UNIVERZITA PALACKÉHO V OLOMOUCI

Přírodovědecká fakulta

Katedra experimentální fyziky

Magnetizmus FeS, MnS a $FeTiO_3$ systémů a laboratorní simulace kosmického zvětrávání

Dizertační práce

Mgr. Jan Čuda

Školitel:

prof. RNDr. Miroslav Mašláň, CSc.

Olomouc

2014

Poděkování

Děkuji svému školiteli prof. RNDr. Miroslavu Mašláňovi, CSc., za odborné vedení, cenné rady a konzultace, které mi poskytl při řešení a vypracování předložené dizertační práce. Dále bych rád poděkoval za odborné vedení a konzultace prof. RNDr. Radku Zbořilovi, Ph.D., doc. Jiřímu Tučkovi, Ph.D. za uvedení do problematiky magnetizmu a Mössbauerovy spektroskopie, doc. Tomáši Kohoutovi, Ph.D. za cenné rady a diskuze nejen v geofyzikální oblasti, Mgr. Milanu Vůjtkovi, Ph.D., doc. Liboru Machalovi, Ph.D., Mgr. Ondřeji Malinovi, a Mgr. Lucii Mohelníkové za formální připomínky k této práci.

Děkuji také týmu Regionálního centra pokročilých technologií a materiálů za přátelskou pracovní atmosféru, cenné rady i připomínky, projektům[1] a Univerzitě Palackého za umožnění podmínek studia.

Mé poslední a obrovské díky patří mým rodičům a přátelům, kteří mě během celého doktorského studia podporovali.

[1] Centrum výzkumu práškových nanomateriálů – 1M0512, Nové technologie přípravy a využití nanočástic na bázi oxidů železa pro ekologické, průmyslové a lékařské aplikace – KAN115600801, RCPTM – CZ.1.05/2.1.00/03.0058, MŠMT – LH12079, IGA – PrF_2013_014.

Seznam prvoautorských a spoluautorských publikací v letech 2010–2014

[i] Kohout, T., **Čuda**, **J.**, Filip, J., Bradley, T., Britt, D., Tuček, J., Skála, R., Kletetschka, G., Kašlík, J., Malina, O., Šišková, K., Zbořil, R. (2014), Space weathering simulations through controlled growth of iron nanoparticles on olivine surface, přijato v časopise *Icarus* (9. 4. 2014).

[ii] Bucko, M., Mattila, O.P., Chrobak, A., Ziolkowski, G., Johanson, B., **Čuda**, **J.**, Filip, J., Zbořil, R., Pesonen, L.J., Lepparanta, M. (2013), Distribution of magnetic particulates in a roadside snowpack based on magnetic, microstructural and mineralogical analyses, *Geophys. J. Int.*, 195, 159–175.

[iii] **Čuda**, **J.**, Kohout, T., Filip, J., Tuček, J., Kosterov, A., Haloda, J., Skála, R., Santala, E., Medřik, I., Zbořil, R. (2013), Low-temperature magnetism of alabandite: Crucial role of surface oxidation, *Am. Miner.*, 98, 1550–1556.

[iv] Marková, Z., Machalová–Šišková, K., Filip, J., **Čuda**, **J.**, Kolar, M., Šafářová, K., Medřík, I., Zbořil, R. (2013), Air stable magnetic bimetallic Fe-Ag nanoparticles for advanced antimicrobial treatment and phosphorus removal, *Environ. Sci. Technol.*, 47, 5285–5293.

[v] Pečová, M., Šebela, M., Marková, Z., Poláková, K., **Čuda**, **J.**, Šafářová, K., Zbořil, R. (2013), Thermostable trypsin conjugates immobilized to biogenic magnetite show a high operational stability and remarkable reusability for protein digestion, *Nanotechnology*, 24, 125102.

[vi] Krisťan, P., Chlan, V., Štěpánková, H., Reznicek, R., Kouril, K., Štěpánek, J., Poláková, K., Procházka**,** V., **Čuda**, **J.**, Medřík, I. (2013), Bentonite/iron oxide composites: preparation and characterization by hyperfine methods, *J. Nanomater.*, 179794.

[vii] Filip, J., Bosi, F., Novák, M., Skogby, H., Tuček, J., **Čuda**, **J.**, Wildner, M. (2012), Iron redox reactions in the tourmaline structure: High-temperature treatment of Fe^{3+}-rich schorl, *Geochim. Cosmochim. Acta*, 86, 239–256.

[viii] Tuček, J., Tuček, P., **Čuda**, **J.**, Filip, J., Pechoušek, J., Machala, L., Zbořil, R. (2012), Iron(III) oxide polymorphs and their manifestations in in-field ^{57}Fe Mossbauer Spectra, Mossbauer Spectroscopy in Materials Science, AIP Conference Proceedings, Editor: J. Tuček, L. Machala, 1489, 56–74, *10th International Conference on Mossbauer Spectroscopy in Materials Science*.

[ix] Kašlík, J., Filip, J., Šeděnková, V., Tuček, J., **Čuda**, **J.**, Zbořil, R. (2012), Thermally induced solid-state route toward magnetite nanoparticles with controlled stoichiometry, Mossbauer Spectroscopy in Materials Science, AIP Conference Proceedings, Editor: J. Tuček, L. Machala, 1489, 75–87, *10th International Conference on Mossbauer Spectroscopy in Materials Science*.

[x] **Čuda**, **J.,** Mousa, I., David, B., Pizurová, N., Tuček, J., Žák, T., Mašláň, M., Schneeweiss, O. (2012), Magnetic properties of $CoFe_2O_4$-$BaTiO_3$ composites, Mossbauer Spectroscopy in Materials Science , AIP Conference Proceedings, Editor: J. Tuček, L. Machala, 1489, 123–132, *10th International Conference on Mossbauer Spectroscopy in Materials Science*.

[xi] **Čuda**, **J.**, Kohout, T., Tuček, J., Filip, J., Medřík, I., Mašláň, M., Zbořil, R. (2012), Mössbauer study and magnetic measurement of troilite extract from natan iron meteorite, Mossbauer Spectroscopy in Materials Science, AIP Conference Proceedings, Editor: J. Tuček, L. Machala, 1489, 145–153, *10th International Conference on Mossbauer Spectroscopy in Materials Science*.

[xii] **Čuda**, **J.**, Kohout, T., Tuček, J., Haloda, J., Filip, J., Prucek, R., Zbořil, R. (2011), Low-temperature magnetic transition in troilite: A simple marker for highly stoichiometric FeS systems, *J. Geophys. Res.*, 116, B11205.

[xiii] Procházka, V., Štěpánková, H., Chlan, V., Tuček, J., **Čuda**, **J.**, Kouril, K., Fillip, J., Zbořil, R. (2011), Electric field gradient in $FeTiO_3$ by nuclear magnetic resonance and ab initio calculations, *J. Phys.-Condes. Matter*, 23, 205503.

[xiv] Pečová, M., Zajoncová, L., Poláková, K., **Čuda**, **J.**, Šafaříková, M., Šebela, M., Šafařík, I. (2011), Biologically active compounds immobilized on magnetic carriers and their utilization in biochemistry and biotechnology, *Chem. Listy*, 105, 524–530.

[xv] **Čuda**, **J.**, Zbořil, R., Schneeweiss, O., Tuček, J., Procházka, V., Mašláň, M., Tuček, P. (2010), Mössbauer study and macroscopic/global magnetic behavior of powdered ilmenite ($FeTiO_3$) sample, Mossbauer Spectroscopy in Materials Science, AIP Conference Proceedings, Editor: J. Tuček, M. Miglierini, 1258, 55–67, *International Conference on Mossbauer Spectroscopy in Materials Science–2010*.

[xvi] Pechoušek, J., Procházka, R., **Čuda**, **J.**, Frydrych, J., Jančík, D. (2010), Investigation of the mossbauer spectrum quality as a dependence on the frequency of the velocity signal, Mossbauer Spectroscopy in Materials Science, AIP Conference Proceedings, Editor: J. Tuček, M. Miglierini, 1258, 134–142, *International Conference on Mossbauer Spectroscopy in Materials Science*–2010.

Vědecké práce komentované v této dizertační práci: [i],[iii], [xi],[xii] a [xv]. Publikace [ii], [iv], [v], [vii] a [xii] byly oceněny „Cenou děkana PřF UP Olomouc“ v kategorii „Článek v časopise“ pro daný rok.

Prohlášení

Prohlašuji, že jsem dizertační práci řešil samostatně, a že použitou literaturu řádně cituji. Dále prohlašuji, že mám většinový autorský přínos v publikacích [i], [iii], [xi], [xii] a [xv], uvedených v seznamu autorských publikací na předchozích stranách.

V Olomouci, dne 29. dubna 2014

Mgr. Jan Čuda

Já, školitel, prohlašuji, že Mgr. Jan Čuda má v publikacích [i], [iii], [xi], [xii] a [xv] většinový autorský přínos.

---

prof. RNDr. Miroslav Mašláň, CSc.

ANOTACE DISERTAČNÍ PRÁCE

Autor: Mgr. Jan Čuda

Název disertační práce: Magnetizmus FeS, MnS a $FeTiO_3$ systémů a laboratorní simulace kosmického zvětrávání

Školitel: prof. RNDr. Miroslav Mašláň, CSc.

Univerzita Palackého v Olomouci

Přírodovědecká fakulta, Katedra experimentální fyziky

Aplikace magnetického měření a Mössbauerovy spektroskopie se odráží v mnoha odvětvích lidského vědeckého bádaní, které poskytuje na jedné straně hledisko systematického popisu a výkladů fyzikálních vlastností, na druhé straně vysvětlení základních koncepcí a mechanismů nutných pro jejich pochopení. Disertační práce se věnuje využití těchto experimentálních technik pro studium (extra)terestriálních minerálů. Konkrétněji je pozornost věnována:

1. Systematickému popisu minerálu ilmenitu z pohledu Mössbauerovy spektroskopie (tj. zdroji elektrického pole kolem mössbauerovsky aktivního jádra, Debyeově teplotě a matematickému proložení Mössbauerova spektra šesti singlety).
2. Nízkoteplotnímu nárůstu magnetické odezvy pro minerál troilit pod ~70 K.
3. Korektnímu matematickému proložení Mössbauerova spektra polykrystalického troilitu.
4. Nízkoteplotnímu magnetickému chování minerálu alabanditu způsobeného povrchovou oxidací.

Mimo jiné je v disertační práci představena nová metoda přípravy analogů kosmického zvětrávaní, která je přestavena na minerálu olivín a která využívá zmíněné experimentální techniky k charakterizaci produktů této přípravy.

ABSTRACT

Author: Mgr. Jan Čuda

Title of thesis: Magnetic study of FeS, MnS a $FeTiO_3$ systems and laboratory simulation of space weathering

Supervisor: prof. RNDr. Miroslav Mašláň, CSc.

Palacký University in Olomouc
Faculty of Science, Department of experimental physics

Magnetic measurements and Mössbauer spectroscopy are broadly reflected in scientific research describing and interpreting physical properties of materials as well as in explanation of basic concepts and mechanisms necessary for their understanding. From this point of view, the thesis is focused on the application of these techniques to study (extra)terrestrial minerals. More specifically the attention is paid to:

1. Systematic description of the mineral ilmenite by means of Mössbauer spectroscopy (i.e., electrical field around the Mössbauer active nuclei, Debye temperature and mathematical fitting of Mössbauer spectra by six singlets).
2. Low-temperature magnetic evolution of troilite sample below ~70 K.
3. Mathematical fitting of Mössbauer spectra of polycrystalline troilite.
4. Low-temperature magnetic behavior of mineral alabandite caused by surface oxidation.

Last but not least, the thesis presents a new method of preparation of space weathering analogues which is introduced for mineral olivine and which also applies the above mentioned experimental techniques to characterize the prepared products.

Obsah

Prohlášení ..... - 6 -

Seznam použitých zkratek ..... - 10 -

Úvod ..... - 12 -

Mössbauerovská studie a makroskopická magnetická odezva práškového ilmenitového ($FeTiO_3$) vzorku ..... - 14 -

Nízkoteplotní magnetický přechod v troilitu: jednoduchý znak pro vysoce stechiometrický FeS systém ..... - 20 -

Mössbauerova studie a magnetické měření minerálu troilitu získaného z železného meteoritu Natan ..... - 26 -

Nízkoteplotní magnetizmus minerálu alabanditu: stěžejní role povrchové oxidace ..... - 31 -

Laboratorní simulace kosmického zvětrávání prostřednictvím kontrolovaného růstu nanočástic železa na povrchu minerálu olivínu ..... - 36 -

Použitá literatura ..... - 40 -

Příloha A ..... - 47 -

Příloha B ..... - 61 -

Příloha C ..... - 71 -

Příloha D ..... - 81 -

Příloha E ..... - 89 -

Seznam použitých zkratek

Označení vzorků

FeS_Bruderheim	přírodní minerál troilit
FeS_Cape_York	přírodní minerál troilit
FeS_Natan	přírodní minerál troilit
Na	přírodní minerál alabandit
SA1	syntetický minerál alabandit
SA1_OX	povrchově oxidovaný syntetický minerál alabandit (SA1)
SA2	syntetický minerál alabandit

Metody měření

FC křivka	Field Cooled křivka
RT SIRM cycle	room temperature saturation isothermal magnetization cycle
ZFC křivka	Zero Field Cooled křivka

Další použité zkratky

A	rezonanční plocha pod mössbauerovskou křivkou
B_A	anizotropní magnetické pole
B_E	výměnné magnetické pole
B_{eff}	efektivní hyperjemné magnetické pole
B_{ext}	externí magnetické pole
B_{hf}	hyperjemné magnetické pole
B_{sf}	magnetické pole nutné pro spinové překlopení
L	jaderné kvantové číslo
M_1	podmřížková magnetizace

M_2	podmřížková magnetizace
m_I	magnetické kvantové číslo
npFe^0	nanočástice redukovaného železa
Q	kvadrupólový moment
T_C	Curieova teplota
T_M	teplota Morinova přechodu
T_N	Néelova teplota
ΔE_Q	kvadrupólové štěpení
∇E_{el}	gradient elektrického pole
δ	izomerní posuv
Θ_D	Debyeova teplota
γ-foton	gama foton

Úvod

Tato dizertační práce si klade za cíl stručně představit vybraná studovaná témata a publikační výstupy v impaktovaných anebo recenzovaných vědeckých periodikách, na nichž se významnou měrou podílel autor této práce během svého doktorského studia. Plné verze jednotlivých článků jsou uvedeny v podobě příloh k této dizertační práci. Rozbor článků je pojat formou krátkého volného komentáře, přičemž samotná forma není koncipovaná jako souhrn či výčet všech výsledků a měření, ale pozornost je věnována těm částem komentovaného článku, které motivovaly autora k vědeckému bádání v dané oblasti a na kterých se autor významnou měrou podílel.

Převážná část komentovaných publikací se zabývá antiferomagnetickými systémy (ilmenit, troilit a alabandit), které patří mezi (extra)terestriální materiály. V těchto studiích byla využívána magnetická měření a Mössbauerova spektroskopie v širokém teplotním rozsahu, resp. aplikací externího magnetického pole. Tyto experimentální přístroje patří mezi stěžejní techniky, kterým se autor během svého doktorského studia věnoval a jejichž menší či větší přínos se odráží ve všech komentovaných publikacích, které se zabývají antiferomagnetickými systémy. V této práci není uveden detailní popis fyzikálního principu těchto experimentálních technik či jejich aplikace na významné teoretické systémy, jednotlivé interpretace a komentáře k těmto technikám budou soustředěny výhradně ve spojitosti se studovanými systémy. Pokud není uvedeno jinak, přínos autora této práce k řešení dané problematiky spočívá v interpretaci dosažených výsledků pomocí magnetického měření a Mössbauerovy spektroskopie.

Poslední kapitola se věnuje nové metodě laboratorní simulace kosmického zvětrávání vyvolávající kvantitativní modifikaci reflektančních spekter ve viditelné a UV oblasti. Tato studie je v současné době zaštítěna čtyřletým česko–americkým projektem, na jehož řešení se autor podílí. V rámci tohoto projektu vznikla první publikace, která je přijatá (9. 4. 2014) k publikaci v časopise ICARUS.

Mössbauerovská studie a makroskopická magnetická odezva práškového ilmenitového ($FeTiO_3$) vzorku

Příloha A

Cílem autorů článku bylo provést detailní mössbauerovskou charakterizaci syntetického ilmenitu. Tento záměr plynul ze snahy o komplexní porozumění problematice hematito–ilmenitových krystalů, které vykazují zajímavé magnetické vlastnosti projevující se vysokou hodnotou saturační magnetizace, samovolným namagnetováním termoremanentní magnetizace proti směru magnetického pole a vysokou hodnotou výměnného pole, které může dosahovat hodnot až 1 T (*Nord a Lawson*, 1989; *Nord a Lawson*, 1992; *McEnroe a kol.*, 2007; *Harrison a kol.*, 2008). Tyto jevy jsou popisovány na základě odlišných přístupů založených na laminárním magnetizmu (*Robinson a kol.*, 2002; *McEnroe a kol.*, 2002; *Robinson a kol*., 2004; *McEnroe a kol.*, 2004; *Robinson a kol.*, 2006; *Fabian a kol.*, 2008; *Kasama a kol.*, 2009), nebo na základě skloněného antiferomagnetického chování v těchto systémech (*Kletetschka a kol*., 2002). Existence více vědeckých přístupů, které vysvětlují zmíněné magnetické vlastnosti, poukazuje na ne zcela jasnou odpověď na popis těchto hematito–ilmenitových krystalů a byla motivací pro studium této problematiky.

Ilmenitu v minulosti nebyla z pohledu Mössbauerovy spektroskopie věnována taková pozornost jako hematitu, proto byl tento minerál studován samostatně, aby bylo možné lépe pochopit a interpretovat mössbauerovská spektra hematito–ilmenitových krystalů. Získané poznatky plynoucí z této studie jsou aplikovány v připravovaném manuskriptu, který se zabývá zmíněnými magnetickými vlastnostmi hematito–ilmenitových krystalů.

V prvním komentovaném článku jsou řešena čtyři vzájemně nezávislá témata základního výzkumu na synteticky připraveném ilmenitu:

(i) zdroj elektrického pole kolem Mössbauerovsky aktivního jádra,

(ii) velikost Debyeovy teploty (Θ_D) pro železnatý iont v ilmenitové struktuře,

(iii) matematické proložení nízkoteplotního Mössbauerova spektra ilmenitu pomocí šesti singletů,

(iv) magnetická měření a Mössbauerova spektroskopie ve vnějším magnetickém poli ilmenitu

Komentovány jsou jen ty výstupy, u kterých je interpretační podíl autora disertační práce, tj. (i), (ii) a (iii).

Zdroji elektrického pole kolem jádra železnatých iontů v ilmenitu se doposud nikdo v literatuře nezabýval. Mössbauerova spektroskopie nabízí velmi jednoduchý způsob, jak získat informace o zdroji elektrického pole kolem mössbauerovsky aktivního jádra (tj. v našem případě jádra železnatých iontů v ilmenitu), a to pomocí sledování teplotní závislosti Mössbauerova hyperjemného parametru, zvaného kvadrupólové štěpení[2] (ΔE_Q).

Obecně existují dva zdroje tohoto elektrického pole, tj. okolní atomy a valenční elektrony nacházející se v atomovém obalu mössbauerovsky aktivního jádra (obr. 1). Pro jednoduchost specifikujme tyto zdroje podle jejich teplotního chování a parametru ΔE_Q, který vystihuje změny elektrického pole obklopující mössbauerovsky aktivní jádro:

[2] Tento parametr vystihuje elektrickou kvadrupólovou interakci nesféricky rozloženého elektrického náboje jádra vloženého do nehomogenního výsledného elektrického pole okolních atomů a jeho valenčních elektronů.

1. Elektrické pole vytvářené okolními atomy[3] – toto elektrické pole se výrazně nemění se změnou teploty, proto nedochází ani ke změnám hodnot ΔE_Q vlivem tohoto zdroje elektrického pole.
2. Elektrické pole generované valenčními elektrony mössbauerovsky aktivního jádra – Je-li nezanedbatelný i tento zdroj elektrického pole kolem mössbauerovsky aktivního jádra, je pozorována teplotní závislost ΔE_Q. Změnou teploty dochází k jiné populaci energetických hladin v atomovém obalu mössbauerovsky aktivního jádra valenčními elektrony, čímž dochází k teplotním změnám elektrického pole obklopujícího jádro.

Z výsledků teplotního chování, konkrétně teplotního vývoje ΔE_Q (viz obr. 3a v příloze A), je patrné, že se změnou teploty měření dochází k posunu hodnoty ΔE_Q. Podle výše zmíněného chování tohoto parametru v závislosti na zdroji elektrického pole, lze stanovit, že valenční elektrony nacházející se v atomovém obalu železnatých iontů v ilmenitu jsou nezanedbatelnými přispěvateli elektrického pole kolem jejich jádra. Je nutné zdůraznit, že při popisu elektrického pole, které obklopuje mössbauerovské aktivní jádro, hraje roli i asymetrické uspořádání nábojů vzdálených iontů (tj. okolních atomů)[4]. Výsledné elektrické pole obklopující jádro železnatých iontů v ilmenitu je důsledkem jak jeho valenčních elektronů, tak i okolních atomů.

---

[3] Elektrické pole je vytvářeno asymetrickým uspořádáním nábojů (nebo dipólů) vzdálených iontů obklopující mössbauerovsky aktivní jádro, čímž se pozmění polarizace nábojové hustoty elektronů, které se nacházejí nejblíže k jádru atomu, což se projeví zesílením nebo zeslabením gradientu elektrického pole (∇E_{el}) v místě jádra (*Tuček*, 2008).

[4] Ilmenit nemá kubickou krystalografickou mřížku, takže okolní atomy mají podíl na výsledném elektrickém poli kolem jádra železnatých iontů v ilmenitu.

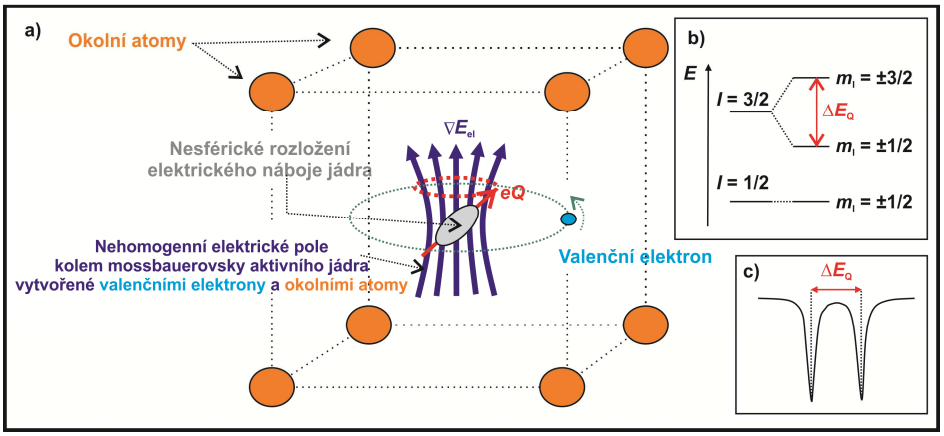

Obr. 1. (a) Elektrická kvadrupólová interakce mezi nesféricky rozložením elektrického náboje jádra popsaného kvadrupólovým momentem (Q) a nehomogenním elektrickým polem kolem mössbauerovsky aktivního jádra vytvářeného okolními atomy a valenčními elektrony, které bývá charakterizováno tenzorem gradientu elektrického pole, (b) energetické schéma rozštěpení jaderných energetických stavů, kde I odpovídá jadernému kvantovému číslu a m_I je magnetické kvantové číslo a (c) projev elektrické kvadrupólové interakce kvadrupólovým štěpením v mössbauerovském spektru.

Stejně jako nebyly v literatuře zmínky o zdroji elektrického pole kolem jádra železnatých iontů v ilmenitu, nebyla v minulosti věnována pozornost ani Debyeově teplotě těchto iontů. Velikost této fyzikální veličiny, která vystihne tuhost vazby železnatého iontu v ilmenitové struktuře, je získána pomocí teplotních závislostí izomerního posuvu (δ) a rezonanční plochy pod mössbauerovskou křivkou (A) (viz obr. 3b a 3c v příloze A). Matematickým proložením[5] těchto závislostí lze získat doposud první odhad Debyeovy teploty pro iont železa v ilmenitové struktuře $\Theta_D = (359 \pm 27)$ K. Tento odhad teploty pro železnatý iont v ilmenitu je porovnán s podobnými krystalovými strukturami, u kterých lze přepokládat podobnou tuhost vazby, tj. i Debyeovu

[5] Teplotní závislosti δ a A jsou velmi dobře matematicky popsatelné prostřednictvím klasických vysokoteplotních limitů (viz vztah 1 a 3 v příloze A) jak pro relativistický posun, tak i pro relativní podíl jaderných emisních/absorpčních přechodů bez přenosu energie na krystalovou mříž (*Greenwood a Gibb*, 1971; *Chen a Yang*, 2007).

teplotu (tab. 1). Toto srovnání přináší uspokojivou shodu ve velikostech Θ_D, a proto lze použitý postup odhadu velikosti Θ_D považovat za korektní, a stejně tak i pracovat se získanou hodnotou Debyeovy teploty pro ilmenit v rámci fyziky pevných látek.

Látka	**Θ_D [K]**
$(FeTiO_3)_{0,5}$–$(Fe_2O_3)_{0,5}$	355 ± 5
$MnTiO_3$	370 ± 10

Tab. 1. Hodnoty Debyeových teplot pro železný iont v $(FeTiO_3)_{0.5}$-$(Fe_2O_3)_{0.5}$ a mangan v cínem dopovaném $MnTiO_3$ (*Kin a kol.*, 2008; *Fabritchnyi a kol.*, 2003).

Podobně jako tomu bylo v případě zdroje elektrického pole kolem mössbauerovsky aktivního jádra a velikosti Debyeovy teploty, nebyla také v minulosti řešena problematika pozic jednotlivých mössbauerovských linií Ilmenitu v magneticky uspořádaném stavu. U ilmenitu dochází k výraznému překrytí těchto linií, které nejsou na první pohled patrné či rozeznatelné (obr. 2), následkem relativně vysoké hodnoty kvadrupólového štěpení ($\Delta E_Q \sim 1{,}44$ mm/s) k poměrně nízké hodnotě hyperjemného magnetického pole ($B_{hf} \sim 4{,}5$ T).

Identifikace polohy jednotlivých mössbauerovských linií ilmenitu bylo docíleno prostřednictvím izomerních posuvů šesti singletů získaných matematickým proložením studovaného mössbauerovského spektra. Dodržením všech nutných fyzikálních podmínek a vazeb mezi jednotlivými mössbauerovskými singlety (viz poslední odstavec na straně 61 v příloze A) lze získat požadované matematické proložení pomocí šesti singletů (viz obr. 4c v příloze A) a jejich izomerní pozice (viz tab. 3 v příloze A) pro Mössbauerovo spektrum ilmenitu při 5 K.

Ověření správnosti získaného výsledku izomerních pozic je v komentovaném čánku provedeno nepřímo. Pomocí těchto pozic jednotlivých singletů jsou stanoveny velikosti mössbauerovských hyperjemných parametrů, tj. B_{hf} a ΔE_Q, které jsou porovnány se stejnými parametry získanými na základě matematického proložení stejného Mössbauerova spektra pomocí statického Hamiltoniánu zahrnujícího jak magnetickou, tak kvadrupólovou interakci (viz obr. 4b a tab. 2 v příloze A). Tato srovnání dává uspokojivou shodu ve velikosti těchto parametrů[6], čímž nepřímo potvrzují správnou polohu izomerních pozic šesti singletů (viz tab. 3 v příloze A).

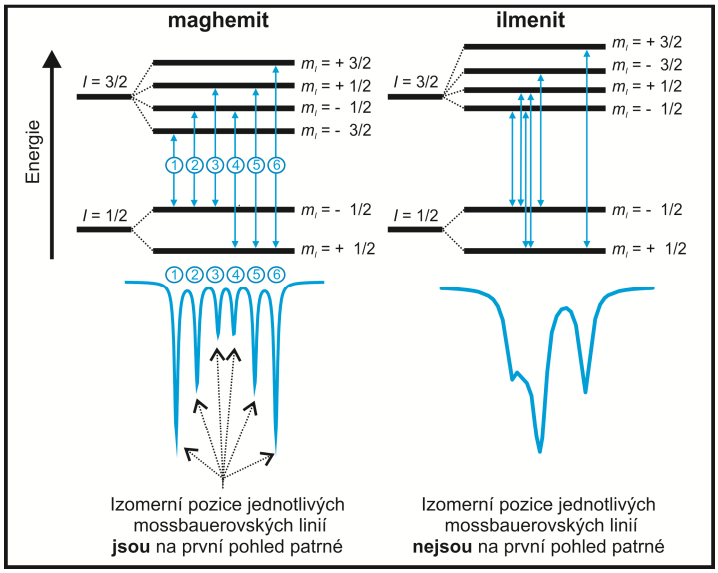

Obr. 2. Schématické znázornění štěpení jaderných energetických hladin základního a excitovaného stavu polykrystalických vzorků maghemitu a ilmenitu s odpovídajícími mössbauerovskými průběhy. Maghemit ilustruje situaci, kdy izomerní pozice jednotlivých mössbauerovských linií jsou na první pohled patrné, kde I odpovídá jadernému kvantovému číslu a m_I je magnetické kvantové číslo.

[6] ΔE_Q = 1,45 mm/s (ΔE_Q = 1,44 mm/s) a B_{hf} = 4,3 T (B_{hf} = 4,5 T) získané matematickým proložením pomocí šesti singletů (využití modelu statického Hamiltoniánu v programu MossWinn u stejného Mössbauerova spektra).

Nízkoteplotní magnetický přechod v troilitu: jednoduchý znak pro vysoce stechiometrický FeS systém

Příloha B

Magnetické minerály fascinují lidskou společnost od pradávna a neutuchající zájem o ně vede k vzájemně propojeným vědeckým oblastem ve snaze o co nejlepší popis jejich magnetických dějů s následným využitím v různých oblastech lidské činnosti. V tomto duchu je v předloženém článku (příloha B) věnována pozornost základnímu výzkumu na minerálu troilitu (FeS), konkrétněji pozorovanému neočekávanému nárůstu magnetické odezvy pod ~70 K (*Kohout a kol.*, 2007). Troilit přechází do antiferomagneticky uspořádaného stavu při Néelově teplotě T_N ~ 588 K (*Wang a Salveson*, 2005) a uvážíme-li polykrystalickou povahu troilitu studovaného autory *Kohout a kol.* (2007), je očekávaným výsledkem pouze pokles magnetické odezvy s klesající teplotou a nikoliv její nárůst pod ~70 K (obr. 3).

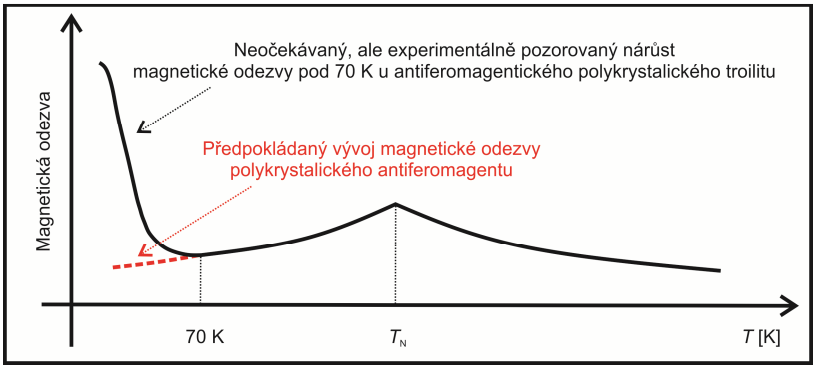

Obr. 3. Schematický obrázek problematiky neočekávaného nárůstu magnetické odezvy pod ~70 K pro antiferomagnetický polykrystalický troilit studovaný autory *Kohout a kol.* (2007).

Tento nesoulad mezi předpokladem[7] a experimentálním pozorováním[8] vedla autory *Kohout a kol.* (2007) k vyslovení hypotézy existence teplotně řízeného magnetického přechodu Morinova typu udělujícího troilitu pod ~70 K výsledné feromagnetické vlastnosti. Teplotně řízený Morinův přechod je znám pro minerál hematit, kde u antiferomagnetického systému vzniká feromagnetická odezva nad ~260 K (obr. 4). *Kohout a kol.* (2007) navrhují analogii s tímto hematitovým Morinovým přechodem také pro minerál troilit[9], přičemž feromagnetická odezva by vznikala právě pod teplotou ~70 K.

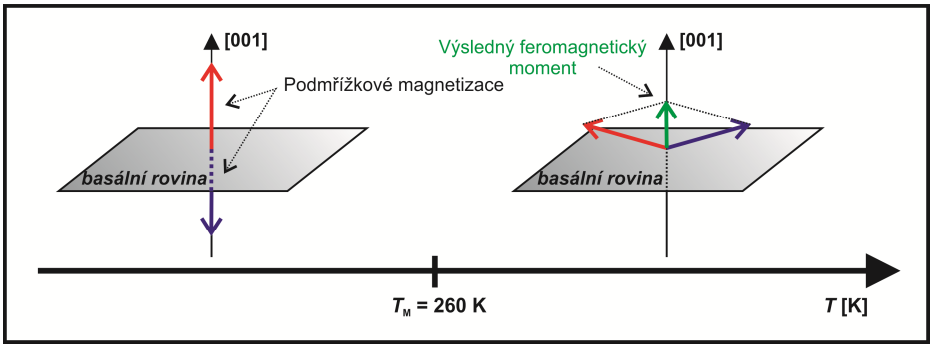

Obr. 4. Uspořádání magnetických podmřížkových magnetizací v minerálu hematitu (červená resp. modrá barva reprezentuje podmřížkové magnetizace). Pod Morinovým teplotním přechodem (T_M ~ 260 K) leží kolineárně antiferomagnetické podmřížkové magnetizace podél osy [001]. Nad ~260 K antiferomagneticky uspořádané podmřížkové magnetizace se překlopí o 90˚ do basální roviny, ze které následně slabě rotují ve směru osy [001]. Podmřížkové magnetizace již nejsou kolineární nad ~260 K, a dávají tak vzniku slabému feromagnetickému momentu celého systému (*Cornell a Schwertmann*, 2003).

Prozkoumáme-li pečlivěji data vedoucí k vyslovené domněnce přechodu Morinova typu u minerálu troilitu při ~70 K uvedené v *Kohout a kol.* (2007), zjistíme, že postrádají

[7] Pokles magnetické odezvy s klesající teplotou pod ~70 K.

[8] Neočekávaný nárůst magnetické odezvy pod ~70 K.

[9] Obráceně než u hematitu, tj. troilit je ferimagnetický pod Morinovou teplotou a antiferomagnetický nad ní.

experimentální potvrzení a navíc samotná studie probíhala pouze na jednom vzorku troilitu. Proto *Gattacceca a kol.* (2011) navrhli jiné vysvětlení, a to že za zmíněným nízkoteplotním magnetickým chováním pravděpodobně stojí ferimagnetická nečistota v podobě minerálu chromitu ($FeCr_2O_4$). Tento minerál přechází do magneticky uspořádaného stavu právě kolem inkriminované teploty (~70 K), což se projevuje nárůstem magnetické odezvy pod touto teplotou. Podle *Gattacceca a kol.* (2011) jeho přítomnost v systému studovaného *Kohout a kol.* (2007) modifikuje nízkoteplotní magnetický průběh tak, jak je schematicky ukázáno na obr. 3. Jinými slovy řečeno pozorovaný nízkoteplotní nárůst magnetické odezvy pod ~70 K, připsaný původně minerálu troilitu ve studii *Kohout a kol.* (2007), je pouze odrazem magnetického projevu zmíněné nečistoty chromitu.

Článek v příloze B věnuje pozornost zmíněným sporným otázkám problematiky nízkoteplotního nárůstu magnetické odezvy, kterými jsou:

(i) nalezení dalšího velmi čistého a stechiometrického troilitu potvrzujícího, že anomálie při teplotě ~70 K není jen vlastností jednoho vzorku, ale je „obecným“ rysem minerálu troilitu,

(ii) ověření správnosti použité terminologie „přechod Morinova typu“ pro nízkoteplotní magnetickou anomálii při ~70 K u troilitu zavedené autory *Kohout a kol.* (2007) a

(iii) prostudování nízkoteplotního magnetického děje pod ~70 K jakožto možného projevu nečistoty v podobě chromitu navržené *Gattacceca a kol.* (2011).

Pro studium nízkoteplotní anomálie při ~70 K jsou v článku použity dva extraterestriální polykrystalické troility získané z chondritických meteoritů Cape York IIIAB (FeS_Cape_York) a Bruderheim L6 (FeS_Bruderheim). Vzorek FeS_Bruderheim je totožný s tím, který byl již dříve použitý ve studii *Kohout a kol.* (2007), a pro něhož byl na základě teplotního magnetického měření navrhnut Morinův přechod pro minerál troilit při teplotě ~70 K. Převážná část srovnávajících měření s nově studovaným troilitickým vzorkem (FeS_Cape_York) je uvedená v doplňkové příloze k článku (supplementary k příloze B). Je potřeba upozornit, že se jedná o měření, která nebyla v dřívější vědecké práci *Kohout a kol.* (2007) provedena či publikována.

Prvním cílem autorů článku (příloha B) bylo nalezení dalšího stechiometrického troilitu s „neočekávaným" nárůstem magnetické odezvy pod ~70 K podobný tomu, jaký pozorovali *Kohout a kol.* (2007). Z pohledu magnetického měření má nově studovaný troilit (tj. FeS_Cape_York vzorek) stejný nízkoteplotní projev v podobě nárůstu magnetické odezvy pod ~70 K (viz obr. 3a a 3b v příloze B), jako dříve studovaný troilit *Kohout a kol.* (2007). Experimentální techniky sloužící ke stanovení krystalové struktury, stechiometrie a čistoty prokazují strukturu troilitu s téměř stechiometrickým poměrem železa a síry bez dalších zjevných nečistot pro vzorek FeS_Cape_York. To dokládá, že se autorům podařilo najít další velmi čistý a stechiometrický troilit, který má stejné nízkoteplotní magnetické chování srovnatelné s již dříve studovaným troilitem *Kohout a kol.* (2007).

Mössbauerova spektroskopie byla použita pro potvrzení anebo vyvrácení druhého vytyčeného cíle týkajícího se správnosti užité terminologie „přechod Morinova typu" pro troilit při ~70 K vyslovené *Kohout a kol.* (2007). Z pohledu Mössbauerovy spektroskopie se Morinův

přechod projevuje výraznou změnou hyperjemného parametru ΔE_Q získaného nad a pod tímto přechodem[10]. Srovnáme-li tento charakteristický znak Morinova přechodu s výsledky získanými pro nově studovaný troilit (FeS_Cape_York vzorek), nepozorujeme žádnou změnu hyperjemného parametru ΔE_Q nad a pod ~70 K (viz tab. 2 v příloze B). Studovaný troilit tedy nesplňuje požadovaný charakteristický znak Morinova přechodu ve změně velikosti ΔE_Q. Stejného výsledku je dosaženo i v rámci srovnávacího měření pro FeS_Bruderheim vzorek, tj. žádná změna ve velikosti ΔE_Q nad a pod inkriminovanou teplotou. Autoři článku na základě těchto výsledků vyjadřují závěr, že pozorované nízkoteplotní magnetické chování u troilitu při ~70 K není strukturně řízený Morinův přechod z pohledu Mössbauerovy spektroskopie a užití terminologie „přechod Morinova typu“ pro tento děj může být do jisté míry zavádějící, či chybné.

Poslední sporná otázka vychází ze studie *Gattacceca a kol.* (2011), kteří tvrdí, že „neočekávaný“ nárůst magnetické odezvy pod ~70 K je odrazem pouze ferimagnetické nečistoty, která přechází do magneticky uspořádaného stavu kolem inkriminované teploty (~70 K). *Gattacceca a kol.* (2011) navrhují vhodného kandidáta v podobě chromitu přecházejícího do ferimagnetického stavu při ~70 K.

Pro potvrzení či vyvrácení přítomnosti chromitu v nově studovaném troilitu (FeS_Cape_York vzorek), který vykazuje „neočekávaný“ nárůst, byla provedena mineralogická, strukturní a chemická analýza s ohledem na případnou kontaminaci studovaného vzorku touto látkou. Detailní rozbor výsledků a atributů těchto pozorování poukazuje na přítomnost chromitu

[10] U minerálu hematitu dochází k výrazné změně hyperjemného Mössbauerova parametru ΔE_Q nad a pod Morinovým přechodem. Pro představu pod inkriminovanou teplotou Morinova přechodu je ΔE_Q ~ 0,37 mm/s, ale nad touto teplotou nabývá záporných hodnot ΔE_Q ~ -0,19 mm/s (*Vandenberghe a kol.*, 1990; *Zbořil a kol.*, 2002).

ve studovaném FeS_Cape_York systému, avšak ve velmi nízké koncentraci, neschopné uspokojivě vysvětlit jeho sledované nízkoteplotní magnetické chování pod ~70 K.

Nově provedená magnetická měření (viz obr. 3c v příloze B) pro FeS_Cape_York vzorek poodkrývají případný charakter daného magnetického přechodu pro troilit při ~70 K. Patrná změna trendu v „room temperature saturation isothermal magnetization cycle"[11] (RT SIRM cycle) při ~70 K odpovídá přechodu z feromagnetického do antiferomagnetického stavu spíše než transformaci z paramagnetického do ferimagnetického stavu, která by odpovídala minerálu chromit podle *Gattacceca a kol.* (2011). „RT SIRM cycle" měření tedy vybízí k původní myšlence zavedené autory *Kohout a kol.* (2007), že uvedené nízkoteplotní magnetické chování při teplotě ~70 K je pravděpodobně charakteristickou vlastností minerálu troilitu.

Na základě dosažených výsledků se autoři článku přiklánějí k interpretaci, že nízkoteplotní nárůst magnetické odezvy je charakteristickou vlastností minerálu troilitu spíše než projevem ferimagnetické nečistoty chromitu, přičemž tento děj při ~70 K nemá povahu Morinova přechodu. Na druhé straně korektně uveďme, že publikovaná studie nedokáže jednoznačně vysvětlit proces vzniku feromagnetické odezvy pod inkriminovanou teplotou, proto mechanismus magnetické odezvy pod ~70 K zůstal neobjasněn.

[11] RT SIRM cycle – zaznamenávání teplotní magnetické odezvy saturační remanentní magnetizace z pokojové teploty na nízkou a zpět, kdy saturační remanence je vtištěna pomocí dostatečného vnějšího magnetického pole před začátkem měření.

Mössbauerova studie a magnetické měření minerálu troilitu získaného z železného meteoritu Natan

Příloha C

Článek v příloze C volně navazuje na předchozí komentovaný článek týkajícího se antiferomagnetického minerálu troilitu. Hlavní přínos i motivace autorů článku spočívá ve znázornění správného matematického prokládání nízkoteplotního mössbauerovského spektra ve vnějším magnetickém poli, a to pro polykrystalický antiferomagnetický FeS systém.

Než přistoupíme k obecnějšímu popisu projevu aplikovaného externího magnetického pole na Mössbauerova spektra polykrystalického antiferomagnetického materiálu, věnujeme pozornost problematice antiferomagnetické látky v magnetickém poli z pohledu Mössbauerovy spektroskopie. Stručně zmíníme dva mezní případy pro antiferomagnetický monokrystal[12]:

1. působí-li vnější magnetické pole podél osy antiferomagnetické látky, dochází k zvýšení podmřížkové magnetizace paralelní s externím magnetickým polem (B_{ext}) a snížení podmřížkové magnetizace antiparalelní s B_{ext}, což je odrazem přičtení či odečtení B_{ext} od pole popisujícího chování magnetizace na jednotlivých podmřížkách. Z pohledu Mössbauerovy spektroskopie je pozorován podobný vývoj jako v případě ferimagnetické látky, kdy se původní Mössbauerovo spektrum štěpí do dvou subspekter vektorovým

[12] Antiferomagnetickým monokrystalem je pro jednoduchost míněna kolineární jednoosá antiferomagnetická látka, která je složena ze dvou vykompenzovaných magnetických podmřížek s magnetizacemi M_1 a M_2, a s jednou krystalografickou pozicí pro mössbauerovsky aktivní jádro. V takovém případě Mössbauerovo spektrum bez vnějšího magnetického pole vykazuje pouze jeden sextet pod T_N (obr. 5a a 6a).

přičtením a odečtením B_{ext} od B_{hf} na jednotlivých podmřížkách (obr. 5b). Jakmile B_{ext} nabude hodnoty spinového překlopení (*Johnson*, 1989):

$$B_{sf} = \sqrt{(2 \cdot B_E + B_A)B_A}\,, \qquad (1)$$

kde B_E a B_A jsou výměnné, resp. anizotropní pole, jsou magnetické momenty podmřížkových magnetizací M_1 a M_2 překlopeny do osy kolmé k vnějšímu magnetickému poli. Dvě rozštěpená mössbauerovská subspektra (v případě $B_{ext} \neq 0$ T a $B_{ext} < B_{sf}$) se zhroutí do jednoho sextetu s výrazným nárůstem 2. a 5. spektrální linie. Sextet má nyní limitní poměr mezi liniemi 3 : 4 : 1 (obr. 5c). Další zvyšování hodnoty vnějšího magnetického pole natáčí podmřížkové magnetizace do směru tohoto pole, čímž dochází u sextetu k mírnému zvyšovaní hodnoty efektivního hyperjemného magnetického pole (B_{eff}) a postupnému vymizení 2. a 5. linie (obr. 5d). Linie 2. a 5. zcela vymizí v případě úplného kolineárního natočení podmřížkových magnetizací M_1 a M_2 do směru B_{ext}.

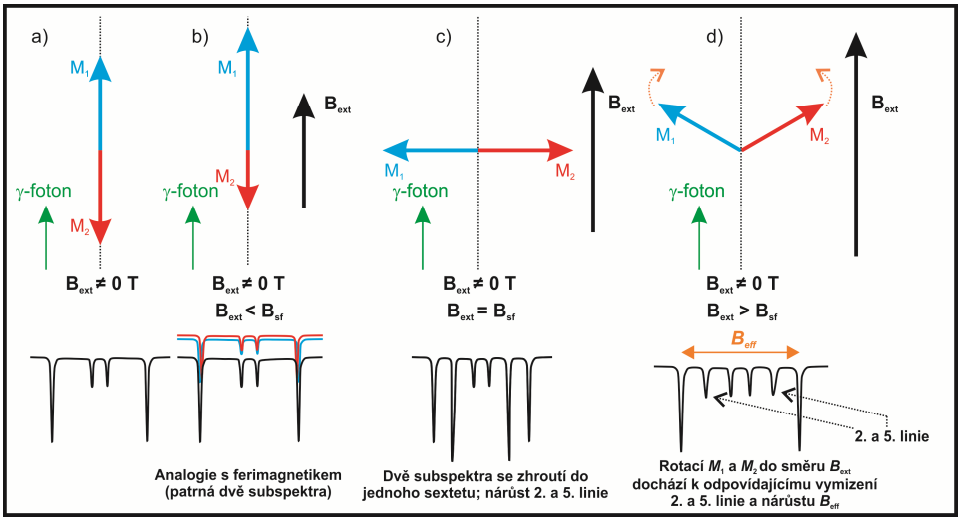

Obr. 5. Schématické znázornění vlivu vnějšího magnetického pole působícího podél antiferomagnetické osy podmřížkových magnetizací M_1 a M_2 a odpovídající mössbauerovské spektra, kde B_{ext} představuje externí magnetické pole, B_{sf} pole nutné pro indukování spinového překlopení, B_{eff} efektivní hyperjemné pole a γ-foton představuje chod gama paprsku Mössbauerovy spektroskopie.

2. Aplikujeme-li magnetické pole na začátku kolmo na osu antiferomagnetické látky u monokrystalu, magnetické momenty ležící původně podél této osy (obr. 6a) začínají rotovat do směru působícího pole (obr. 6b a 6c). Odpovídající mössbauerovská subspektra jednotlivých magnetických podmřížek jsou rovnocenná, přičemž dochází k mírnému nárůstu B_{eff} na mössbauerovsky aktivních jádrech v důsledku zvyšovaní hodnoty B_{ext} (*Frankel*, 1974; *Pankhurst,* 1991; *Johnson*, 1996).

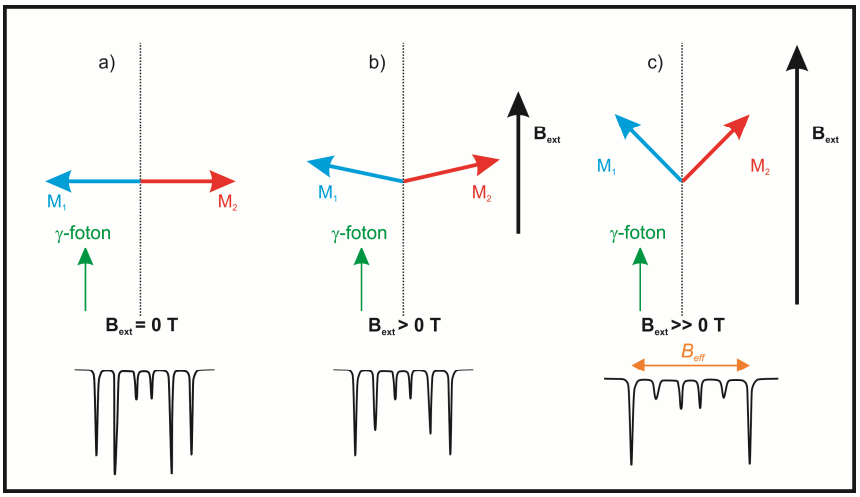

Obr. 6. Schématické znázornění vlivu B_{ext} působující kolmo na antiferomagnetickou osu podmřížkových magnetizací M_1 a M_2 a odpovídající mössbauerovské spektra, kde B_{ext} představuje externí magnetické pole, B_{eff} efektivní hyperjemné pole a γ-foton představuje chod gama paprsku Mössbauerovy spektroskopie.

Mnohem složitější situace nastává v případě aplikace vnějšího magnetického pole na polykrystalické antiferomagnetické látky, kde dostáváme zprůměrované výsledné Mössbauerovo spektrum přes všechny možné a zcela náhodné směry antiferomagnetických os u jednotlivých domén v polykrystalické látce. Jinými slovy se zde projevují výše zmíněné mezní případy pro antiferomagnetický monokrystal v magnetickém poli (obr. 5 a 6). Pro jednoduchost věnujme

pozornost pouze výsledkům vnějšího magnetického pole na výsledné Mössbauerovo spektrum. To vykazuje nárůst 2. a 5. linie a rozšíření všech linií v porovnání se spektrem měřeného v nulovém magnetickém poli (obr. 7a), přičemž šířka linie klesá od vnějších k vnitřním liniím (obr. 7b a 7c). Rozšiřování linií se zastaví při hodnotě $B_{ext} = B_{sf}$, kde pozorujeme zpětné zúžení mössbauerovských linií (obr. 7d) (*Pankhurst a Pollard*, 1990). Aplikace většího magnetického pole než B_{sf} (tj. $B_{ext} > B_{sf}$) vede již k postupnému vymizení 2. a 5. linie a odpovídajícímu nárůstu B_{eff} (obr. 7e a 7f).

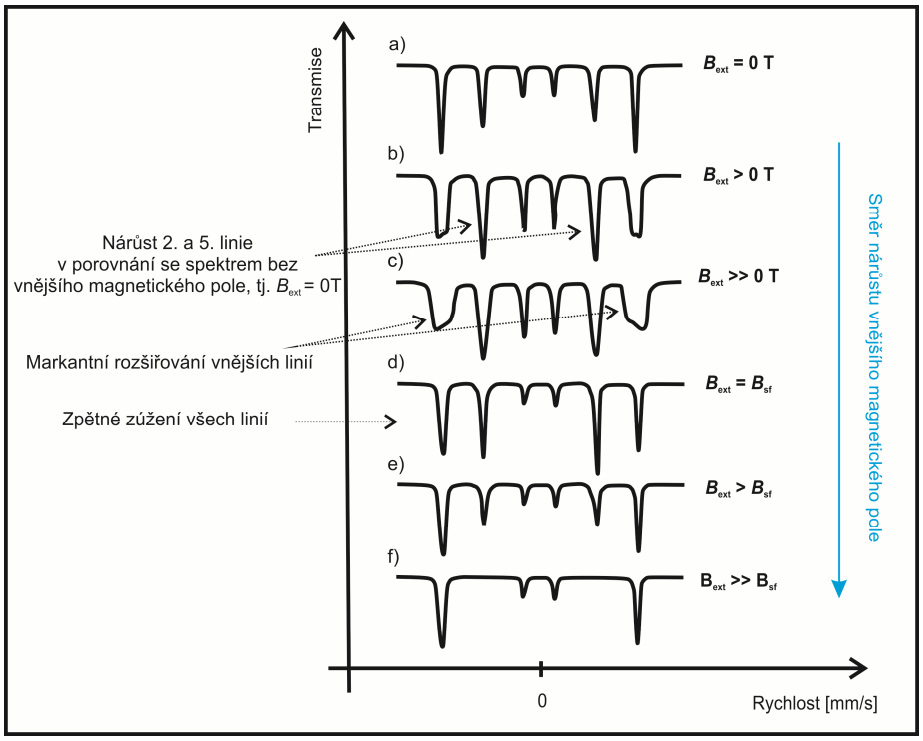

Obr. 7. Schématické znázornění vývoje mössbauerovského spektra polykrystalického antiferomagnetu v externím magnetickém poli, který má jednu krystalografickou pozici pro mössbauerovsky aktivní jádro, kde B_{ext} představuje externí magnetické pole a B_{sf} pole nutné pro indukování spinového překlopení.

Při pohledu na nízkoteplotní mössbauerovské spektrum v externím magnetickém poli 5 T pro antiferomagnetický polykrystalický troilit (FeS_Natan vzorek) (viz obr. 2c v příloze C), je

patrné, že jsou splněny uvedené předpoklady pro polykrystalický antiferomagnet v magnetickém poli z pohledu Mössbauerovy spektroskopie (a to pro případ $B_{sf} > B_{ext}$, viz také obr. 7b či 7c). To potvrzuje interpretaci, že matematické proložení výše uvedeného spektra studovaného troilitu v magnetickém poli vyžaduje užití modelu pro polykrystalický antiferomagnetický systém. Uvedené spektrum bylo matematicky proloženo prostřednictvím distribuce efektivního hyperjemného pole mající pouze jedno maximum (viz obr. 2d v příloze C), což odpovídá předpokladu jedné krystalografické pozice pro železnatý iont ve struktuře troilitu a užití pouze jednoho sextetu pro korektní matematické proložení Mössbauerova spektra troilitu v externím magnetickém poli.

V tomto případě není možné použít teoretický model matematického prokládání Mössbauerova průběhu zaznamenaného ve vnějším magnetickém poli pro antiferomagnetikum, které má neideální antiferomagnetické chování[13] (*Čuda a kol.*, 2010) a na jeho základě interpretovat Mössbauerovská spektra polykrystalického antiferomagnetického troilitu ve vnějším magnetickém poli. K použití tohoto modelu svádí „neobvyklé“ rozšíření vnějších linií u polykrystalického troilitu[14] (viz obr. 2c v příloze C), které na první pohled naznačuje nekorektní použití dvou sextetů, jenž jsou typické pro zmíněný teoretický model.

[13] Tento model přepokládá antiferomagnetický systém se dvěma rovnocennými magnetickými podmřížkami a jednu krystalografickou pozici pro železný iont ve struktuře (stejně jako v případě troilitu). Dále se předpokládá, že vlivem vnějšího magnetického pole se jednotlivé podmřížkové magnetizace chovají na sobě vzájemně nezávisle, tj. neideální antiferomagnetické chování tohoto systému ve vnějším magnetickém poli. Potom je Mössbauerovo spektrum ve vnějším magnetickém poli proloženo ne pomocí jednoho sextetu (jako v případě troilitu) ale dvou, přičemž každý sextet odpovídá jedné magnetické podmřížce.

[14] Obecný příklad polykrystalického antiferomagnetu v magnetickém poli, kdy $B_{ext} < B_{sf}$ (obr. 7b a 7c).

Nízkoteplotní magnetizmus minerálu alabanditu: stěžejní role povrchové oxidace

Příloha D

Za jistých okolností magnetická měření pracují jako experimentální nástroje poskytující informace o fázovém složení, principálně založené na hledání známých magnetických znaků, které jsou neoddiskutovatelným magnetickým podpisem dané fáze. Ve zmíněném duchu *Petrakovski a kol.* (2001) publikovali tento charakteristický magnetický znak či podpis nestechiometrických alabanditů bohatších na mangan (Mn_xS; $1 \leq x \leq 1{,}25$), který uděluje těmto antiferomagnetickým systémů feromagnetické vlastnosti pod ~40 K (obr. 8).

Citovaná studie (*Petrakovski a kol.*, 2001) nebere v úvahu klíčovou otázku čistoty studovaných systémů, a vrhá tak stín pochybnosti na možné aplikace tohoto charakteristického znaku z pohledu magnetického rozpoznávání nestechiometrických alabanditových systémů. Případná přítomnost feromagnetické či ferimagnetické nečistoty, u které narůstá magnetická odezva přechodem do uspořádaného magnetického stavu kolem inkriminované teploty (~40 K), by mohla vysvětlit pozorované nízkoteplotní magnetické chování studované *Petrakovski a kol.* (2001). V takovém případě je nárůst magnetické odezvy pouhým magnetickým projevem zmíněné nečistoty a nikoliv charakteristickým magnetickým znakem těchto nestechiometrických albanditových systémů. Následné využití tohoto jevu při magnetickém identifikovaní nestechiometrických alabanditů bohatších na mangan (tj. Mn_xS; $1 \leq x \leq 1{,}25$) například v mnoha fázovém systému by bylo zavádějící, či přímo chybné.

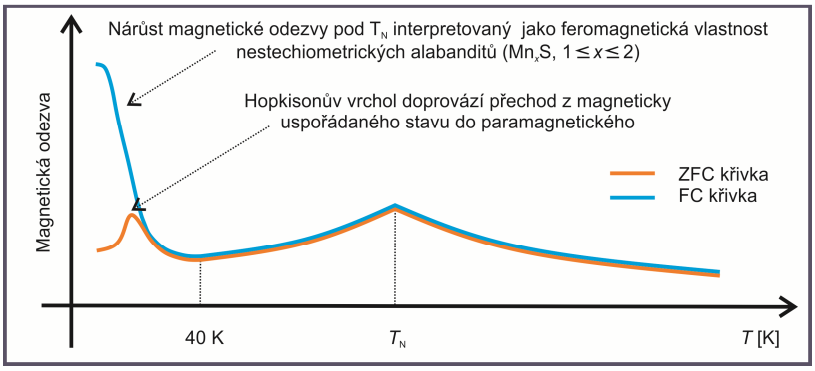

Obr. 8. Schématický obrázek nárůstu magnetické odezvy pod ~40 K u nestechiometrických alabanditů, interpretované jako jejich feromagnetická vlastnost *Petrakovski a kol.* (2001), kde T_N označuje Néelovu teplotu těchto systémů. (Zero-field-cooled) ZFC křivka odpovídá měření, kde je vzorek bez přítomnosti vnějšího magnetického pole vychlazen z pokojové teploty na nízkou teplotu (např. 5 K). Samotné magnetické měření probíhá při ohřevu z této nízké teploty na pokojovou teplotu v příslušném vnějším magnetickém poli. Field-Cooled (FC) křivka je důsledkem velmi podobného měření jako ZFC křivka, jen s tím rozdílem, že vzorek je chlazen na nízkou teplotu již v přítomnosti příslušného vnějšího magnetického pole.

Článek v příloze D zabývající se nízkoteplotním magnetizmem minerálu alabanditu řeší zmíněnou problematiku přítomnosti nečistoty a jejího případného vlivu na nízkoteplotní magnetickou odezvu těchto nestechiometrických alabanditů. Než-li budou uvedeny tyto závěry, věnujme v krátkosti pozornost výsledkům dosaženým ve studii v příloze D.

V článku jsou zkoumány tři alabanditové systémy, a to jeden přírodní (NA vzorek) a dva synteticky připravené (SA1 a SA2 vzorky). Z pohledu magnetického měření je u nich patrný jev nárůstu magnetické odezvy pod ~40 K (viz obr. 2 v příloze D) podobný tomu, jaký pozorovali pro nestechiometrické alabandity pod ~40 K *Petrakovski a kol.* (2001). Toto magnetické chování je ale překvapivým výsledkem v případě NA a SA2 vzorků, protože rentgenová a elementární analýza zařazuje tyto dva systémy do oblasti vysoce stechiometrických příkladů alabanditu (viz

obr. 1 a tab. 1 v příloze D). Jak je známo, ten má antiferomagnetické uspořádání pod $T_N \sim 153$ K (*Heikens a kol.*, 1977; Pearce a kol., 2006) a spolu s polykrystalickou povahou těchto vzorků je predikovaným výsledkem pouze pokles teplotního průběhu magnetické odezvy pod ~153 K a nikoliv její nárůst při nižší teplotě (tj. pod ~40 K). Toto neočekávané avšak pozorované magnetické chování u NA a SA2 vzorků naznačuje přítomnost feromagnetické či ferimagnetické nečistoty v těchto systémech. Na základě níže uvedených bodů je předpokládáno v příloze D, že nečistotou je feromagnetický minerál hausmanit (Mn_3O_4):

1. Hausmanit má Currierovu teplotu $T_C \sim 41–43$ K (*Dwight a Menyuk*, 1960; *Robie a Hemingway*, 1985) velmi blízko inkriminované teplotě ~40 K – pod touto teplotou dochází vlivem přechodu do ferimagnetického stavu k nárůstu jeho magnetické odezvy. Přítomnost tohoto minerálu ve studovaných systémech (NA a SA2) může vysvětlit „překvapivý“ nárůst magnetické odezvy pod ~40 K.
2. Detailní rentgenová analýza poukazuje na minoritní přítomnost oxidu manganu v podobě minerálu hausmanitu v NA systému. Rietveldovou analýzou určené zastoupení hausmanitu v NA vzorku (~6,9 hm. %) koresponduje s potřebným množstvím této látky (tj. ~5,3 hm. %) pro vysvětlení magnetického chování tohoto vzorku pod ~40 K. Nízkoteplotní magnetické chování pod ~40 K u NA vzorku je odrazem hausmanitu a nikoliv majoritní fáze minerálu alabanditu (~93,1 hm. %).
3. Záměrným zoxidováním povrchu zrn práškového vzorku SA1 dojde k zvýšení přítomnosti minerálu hausmanitu v SA1 systému (viz obr. 1d v příloze D). Teplotní závislost magnetické odezvy tohoto povrchově modifikovaného systému (označeného

v komentovaném článku jako SA1_OX vzorek), vykazuje stejný profil nízkoteplotního magnetického chování s předpokládaným větším magnetickým nárůstem pod ~40 K (viz obr. 5 v příloze D). Magnetický nárůst je v souladu s určenou přítomností hausmanitu v povrchově modifikovaném systému (SA1_OX vzorek). Rietveldovou analýzou určené zastoupení hausmanitu (~22 hm. %) odpovídá potřebnému množství toho minerálů (~20 hm. %), které je nutné pro vysvětlení nízkoteplotního magnetického chování SA1_OX vzorku.

4. Přítomností pozorovaného Hopkinsonova vrcholu[15] na ZFC křivkách pro všechny studované systémy (NA, SA1, SA2 i SA1_OX) (viz obr. 2 a 5a v příloze D), který je pozorován v případě transformace z magnetického uspořádaného stavu do paramagnetického (*Dunlop a Özdemir*, 1997), což je případ právě hausmanitu.

Dosažené výsledky poukazují na fakt, že nárůst magnetické odezvy pod ~40 K (viz obr. 2 a 5a v příloze D) je důsledkem minoritní přítomnosti hausmanitu ve studovaných systémech (NA, SA1, SA2, SA1_OX). Hausmanit vstupuje do ferimagnetického stavu kolem inkriminované teploty, což je doprovázeno nárůstem jeho magnetické odezvy pod ~40 K, která modifikuje nízkoteplotní magnetickou odezvu celého systému (NA, SA1, SA2, SA1_OX) s intenzitou odpovídající přítomnosti hausmanitu.

Podíváme-li se na studii provedenou *Petrakovski a kol.* (2001) pro synteticky připravené nestechiometrické alabandity bohatší na mangan (tj. Mn_xS, $1 \leq x \leq 1{,}25$), můžeme vyslovit závěr

[15] Viz schématické znázornění toho vrcholu na obr. 8.

směrem k této studii. Systémy studované *Petrakovski a kol.* (2001) mají stejné či velmi podobné nízkoteplotní magnetické chovaní pod ~40 K jaké pozorujeme pro vzorky NA, SA1, SA2 a SA1_OX. *Petrakovski a kol.* (2001) připisují tento nárůst magnetické odezvy přítomnosti charakteristického feromagnetického přechodu v nestechiometrických alabanditech a nikoliv nečistotě. Lze se však domnívat, že nárůst magnetické odezvy je v tomto případě opět způsoben pouhou přítomností ferimagnetické nečistoty v podobě hausmanitu. Ten vzniká nejpravděpodobněji v průběhu syntézy těchto alabanditů bohatších na mangan (tj. Mn_xS, $1 \leq x \leq 1{,}25$), kde nadstechiometrický mangan nevstupuje do struktury alabanditu, ale reakcí s kyslíkem vytváří oxidy manganu zahrnující i hausmanit. Tomuto závěru přispívá i pozorovaný Hopkinsonův vrchol na ZFC křivkách[16] pro všechny nestechiometrické alabandity studované *Petrakovski a kol.* (2001), kterému v citované práci nebyla věnována pozornost a který nyní můžeme interpretačně připsat právě přechodu z ferimagnetického do paramagnetického stavu hausmanitu. Potom korelace mezi mírou nárůstu magnetizace a koncentrací nadstechiometrického manganu je způsobena přítomností hausmanitu a nikoliv nestechiometrií těchto systémů ve studii *Petrakovski a kol.* (2001).

Předložená práce v Příloze D tedy vrhá stín pochybnosti na možné magnetické aplikace charakteristického znaku při ~40 K pro nestechiometrické alabandity bohatších na mangan studované *Petrakovski a kol.* (2001).

[16] Viz obr. 2 ve studii provedené *Petrakovski a kol*. (2001).

Laboratorní simulace kosmického zvětrávání prostřednictvím kontrolovaného růstu nanočástic železa na povrchu minerálu olivínu

Příloha E

Kosmické zvětrávání je proces, kdy je povrch vesmírných těles bez atmosféry neustále vystaven proudu slunečního větru (ionizovaného vodíku – protonů) a dopadům drobných prachových částic (mikrometeoritů), čímž dochází k modifikaci fyzikálních, chemických i mineralogických vlastností původního povrchu těchto těles. Souhrnné i zaměřené vědecké práce ukazují, že vlivem kosmického zvětrávání na povrchu kosmických těles dochází k procesům rozrušení krystalové mříže, bodovému natavení a vypařování hornin. Během následné depozice par pak dochází v povrchových vrstvách železo–obsahujících kosmických materiálů k tvorbě sklovité povrchové vrstvy obohacené o nanočástice redukovaného železa ($npFe^0$). Reflektanční spektra (v optické, ultrafialové a infračervené oblasti) následně vykazují buď méně výrazné absorpční pásy obsažených silikátů (olivínu, pyroxenu) s pozitivním sklonem k vyšším vlnovým délkám či pouze pozitivní sklon u kosmických těles chudých na zmíněné silikáty (obr. 9) (*McCord a Johnson*, 1970; *Adams a McCord*, 1973; *McCord a Adams*, 1973; *Pieters a kol.*, 2000; *Noble a kol.*, 2001; *Sasaki a kol.*, 2001; *Hapke*, 2001; *Chapman*, 2004; *Marchi a kol.*, 2005; *Lazzarin a kol.*, 2006).

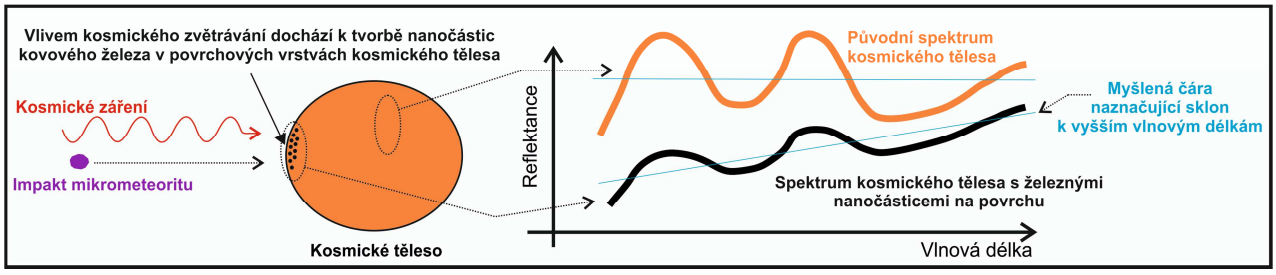

Obr. 9. Schématické znázornění kosmického zvětrávání a vlivu na reflektanční spektrum.

Pro laboratorní simulaci kosmického zvětrávání se využívá dvou metod, založených buď na krátce trvajícím laserovém ozáření, nebo na bombardování povrchu studovaného minerálu ionty (*Marchi a kol.*, 2005; *Brunetto a kol.*, 2006; *Lazzarin a kol.*, 2006). Avšak tyto metody neposkytují dostatečnou kontrolu jak ve velikostní distribuci vznikajících $npFe^0$, tak ani v jejich koncentraci na povrchu (*Brunetto a kol.*, 2006). Z tohoto pohledu je kvantitativní studie kosmického zvětrávání těžko proveditelná. Pouze metody založené na tvorbě $npFe^0$ v substrátu pórovitého silikagelu s póry o různé velikosti umožní ovlivnit velikostní distribuci $npFe^0$, a tedy i kvantitativní analýzu vlivu $npFe^0$ na spektrální vlastnosti (*Allen a kol.*, 1996; *Noble a kol.*, 2007).

Předložený článek (příloha E), který byl přijat (9. 4. 2014) k publikaci v časopise ICARUS, věnuje pozornost zmíněnému fenoménu kosmického zvětrávání a jeho laboratorní simulaci. Konkrétněji motivací autorů článku bylo využít bohaté zkušenosti na pracovišti autora této dizertační práce s přípravou a následnou charakterizací nanočástic na bázi železa a tyto zkušenosti aplikovat v podobě nového přístupu k laboratorní simulaci kosmického zvětrávání, která umožní kvantitativní analýzu. Sekundární motivace spočívala v rovině využití nového přístupu ke studiu vlivu $npFe^0$ na reflektanční spektra minerálu olivínu, jakožto reprezentativního příkladu silikátového minerálu, který se vyskytuje v planetkách (S komplex) či u chondritů a podléhá přirozenému kosmickému zvětrávání ve vesmíru.

V článku je představena nová dvoukroková metoda přípravy analogů kosmického zvětrávání na minerálu olivínu, založená na teplotní dekompozici, přičemž požadované velikostní distribuce i koncentrace $npFe^0$ v povrchových vrstvách je docíleno pomocí změn teploty a doby žíhání studovaného systému. V prvním kroku je olivín žíhán za přístupu kyslíku vedoucímu

k částečné oxidaci železných iontů ve struktuře, zvláště těch nacházejících se blízko povrchu studovaného systému. Oxidace Fe^{2+} iontů vede k nábojové nerovnováze ve struktuře způsobující difuzi Fe^{3+} atomů směrem k povrchu, kde precipitují ve formě Fe^{3+} oxidů železa (obr. 10). Získání $npFe^{0}$ v povrchových vrstvách studovaného systému se dosahuje prostřednictvím druhého kroku, kdy povrchové nanočástice Fe^{3+} oxidů železa jsou redukovány žíháním v redukční vodíkové atmosféře na požadované $npFe^{0}$. Výsledkem této dvoukrokové metody je povrch studovaného systému změněn na sklovitou vrstvu s $npFe^{0}$.

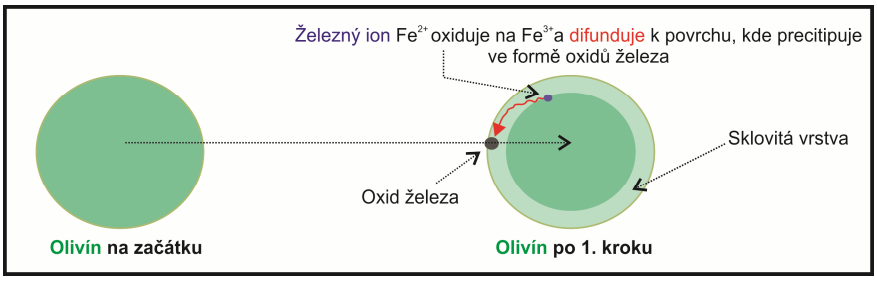

Obr. 10. Schématické znázornění prvního kroku přípravy analogů kosmického zvětrávaní pro minerál olivín. Žíháním v peci za přístupu kyslíku dochází k tvorbě sklovité vrstvy s oxidy železa.

Zmíněný postup přípravy analogů kosmického zvětrávání je ukázán na minerálu olivínu, kdy je získán $npFe^{0}$ v povrchových vrstvách (viz snímky z transmisní elektronové mikroskopie obr. 2 a 3 v příloze E) podobným těm, které známe u přírodně kosmicky zvětralých systémů (*Pirters a kol.*, 2000; *Hapke*, 2001). Skutečnost, že se podařilo povrchově modifikovat zrna minerálu olivínu systémem $npFe^{0}$, je prokazována na základě těchto poznatků:

1. mřížkové rozteče těchto $npFe^{0}$ mají hodnotu typickou pro kovové železo (viz obr. 4 v příloze E),

2. elementární analýza těchto částic ukazuje pouze kovové železo bez přítomnosti kyslíku (viz obr. 5 v příloze E) a
3. Mössbauerova spektroskopie ukazuje ve studovaném systému pouze přítomnost minerálu olivínu a kovového železa (viz obr. 6 v příloze E).

Kvantitativní analýza získaných výsledků na minerálu olivínu ukazuje, že pozorované změny reflektančních spekter jsou důsledkem pouze míry koncentrace $npFe^0$ v povrchových vrstvách. Porovnáním se spektrem pro čistý olivín je patrný trend, že s rostoucí koncentrací $npFe^0$ jsou méně výrazné absorpční pásy minerálu olivínu s pozitivním sklonem k vyšším vlnovým délkám (viz obr. 7 v příloze E). Dále je patrná lineární vazba mezi mírou koncentrace $npFe^0$ v povrchových vrstvách olivínu a absorpčním pásmem 1 μm (viz obr. 8 v příloze E) a logaritmický trend jak mezi mírou koncentrace $npFe^0$ a odrazivostí, tak 1 μm absorpčním pásmem a pozitivním sklonem k vyšším vlnovým délkám (viz obr. 9 v příloze E).

Úspěšné navrhnutá dvoukroková metoda tvorby analogů kosmického zvětrávaní, představené na minerálu olivínu, umožňuje aplikovat tuto metodu i pro jiné systémy a studovat vliv velikosti a koncentrace $npFe^0$ na jejich reflektanční spektra. Nad rámec článku v příloze E byla dvoukroková metoda aplikovaná na minerál pyroxen a přírodní extraterestriální vzorek meteoritu. Tyto prvotní studie dávají uspokojivé výsledky v záměrné povrchové modifikaci systémem $npFe^0$. To dokládá, že nová dvoukroková metoda simulace kosmického zvětrávání je reálně využitelná pro kvantitativní studium tohoto jevu.

Použitá literatura

Adams, J.B., McCord, T.B. (1973), Vitrification darkening in the lunar highlands and identification of Descartes material at the Apollo 16 sites, *Proceedings of the Lunar and Planetary Science Conference*, 4, 163–177.

Allen, C.C., Morris, R.V., McKay, D.S. (1996), An experimental analog to maturing lunar soil, *Proceedings of the Lunar and Planetary Science Conference*, 37, 13–14.

Brunetto, R., Romano, F., Blanco, A., Fonti, S., Martino, M., Orofino, V., Verrienti, C. (2006) Space weathering of silicates simulated by nanosecond pulse UV excimer laser, *Icarus*, 180, 546–554.

Cornell, R.M., Schwertmann, U. (2003), The Iron Oxides, 2nd Edition. *Wiley-VCH Verlag GmbH & Co. KGaA*, Weinheim, Germany.

Čuda, J., Zbořil, R., Schneeweiss, O., Tuček, J., Procházka, V., Mašláň, M., Tuček, P. (2010), Mossbauer study and macroscopic/global magnetic behavior of powdered ilmenite ($FeTiO_3$) sample, Mossbauer Spectroscopy in Materials Science, AIP Conference Proceedings, Editor: J. Tuček, M. Miglierini, 1258, 55–67, *International Conference on Mossbauer Spectroscopy in Materials Science–2010*.

Dwight, K., Menyuk, N. (1960) Magnetic properties of Mn_3O_4 and the canted spin problem, *Phys. Rev.*, 119, 1479–1479.

Dunlop, D.J., Özdemir, Ö. (1997), Rock magnetism: Fundamentals and frontiers, 1. Edition., *Cambridge University Press.*

Fabian, K., McEnroe, S.A., Robinson, P., Shcherbakov, V.P. (2008), Exchange bias identifies lamellar magnetism as the origin of the natural remanent magnetization in titanohematite with ilmenite exsolution from Modum, Norway, *Earth Planet. Sci. Lett*., 268, 339–353.

Fabritchnyi, P.B., Korolenko, M.V., Afanasov, M.I., Danot M., Janod E. (2003), Mössbauer characterization of tin dopant ions in the antiferromagnetic ilmenite $MnTiO_3$, *Solid State Commun.* 125, 341–346.

Frankel, R.B. (1974), Phase Transitions in antiferromagnets in external magnetic fields: Mössbauer spectroscopy, *Mössbauer Effect Methodology*, 151–180.

Gattacceca, J., Rochette, P., Lagroix, F., Mathé, P.E., Zanda, B. (2011), Low temperature magnetic transition of chromite in ordinary chromites, *Geophys. Res. Lett.*, 38, L10203.

Greenwood, N.N., Gibb, T.C. (1971), Mössbauer Spectroscopy, *Chapman & Hall Ltd.*, London, UK, 1971.

Chapman, C.R. (2004), Space weathering of asteroid surfaces, *Annual Reviews.*, 32, 539-567.

Chen Y.L., Yang, D.P. (2007), Mössbauer Effect in Lattice Dynamics: Experimental Techniques and Applications, *Weinheim: WILEY-VCH Verlag GmbH & Co. KGaA*, Germany.

Hapke, B. (2001), Space weathering from Mercury to the asteroid belt. J. Geophys. Res., 106, 10039–10073.

Harrison, R.J, McEnroe, S.A., Robinson, P., Carter-Stiglizt, B., Palin, E.J., Kasama, T. (2008), Low-temperature exchange coupling between Fe_2O_3 and $FeTiO_3$: Insight into the mechanism of giant exchange bias in a natural nanoscale intergrowth, *Phys. Rev. B*, 76, 174436.

Heikens, H.H., Wiegers, G.A., Van Bruggen, C.F. (1977), On the nature of a new phase transition in α–MnS, *Solid State Commun.*, 24, 205209.

Johnson, C.E. (1989), The Mössbauer effect and magnetic phase transitions, *Hyperfine Interact.*, 49, 19–42.

Johnson, C.E. (1996), Characterization of magnetic materials by Mössbauer spectroscopy, *J. Phys. D: Appl. Phys.*, 29, 2266–2273.

Kasama, T., Dunin-Borkowski, R.E., Asaka, T., Harrison, R.J., Chong, R.K.K., McEnroe, S.A., Simpson, E.T., Matsui, Y., Putnis, A. (2009), The application of Lorentz transmission electron microscopy to the study of lamellar magnetism in hematite-ilmenite, *Am. Mineral.*, 94, 262–269.

Kin, W., Park, I.J., Kim, C.S. (2008), Ferromagnetism in a mixture of antiferromagnetic $FeTiO_3$ and alpha-Fe_2O_3 as observed by using Mossbauer Spectroscopy, *J. Korean Phys. Soc.*, 53, 1529–1533.

Kletetschka, G., Wasilewski, P.J., Taylor, P.T. (2002) The role of hematite-ilmenite solid solution in the production of magnetic anomalies in ground- and satellite-based data. *Tectonophysics*, 347, 167–177.

Kohout, T., Kosterov A., Jackson, M., Pesonen, L.J., Kletetschka, G., Lehtinen, M. (2007), Low-temperature magnetic properties of the Neuschwanstein EL6 meteorite, *Earth Planet. Sci. Lett.*, 261, 143–151.

Lazzarin, M., Marchi, S., Moroz, L.V., Brunetto, R., Magrin, S., Paolicchi, P., Strazzulla, G. (2006), Space weathering in the main asteroid belt: The big picture, *Astrophys. J. Lett.*, 2006, 647, L179–L182.

Marchi, S., Brunetto, R., Magrin, S., Lazzarin, M., Gandolfi, D. (2005), Space weathering of near-Earth and main belt silicate-rich asteroids: observations and ion irradiation experiments, *Astron. Astrophys.*, 443, 769–775.

McCord, T.B., Adams, J.B. (1973), Progress in remote optical analysis of lunar surface composition. Moon, 7, 453–474.

McCord, T.B., Johnson, T. (1970), Lunar spectral reflectivity (0.30 to 2.50 microns) and implications for remote mineralogical analysis, *Science*, 169, 855–858.

McEnroe, S.A., Harrison, R.J., Robinson, P., Langenhorst, F. (2002), Nanoscale haematite–ilmenite lamellae in massive ilmenite rock: An example of "rock magnetism" with implications for planetary magnetic anomalies, *Geophys. J. Int.*, 151, 890–912.

McEnroe, S.A., Langenhorst, F., Robinson, P., Bromiley, G.D., Shaw, C.S.J. (2004), What is magnetic in the lower crust?, *Earth Planet. Sci. Lett.*, 226, 175–192.

McEnroe, S.A., Carter-Stiglitz, B., Harrison, R.J., Robinson, P., Fabian, K., McCammon, C. (2007), Magnetic exchange bias of more than 1 Tesla in a natural mineral intergrowth, *Nature Nanotechnol.*, 2, 631–634.

Noble, S.K., Pieters, C.M., Keller, L.P. (2007), An experimental approach to understanding the optical effects of space weathering. *Icarus*, 192, 629–642.

Noble, S.K., Pieters, C.M., Taylor, L.A., Morris, R.V., Allen, C.C., McKay, D.S., Keller, L.P. (2001), The optical properties of the finest fraction of lunar soil: Implications for space weathering, *Meteorit. Planet. Sci.*, 2001, 36, 31–42.

Nord, Jr., G.L., Lawson C.A. (1989), Order-disorder transition-induced twin domains and magnetic properties in hematite-ilmenite, *Am. Mineral.*, *74*, 160–176.

Nord, G.L., Lawson, C.A. (1992), Magnetic properties of ilmenite70-hematite30: Effect of transformation-induced twin boundaries, *J. Geophys. Res.*, 97, 10897–10910.

Pankhurst, Q.A., Pollard, R.J. (1990), Mössbauer spectra of antiferromagnetic powders in applied fields, *J. Phys.: Condens. Matter*, 2, 7329–7337.

Pankhurst, Q.A. (1991), Anisotropy field measurement in barium ferrite powders by applied field Mössbauer spectroscopy, *J. Phys.: Condens. Matter*, 3, 1323–1335.

Petrakovski, G.A., Ryabinkina, L.I., Abramova, G.M., Velikanov, D.A., Bovina, A.F. (2001), Antiferromagnet–ferromagnet transition in α-MnxS manganese sulfides, *Phys. Solid State*, 43, 493–495 (přeloženo z *Fizika Tverdogo Tela*, 43, 474–476).

Pearce, C.I., Pattrick, R.A.D., Vaughan, D.J. (2006), Electrical and Magnetic Properties of Sulfides, *Rev. Mineral. Geochem.*, 61, 127-180.

Pieters, C.M., Taylor, L.A., Noble, S.K., Keller, L.P., Hapke, B., Morris, R.V., Allen, C.C., McKay, D.S., Wentworth, S. (2000), Space weathering on airless bodies: Resolving a mystery with lunar samples, *Meteorit. Planet. Sci.*, 35, 1101–1107.

Robie, R.A., Hemingway, B.S. (1985), Low-temperature molar heat capacities and entropies of MnO_2 (pyrolusite), Mn_3O_4 (hausmannite), and Mn_2O_3 (bixbyite), *J. Chem. Thermodyn.*, 17, 165–181.

Robinson, P., Harrison, R.J., McEnroe, S.A., Hargraves, R.B. (2002), Lamellar magnetism in the haematite-ilmenite series as an explanation for strong remanent magnetization. *Nature*, 418, 517–520.

Robinson, P., Harrison, R.J., McEnroe, S.A., Hargraves, R.B. (2004), Nature and origin of lamellar magnetism in the hematite-ilmenite series, *Am. Mineral.*, 89, 725–747.

Robinson, P., Heidelbach, F., Hirt, A.M., McEnroe, S.A., Brown, L.L. (2006), Crystallographic-magnetic correlations in single-crystal haemo-ilmenite: new evidence for lamellar magnetism, *Geophys. J. Int.*, 165, 17–31.

Tuček, J. (2008), Magnetismus nanočástic oxidů železa a dvojného perovskitu typu Sr_2FeRuO_6, disertační práce, Univerzita Palackého v Olomouci.

Sasaki, S., Nakamura, K., Hamabe, Y., Kurahashi, E., Hiroi, T. (2001), Production of iron nanoparticles by laser irradiation in a simulation of lunar-like space weathering, *Nature*, 410, 555-557.

Vandenberghe, R.E., de Grave, E., Landuydt, C. (1990), Some aspects concerning the characterization of iron oxides and hydroxides in soils and clays, *Hyperfine Interact.*, 53, 175–195.

Wang, H., Salveson, I. (2005), A review on the mineral chemistry of the non-stoichiometric iron sulphide, $Fe_{1-x}S$ ($0 \leq x \leq 0.125$): polymorphs, phase relations and transitions, electronic and magnetic structures, *Phase Transit.*, 78, 547–567.

Zboril, R., Mashlan, M., Petridis, D. (2002), Iron(III) oxides from thermal processes-synthesis, structural and magnetic properties, Mossbauer spectroscopy characterization, and applications, *Chem. Mater.*, 14, 969–982.

Příloha A

Čuda, J., Zbořil, R., Schneeweiss, O., Tuček, J., Procházka, V., Mašláň, M., Tuček, P.:

Mössbauer study and macroscopic/global magnetic behavior of powdered ilmenite ($FeTiO_3$) sample

MSMS 2010, *Conference Proceedings*, 55–67 (2010)

Mössbauer Study and Macroscopic/Global Magnetic Behavior of Powdered Ilmenite ($FeTiO_3$) Sample

J. Cuda[a], R. Zboril[a, b], O. Schneeweiss[c], J. Tucek[a, d], V. Prochazka[a], M. Maslan[a, d] and P. Tucek[e, f]

[a]*Centre for Nanomaterial Research, Palacky University, Slechtitelu 11, 783 71 Olomouc, Czech Republic*
[b]*Department of Physical Chemistry, Faculty of Science, Palacky University, 17. listopadu 1192/12, 771 46 Olomouc, Czech Republic*
[c]*Institute of Physics of Materials, Academy of Sciences of the Czech Republic, Zizkova 22, 616 62 Brno, Czech Republic*
[d]*Department of Experimental Physics, Faculty of Science, Palacky University, 17. listopadu 1192/12, 771 46 Olomouc, Czech Republic*
[e]*Department of Mathematical Analysis and Mathematical Applications, Faculty of Science, Palacky University, 17. listopadu 1192/12, 771 46 Olomouc, Czech Republic*
[f]*Department of Geoinformatics, Faculty of Science, Palacky University, Svobody 26, 771 46 Olomouc, Czech Republic*

Abstract. In this article, the commercial synthetic powdered sample of ilmenite ($FeTiO_3$) has been re-examined by Mössbauer spectroscopy in the paramagnetic regime from 77 K to 280 K and in a magnetically ordered state below 57 K. The effective vibrating mass and the Debye temperature was found to be (78 ± 3) amu and (359 ± 27) K, respectively. The two sextet components were used for correct fitting of the Mössbauer spectra recorded at 5 K and 45 K in an external magnetic field of 5 T. Moreover, the macroscopic magnetic measurements were carried out by an MPMS XL–7 magnetometer to determine a temperature dependence of the molar susceptibility and hysteresis loops of this sample. The Mössbauer spectra and magnetization measurements confirm that below the ordering temperature of ilmenite, it behaves as a non-ideal antiferromagnetic material with a significant magnetic hardening at low temperatures. In addition, the magnetic molar susceptibility follows a Curie-Weiss law with $C_m = 5.8 \times 10^{-5}$ K m^3/mol, and Weiss temperature $\theta_p = 30.6$ K.

Keywords: Ilmenite, $FeTiO_3$, zero-field and in-field Mössbauer spectroscopy, hyperfine interactions, low-temperature magnetic regime.
PACS: 76.80.+y, 75.50.Ee

INTRODUCTION

The iron titanium oxide has the chemical formula of $FeTiO_3$ and it occurs as an igneous and metamorphic hard rock with a typical dark brown or black color. In addition, it forms solid solutions in combination with other phases (hematite in most cases) in which it governs unusual magnetic properties of these compositions such as in the hematite-ilmenite solid solutions. This solid solution exhibits a significant

exchange bias phenomenon with an exchange bias field of up to 1 T and anomalously high thermoremanent magnetization being stable for a long period of time [1,2].

Crystal structure of $FeTiO_3$ can have three possibilities depending on the temperature and pressure conditions [3,4]. Among them, ilmenite structure with space group *R*–3 is regarded as the most stable phase at ambient conditions. There are alternating layers of Ti and Fe ions perpendicular to crystallographic *c*-axis with oxygen layers between them. The neutron diffraction data have been discussed in several papers [5-8] proposing that $FeTiO_3$ has an antiferromagnetic magnetic structure below its Néel temperature in the range of 56-58 K with magnetic moments of Fe ions lying parallel or antiparallel along the *c*-axis. At low temperatures, magnetic moments are still collinear but oblique from *c*-axis with a small angle of about 2°.

A metamagnetic phase transition at low temperatures is also observed in $FeTiO_3$. $FeTiO_3$ undergoes the metamagnetic transition under about 8 T at 4.2 K and the whole phase diagram was published in [9]. Time evolution of the magnetic response through this transition was investigated in [10].

A nominal valence state of Ti and Fe ions is 4+ and 2+, respectively, which has been confirmed in [11]. On the other hand, it is possible to find oxidation states Ti^{3+} and Fe^{3+} in the natural ilmenite and synthetic specimen due to close energy levels between Fe^{2+} a Ti^{4+} ions [3,12-15].

In the present paper, we have re-examined the Mössbauer spectra in the paramagnetic and also in the antiferromagnetic regime together with the results acquired from the magnetization measurements. From the temperature evolution of the zero-field Mössbauer spectra, we have derived the effective vibrating mass and the Debye temperature and we show that ilmenite does not behave as a collinear antiferromagnetic material as evidenced by a deconvolution of the in-field Mössbauer spectra and temperature behavior of the molar susceptibility and coercivity.

EXPERIMENTAL DETAILS

The commercial synthetic powdered specimen of $FeTiO_3$ was bought from Sigma Aldrich Company with sizes of particles being less than 150 microns. Before other studies, we have checked a crystal structure and stoichiometry of this sample by X-ray powder diffraction (XRD) and X-ray fluorescence (XRF), respectively. XRD experiments were performed with a PANalytical X´Pert PRO instrument (CoK_α radiation) equipped with an X´Celerator detector. Samples were spread on a zero-background Si slides and step-scanned in the 2θ range of 10–100° in steps of 0.017° for 720 s per step. The XRF analysis has been carried out by an X-ray Fluorescence Spectrometer Wavelength dispersive XRF S4 Pioneer. The zero-field Mössbauer spectra were recorded in the temperature interval from 5 to 280 K in a constant acceleration mode with a 50 mCi $^{57}Co(Rh)$ source. The values of the center shift are reported with respect to α-Fe at room temperature. The in-field Mössbauer measurements were performed in a constant acceleration mode when the sample was placed in a cryomagnetic system (Oxford Instruments) at a temperature of 5 and 45 K and exposed to an external magnetic field of 5 T, applied parallel to the direction of γ-rays. To fit the collected Mössbauer spectra, MossWinn software package has been employed. A superconducting quantum interference device (SQUID, MPMS XL-7,

Quantum Design) has been used for the magnetic measurements. The hysteresis loops were recorded in external magnetic fields of up to ± 5 T. The temperature dependence of the magnetic molar susceptibility was measured in the settle mode in the temperature range from 5 to 300 K and in an external magnetic field of 0.1 T.

RESULTS AND DISCUSSION

XRD and XRF Analysis

The X-ray pattern of the investigated sample is depicted in Fig. 1. It shows the presence of crystalline ilmenite structure of *R*–3 space group and peaks corresponding to this structure are marked by arrows (JCPDS card No. 01-075-1209). As far as the stoichiometry is concerned, the analysis of the XRF spectrum indicates that titanium and iron atoms are present in the ratio of 1.02 in the studied sample in contrast to 1 expected for precisely stoichiometric specimen. That implies a presence of either a small amount of vacant sites of iron or a small amount of another phase in the sample which may increase this ratio and/or both two possibilities occur simultaneously. According to the XRD pattern, TiO_2 probably seems to be another phase and its presence was determined to be less than 1%. Thus, our studied sample can be considered as an almost single-phase sample because the presence of vacancies and/or impurities (TiO_2) is negligible as evidenced from the X-ray pattern and stoichiometry study.

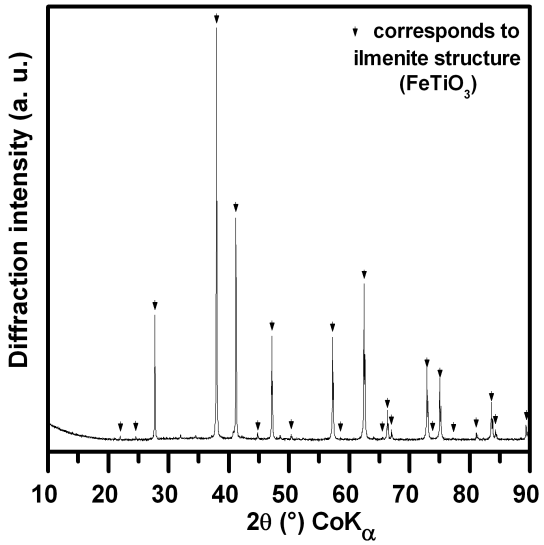

FIGURE 1. XRD pattern of the powdered $FeTiO_3$ sample.

Mössbauer Study

In order to study the temperature dependence of the physical properties of $FeTiO_3$, we measured the Mössbauer spectra in the paramagnetic region above the Néel temperature. Each of 12 Mössbauer spectra were recorded in the temperature range from 77 K to 280 K and they were fitted well by means of one symmetric quadrupole doublet indicating an absence of any texture in our sample. The Mössbauer spectra at 77 K and at 280 K are depicted in Fig. 2 and relevant parameters of the temperature evolution of the quadrupole doublet are listed in Table 1. It is clearly seen that the value of the center shift at 280 K (i.e., 1.10 mm/s) corresponds to ferrous component of iron in spin state of $S = 2$ which is in agreement with a presumption for iron ions in $FeTiO_3$.

Further, we constructed the temperature dependences of the quadrupole splitting ΔE_Q and the center shift δ. The temperature behavior of these hyperfine parameters is shown in Fig. 3. We observe a quite strong temperature dependence of the quadrupole splitting parameter (see Fig. 3a). In principle, there are two main sources which can contribute to the electric field gradient (EFG) if the electric charge distribution around a Mössbauer nucleus is non-spherical [16,17]. The first term arises from a lattice contribution $(V_{zz})_{lat}$ where the dominant source for the EFG tensor is governed by an electric charge belonging to atoms surrounding the probed Mössbauer atom, however, this term is hardly affected by temperature. On the other hand, the second one which can display a temperature dependence is called the valence electron contribution $(V_{zz})_{val}$ and reflects an anisotropic electron distribution in the valence shell of the Mössbauer atom. Therefore, in our case, $(V_{zz})_{val}$ is the main source for EFG tensor of the Mössbauer-active atom in $FeTiO_3$. Moreover, the temperature dependence of the center shift has been taken into account and is illustrated in Fig. 3b. Employing a linear curve to account for the decrease in δ with raising temperature, the derived value of the correlation coefficient of the linear regression is found to be 0.99. This value of the correlation coefficient is larger than 0.95 which is the lowest limit value for mathematical acceptance of the linear regression. Therefore, the effective vibrating mass M_{eff} can be calculated according to the expression valid for a classical high-temperature limit [17,18], i.e.,

$$\frac{\mathrm{d}\delta}{\mathrm{d}T} = -\frac{3}{2}\frac{E_\gamma k_B}{M_{eff}c^2}, \qquad (1)$$

where T denotes the temperature, E_γ represents the energy of the Mössbauer gamma-photon, k_B stands for the Boltzmann constant, M_{eff} is the effective vibrating mass and c corresponds to the speed of light. From the observed temperature behavior of δ, M_{eff} was evaluated to be (78 ± 3) amu for the Mössbauer probed atom. If M_{eff} is determined, the Debye temperature Θ_D can be calculated on the basis of the formula of the recoil-free fraction. It is known that an area $A(T)$ under the absorption resonance curve of a Mössbauer spectrum is connected with a recoil-free fraction $f(T)$ and the temperature evolution of $f(T)$ can be accompanied by the temperature behavior of $A(T)$. Then

$$\frac{\mathrm{d}\ln A}{\mathrm{d}T} = \frac{\mathrm{d}\ln f}{\mathrm{d}T}. \qquad (2)$$

The Debye temperature Θ_D was determined using a high temperature limit of the recoil free fraction because we observed almost a linear character of the natural logarithm plots of the resonance areas (normalized to 77 K) at the temperature range of $77 \leq T \leq 280$ K as evidenced in Fig. 3c. Then, with regard to Eq. 2, we can write that

$$\frac{\mathrm{d}\ln A}{\mathrm{d}T} = -\frac{6E_R}{k_B\Theta_D^2} = -\frac{3E_\gamma}{k_B M_{eff} c^2 \Theta_D^2}, \qquad (3)$$

where E_R represents the recoil energy. It was found that Θ_D is (359 ± 27) K by means of the linear regression through the experimental data (solid line in Fig. 3c) and by substitution of $M_{eff} = 78$ amu in Eq. 3 derived from the second-order Doppler shift described by Eq. 1. The Debye temperature points to the strength of the bonds between the lattice and Mössbauer-active atom and is higher than 300 K reported for most metallic materials. However, we were unable to found out any estimation of it by help of Mössbauer spectroscopy in the literature. Nevertheless, the determined Debye temperature for $FeTiO_3$ can be compared with that for materials with related crystal structures such as ilmenite-hematite solid solution and tin-doped ilmenite $MnTiO_3$. For $(FeTiO_3)_{0.5}$-$(Fe_2O_3)_{0.5}$ solid solution, the Debye temperature was found to be equal to (355 ± 5) K [19] and (370 ± 10) K for tin-doped ilmenite $MnTiO_3$ [20].

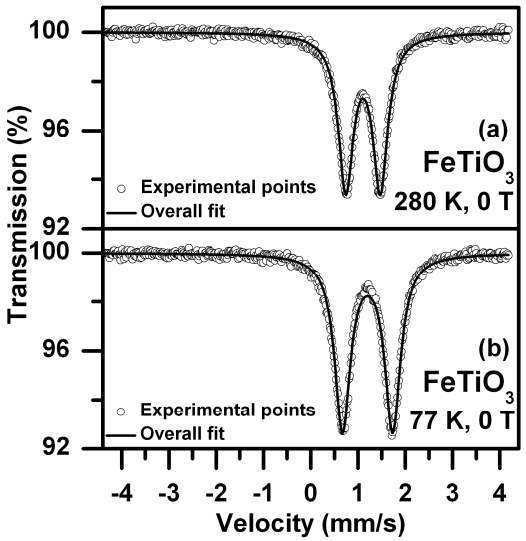

FIGURE 2. Mössbauer spectra of the powdered $FeTiO_3$ sample measured at 280 K (a) and 77 K (b).

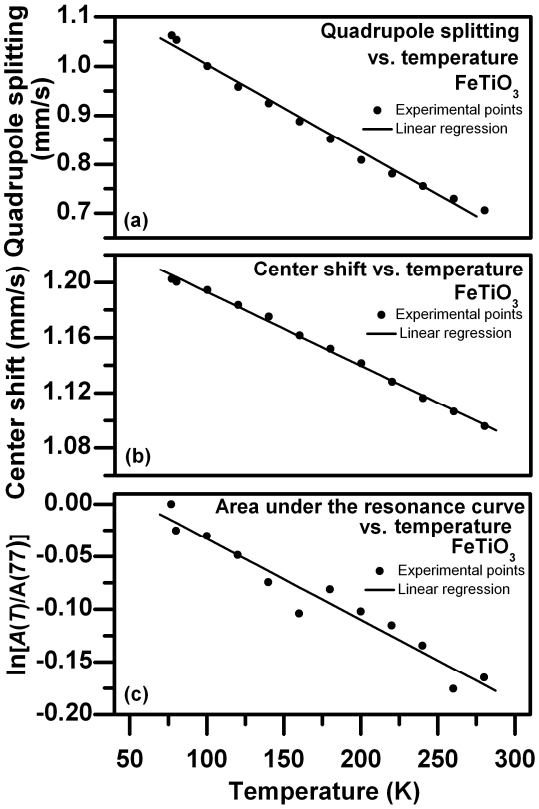

FIGURE 3. Temperature behavior of the quadrupole splitting parameter in the temperature range from 77 K to 280 K (a), temperature dependence of the center shift parameter in the temperature range from 77 K to 280 K (b), natural logarithm of area under the Mössbauer absorption resonance curve (normalized to 77 K) of the powdered $FeTiO_3$ sample at various temperatures (c).

TABLE 1. Summary of parameters for the powdered $FeTiO_3$ sample derived from the measured Mössbauer spectra in the paramagnetic region where δ corresponds to the center shift, ΔE_Q represents the quadrupole splitting, Γ is the linewidth, $A(T)$ is the resonant area under Mössbauer spectrum at a temperature T, M_{eff} refers to an effective mass of the Mössbauer probed atom and Θ_D is the Debye temperature of the solid.

	77 K	**280 K**	
δ (mm/s)	1.20 ± 0.01	1.10 ± 0.01	
ΔE_Q (mm/s)	1.06 ± 0.01	0.71 ± 0.01	
Γ (mm/s)	0.40 ± 0.01	0.39 ± 0.01	
$d\Delta E_Q/dT$ (mm/s K^{-1})			-1.77×10^{-3}
$d\delta/dT$ (mm/s K^{-1})			-5.34×10^{-4}
M_{eff} (amu)			78 ± 3
$d\ln[A(T)/A(77\ K)]/dT$ (K^{-1})			-7.70×10^{-4}
Θ_D (K)			359 ± 27

Now, we will briefly focus on the Mössbauer spectra in the magnetic ordered state of $FeTiO_3$ below 57 K. The zero-field Mössbauer spectra at 45 T and 5 K are shown in Fig. 4a and 4b. Looking at the measured Mössbauer spectra, it is evident that the individual peaks of the sextet are significantly overlapped due to the high value of the quadrupole splitting and relatively small value of the magnetic hyperfine field. Further, the point symmetry of the Fe^{2+} sites which are crystallographically equivalent suggests that the electric field gradient (EFG) is axially symmetric (*i.e.*, $\eta = 0$, where η is the asymmetry parameter) and the hyperfine magnetic field is parallel to V_{zz} (*i.e.*, the diagonal element of the electric field gradient tensor along the z principal axis) [21]. Therefore, to fit correctly the low-temperature Mössbauer spectra of our investigated sample, we used a model which is implemented in the MossWinn program involving a static Hamiltonian [22] for mixed magnetic and quadrupole interactions in order to determine hyperfine parameters of Fe^{2+} ions. They are summarized in Table 2. A profile of the Mössbauer spectrum recorded at 5 K is comparable with the spectrum obtained by Grant et al. [21]. From the analysis of the measured Mössbauer spectrum, the quadrupole splitting was determined to be 1.44 mm/s at 5 K which is the same value reported by Grant et al. at the given temperature [21]. The center shift is also consistent with the previously published value.

It is worth to mention that the hyperfine magnetic field involves several contributions. Apart from usual Fermi-contact term, for Fe^{2+} ions, orbital and dipolar hyperfine magnetic terms do contribute to the value and the direction of the overall hyperfine magnetic field. Thus, below the ordering temperature, the temperature dependence of the hyperfine field do not need to obey the Brillouin function with S = 2. The sign of the hyperfine magnetic field at low temperatures is negative according to analysis of the orbital, dipolar and Fermi-contact contributions to the hyperfine magnetic field in $FeTiO_3$ [21,23]. In such a case, the magnetic hyperfine field at the Mössbauer-active nucleus is oriented antiferromagnetically to direction of an applied external magnetic field.

The Mössbauer spectrum at 5 K and 0 T was fitted again by means of six singlets to show the position of each sextet line in the overall fitting. This time, during the fitting procedure, we fixed the relative line intensities to be 2:1:1:2:3:3 for randomly-oriented powdered non-magnetized sample because of a small magnetic hyperfine field and a large quadrupole interactions which cause that the transition from – 3/2 excited state to – 1/2 ground state has a higher energy than the energy corresponding to the transition from + 1/2 excited state to + 1/2 ground state. Furthermore, the width of each six lines was held to have the same value and the difference between the 4^{th} and the 2^{nd} line was held to be equal to the difference between the 5^{th} and the 3^{rd} line. The fitting of this spectrum is depicted in Fig. 4c and the parameters of six singlets are listed in Table 3. The calculated value of the magnetic hyperfine field is equal to 4.3 T from the difference between the 4^{th} and the 2^{nd} line and the calculated quadrupole splitting is equal to 1.45 mm/s from the positions of the 6^{th}, 5^{th}, 2^{nd} and 1^{st} line. These values are in agreement with those derived from the same zero-field Mössbauer spectrum at 5 K fitted by the static Hamiltonian model in the MossWinn software program (see Table 2).

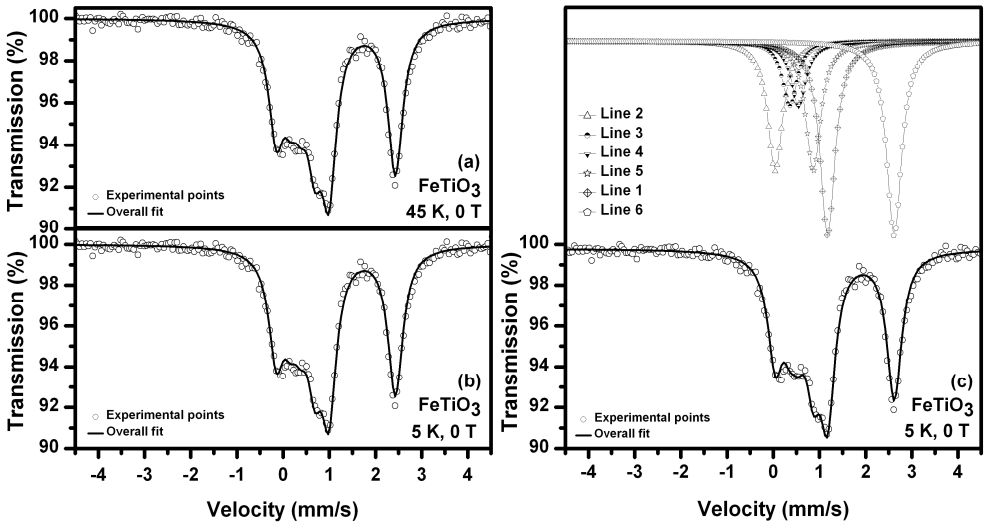

FIGURE 4. The Mössbauer spectrum of the powdered $FeTiO_3$ sample measured at 45 K and 0 T fitted by means of the static Hamiltonian model for mixed magnetic and quadrupole interactions (a), the Mössbauer spectrum measured at 5 K and 0 T fitted by means of the static Hamiltonian model for mixed magnetic and quadrupole interactions (b) and the Mössbauer spectrum at 5 K and 0 T fitted by six singlets (c).

TABLE 2. Hyperfine parameters of the zero-field Mössbauer spectra of the powdered $FeTiO_3$ sample at 5 K and 45 K, where T is the temperature of measurement, δ is the center shift, V_{zz} is the diagonal element of the EFG tensor along the z principal axis, ΔE_Q is the quadrupole splitting, B_{hf} is the magnetic hyperfine field, and Γ is the linewidth.

T (K)	$\delta \pm 0.01$ (mm/s)	$V_{zz} \pm 0.06$ (10^{21} V/m^2)	$\Delta E_Q \pm 0.01$ (mm/s)	$B_{hf} \pm 0.3$ (T)	$\Gamma \pm 0.01$ (mm/s)
5	1.18	8.67	1.44	4.5	0.39
45	1.17	7.90	1.31	4.0	0.40

TABLE 3. Parameters of six singlets used for fitting the zero-field Mössbauer spectrum at 5 K, where δ is the center shift and Γ is the linewidth.

Line from Fig. 4b	Relative intensity	$\delta \pm 0.01$ (mm/s)	$\Gamma \pm 0.01$ (mm/s)
2	2	0.04	0.39
3	1	0.36	0.39
4	1	0.55	0.39
5	2	0.87	0.39
1	3	1.18	0.39
6	3	2.62	0.39

To the best of our knowledge, the Mössbauer spectra of $FeTiO_3$ in external magnetic fields have never been investigated. Fig. 5a and 5b display the Mössbauer spectra measured at 45 K and 5 K, both in an external magnetic field of 5 T. As one can see in Fig. 5, two sextets have been used in order to correctly fit the experimental profiles. Each of the two sextets occupies 50% of overall fitting area of the Mössbauer spectrum at 45 K and 5 K. All the corresponding hyperfine parameters are listed in Table 4 for both spectra. We suggest that the application of the external magnetic

field, applied along the direction of propagation of γ-rays, leads to the separation of magnetic sublattices in the structure of $FeTiO_3$ because the applied magnetic field differently influences the magnetic moments of Fe^{2+} atom situated on the two magnetic sublattices of $FeTiO_3$. Thus, one sextet corresponds to the magnetic moments that lie parallel along the main crystallographic axis and another one belongs to the antiparallel orientation of Fe^{2+} magnetic moments pointing along this axis. The distinguishing of both magnetic sublattices in this almost precisely stoichiometric powdered $FeTiO_3$ implies the imperfect antiferromagnetic behavior below the magnetic ordering temperature. For polycrystalline pure antiferromagnetic material, only one sextet is expected [24]. Note that the value of the quadrupole splitting parameter has changed (e.g., from 1.44 mm/s at 5 K and without external magnetic field to 0.84 mm/s at 5 K and under applied magnetic field of 5 T) upon application of external magnetic field. This indicates that the external magnetic field affects the quadrupole interactions which, due to their significance, cannot be treated as a perturbation to magnetic dipolar hyperfine interactions. The field-induced quadrupole interactions is assumed to be generated by collective magnetic arrangement of atomic magnetic moments when the electric field gradient arises as a consequence of non-zero exchange interaction of effective magnetic field in the place of the Mössbauer-active atom, acting via spin-orbital coupling, which creates an asymmetric distribution of electric charge [24]. Thus, the external magnetic field both aligns the Fe^{2+} ions magnetic moments at the two magnetic sublattices (i.e., separation of magnetic sublattices in the structure of $FeTiO_3$) and modifies quadrupole interactions.

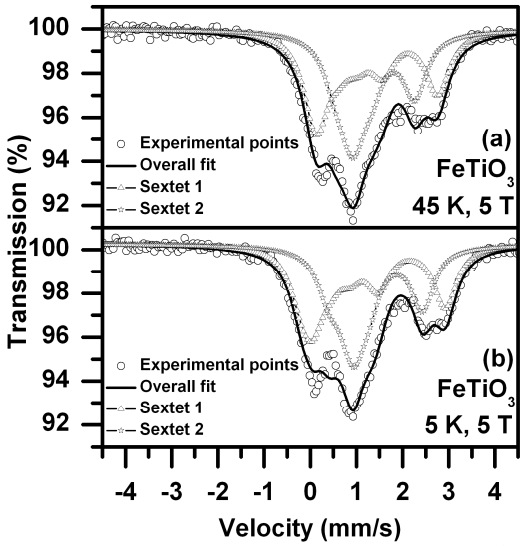

FIGURE 5. The Mössbauer spectrum of the powdered $FeTiO_3$ sample at 45 K and 5 T (a) and the Mössbauer spectrum at 5 K and 5 T (b) fitted by two sextets.

TABLE 4. Hyperfine parameters of $FeTiO_3$ at 5 K and 5 T and 45 K and 5 T, where T is the temperature of measurement, B_{ext} is the external magnetic filed, δ is the center shift, ΔE_Q is the quadrupole splitting, B_{eff} is the effective magnetic field (i.e., B_{eff} is vector sum of the external magnetic field B_{ext} and the hyperfine field B_{hf}), Γ is the linewidth and A is relative spectra area of each component.

Component	T (K)	B_{ext} (T)	$\delta \pm 0.01$ (mm/s)	$\Delta E_Q \pm 0.01$ (mm/s)	$B_{eff} \pm 0.3$ (T)	$\Gamma \pm 0.01$ (mm/s)	A (%)
Sextet 1	5	5	1.08	0.85	8.9	0.59	50
Sextet 2			1.27	0.85	4.6	0.59	50
Sextet 1	45	5	1.14	0.64	8.0	0.61	50
Sextet 2			1.28	0.64	4.2	0.61	50

Macroscopic Magnetic Behavior

In this section, we discuss the macroscopic magnetic behavior of $FeTiO_3$ powdered sample derived from the magnetization measurements. The temperature dependence of the molar susceptibility is shown in Fig. 6a. In this case, the molar susceptibility vs. temperature curve shows a maximum approximately at 57 K which corresponds to the magnetic transition temperature. A comparable Néel temperature T_N for $FeTiO_3$ is given in [25,26]. A low T_N of 57 K reflects not so strong antiferromagnetic interactions acting between Fe ions located on the different nearest layers which are separated by layers of Ti ions [27]. This conclusion of weak antiferromagnetic interactions is indirectly confirmed by the Curie-Weiss law that was found to be valid in the paramagnetic region above the characteristic Néel temperature. On the basis of this law, a value of the molar Curie constant C_{mol} was determined to be 5.8×10^{-5} K m^3/mol and a value of the paramagnetic Weiss temperature θ_p was found to be 30.6 K as derived from an extrapolation of the smooth curve through the experimental points of the reciprocal molar susceptibility above the magnetic transition temperature (see Fig. 6b). Despite the fact that $FeTiO_3$ is an ordered antiferromagnetic material, we observe a sing of θ_p to be positive. The positive value was also experimentally determined for $FeTiO_3$ in [25]. This suggests that the ferromagnetic interactions between Fe ions belonging to the same layer of $FeTiO_3$ structure dominate over the antiferromagnetic superexchange interactions of Fe ions between the alternate layers above T_N.

Further, as mentioned in the Introduction, $FeTiO_3$ is an antiferromagnetically ordered material but its temperature evolution of susceptibility does not confirm a typical behavior expected for an ideal antiferromagnetic powdered material below its Néel temperature (*i.e.*, it should fall down below T_N) because there is a change in the slope in the molar susceptibility at about 25 K. Similar behavior of susceptibility at low temperatures has been already observed for $FeTiO_3$ in [25]. These unusually increasing values of the susceptibility below 25 K are accompanied by the magnetic hardening as it is evidenced from the hysteresis loops recorded at 45 K and 1.9 K (see Fig. 7) and values of coercivity fields reported in Table 5. It is known that coercivity field and remanent magnetization should be almost constant and equal practically to zero for ideal antiferromagnetic material below T_N because the magnetizations on each magnetic sublattice are completely compensated together. Thus, the unusual magnetic behavior below 25 K and observed magnetic hardening validate the experimental conclusion that $FeTiO_3$ behaves as an imperfect antiferromagnetic material below its

characteristic ordering temperature as already predicted from the in-field Mössbauer spectra (see above).

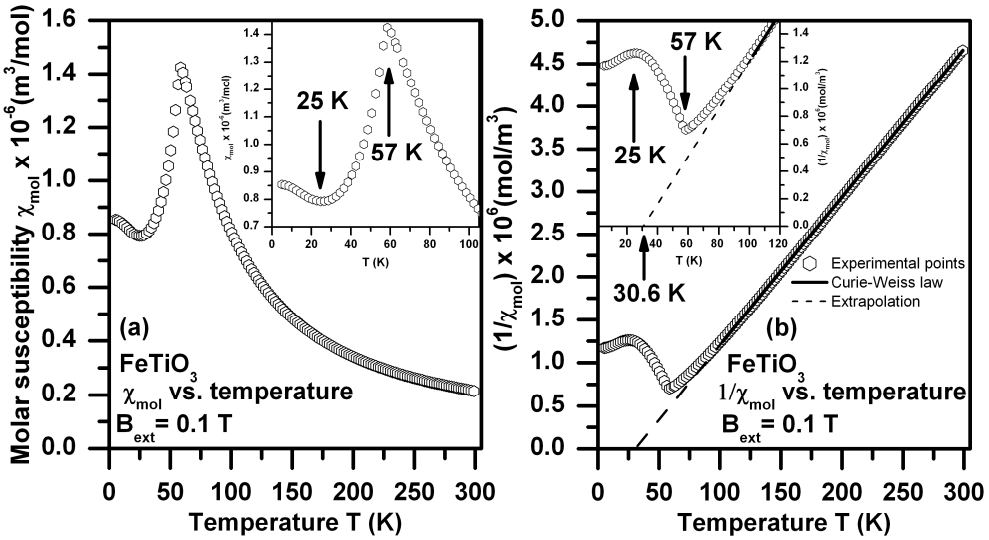

FIGURE 6. Temperature behavior of the molar susceptibility of the powdered $FeTiO_3$ sample (a) and temperature dependence of the reciprocal molar susceptibility of $FeTiO_3$ (b).

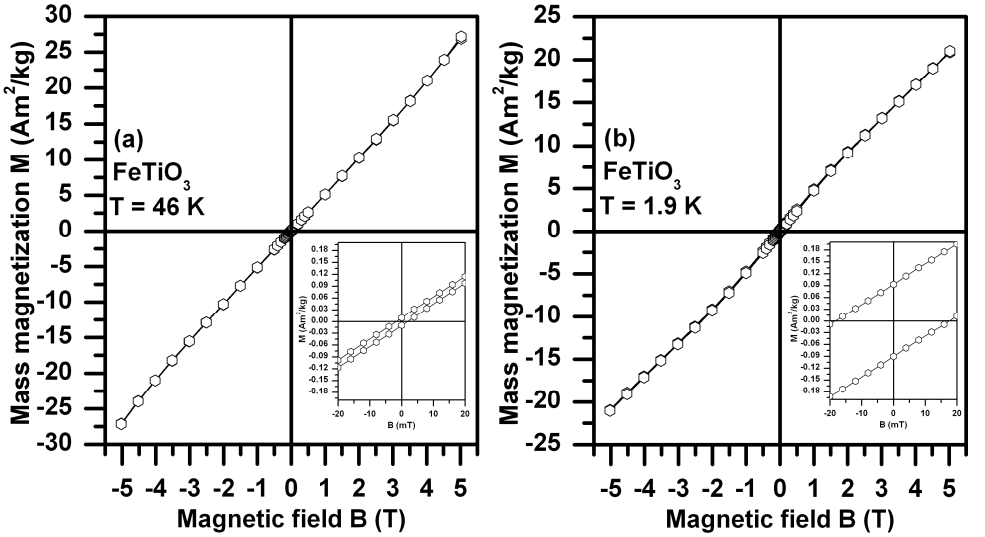

FIGURE 7. Hysteresis loops of the powdered $FeTiO_3$ sample at 46 K (a) and 1.9 K (b).

TABLE 5. Parameters of the hysteresis loops of the measured powdered $FeTiO_3$ at 1.9 K and 46 K, where M_{max+} is the maximum magnetization at + 5 T, M_{min-} is the maximum magnetization at – 5 T, B_{C+} is the "up-down" coercivity, B_{C-} is the "down-up" coercivity, M_{R+} is the "up-down" remanent magnetization and M_{R-} is the "down-up" remanent magnetization.

T (K)	M_{max+} (+ 5 T) (Am^2/kg)	M_{max-} (– 5 T) (Am^2/kg)	B_{C+} (T)	B_{C-} (T)	M_{R+} (Am^2/kg)	M_{R-} (Am^2/kg)
1.9	21.0525	– 21.0525	0.0177	– 0.0183	0.0936	– 0.0896
46	27.1348	– 27.1348	0.0018	– 0.0018	0.0094	– 0.0094

CONCLUSIONS

In the present study, we examined the magnetic behavior of powdered $FeTiO_3$ sample from the viewpoint of zero-field and in-field ^{57}Fe Mössbauer spectroscopy and magnetization measurements. Following conclusions can be drawn from the reported results:

(1) From the temperature evolution of the zero-field Mössbauer spectra of the powdered $FeTiO_3$ sample and on the basis of expected behavior of the high-temperature recoil-free fraction, we found the value of effective vibrating mass to be equal to (78 ± 3) amu and the Debye temperature equal to (359 ± 27) K;

(2) The in-field low-temperature Mössbauer spectra indicate that below 57 K, $FeTiO_3$ behaves as a non-ideal antiferromagnetic material;

(3) From the magnetization measurements carried out on the powdered $FeTiO_3$ sample, we determined the Curie constant and Weiss temperature to be equal to 5.8 $\times 10^{-5}$ Km^3/mol and 30.6 K, respectively;

(4) Below 25 K, we observed a significant magnetic hardening of $FeTiO_3$ as documented by a remarkable enhancement in the material's coercivity at low temperatures.

ACKNOWLEDGEMENTS

This work has been supported by the Projects of the Ministry of Education of the Czech Republic (1M6198959201, MSM6198959218 and MSM6198959214), the Project of the Academy of Sciences of the Czech Republic (KAN115600801) and by the Project of Grant Agency of the Czech Republic (Project No. 106/08/1440).

REFERENCES

1. G. Kletetchka, P. J. Wasilewski and P. T. Taylor, *Tectonophysics* **347**, 167-177 (2002).
2. S. A. McEnroe, B. Carter-Stiglitz, R. J. Harrison, P. Robinson, K. Fabian and C. McCammon, *Nat. Nanotechnol.* **2**, 631-634 (2007).
3. N. C. Wilson, J. Muscat, D. Mkhonto, P. E. Ngoepe and N. M. Harrison, *Phys. Rev. B* **71**, 075202 (2005).
4. X. Wu, G. Steinle-Neumann, O. Narygina, I. Kantor, C. McCammon, S. Pascarelli, G. Aquilanti, V. Prakapenka and L. Dubrovinsky, *Phys. Rev. B* **79**, 094106 (2009).
5. G. Shirane, S. J. Pickart, R. Nathans and Y. Ishikawa, *J. Phys. Chem. Solids* **10**, 35-43 (1959).
6. H. Kato, Y. Yamaguchi, M. Ohashi, M. Yamada, H. Takei and S. Funahashi, *Solid State Commun.* **45**, 669-672 (1983).

7. H. Kato, Y. Yamaguchi, M. Yamada, S. Funahashi, Y. Nakagawa and H. Takei, *J. Phys. C: Solid State Phys.* **19**, 6993-7011 (1986).
8. Y. Yamaguchi, H. Kato and H. Takei, *Solid State Commun.* **59**, 865-868 (1986).
9. H. Kato, M. Yamada, H. Yamauchi, H. Hiroyoshi, H. Takei and H. Watanabe, *J. Phys. Soc. Jpn.* **51**, 1769-1777 (1982).
10. H. Kato and Y. Nakagawa, *Physica B* **201**, 80-83 (1994).
11. G. Radtke, S. Lazar and G. A. Botton, *Phys. Rev. B* **74**, 155117 (2006).
12. R. W. Vaughan and H. G. Drickamer, *J. Chem. Phys.* **47**, 1530-1536 (1967).
13. P. A. van Aken, B. Liebscher and V. J. Styrsa, *Phys. Chem. Miner.* **25**, 323-327 (1998).
14. T. Seda and G. R. Hearne, *J. Phys. Condens. Matter* **16**, 2707-2718 (2004).
15. T. Fujii, M. Yamashita, S. Fujimori, Y. Saitoh, T. Nakamura, K. Kobayashi and J. Takada, *J. Magn. Magn. Mater.* **310**, e555-e557 (2007).
16. Z. Homonnay, S. Music, T. Nishida, N. S. Kopelev and A. Vértes, *Mössbauer Spectroscopy of Sophisticated Oxides*, edited by A. Vertes and Z. Homonnay, Akademiai Kiado Budapest 1997, pp. 1-26.
17. Y.-L. Chen and D.-P. Yang, *Mössbauer Effect in Lattice Dynamics: Experimental Techniques and Applications*, Weinheim: WILEY-VCH Verlag GmbH & Co. KGaA, Germany, 2007, pp. 29-211.
18. N. N. Greenwood and T. C. Gibb, *Mössbauer Spectroscopy*, Chapman & Hall Ltd., London, UK, 1971, pp. 46-79.
19. W. Kin, I. J. Park and C. S. Kim, *J. Korean Phys. Soc.* **53**, 1529-1533 (2008).
20. P. B. Fabritchnyi, M. V. Korolenko, M. I. Afanasov, M. Danot and E. Janod, *Solid State Commun.* **125**, 341-346 (2003).
21. R. W. Grant, R. M. Housley and S. Geller, *Phys. Rev. B* **5**, 1700-1703 (1972).
22. W. Kündig, *Nucl. Instrum. Meth.* **48**, 219-228 (1967).
23. R. W. Grant, Mössbauer Spectroscopy in Magnetism: Characterization of Magnetically-Ordered Compounds, in Mössbauer Spectroscopy, edited by U. Gonser, Springer-Verlag Berlin, Germany, 1975, pp. 97-137.
24. J. Chappert, *J. Phys. Colloque* **35**, C6-71 (1974).
25. J. J. Stickler, S. Kern, A. Wold and G. S. Heller, *Phys. Rev.* **164**, 765-767 (1967).
26. P. F. McDonald, A. Parasiris, R. K. Pandey, B. L. Gries and W. P. Kirk, *J. Appl. Phys.* **69**, 1104-1106 (1991).
27. N. E. Brown, A. Navrotsky, G. L. Nord and S. K. Banerjee, *Am. Mineral.* **78**, 941-951 (1993).

Příloha B

Čuda, J., Kohout, T., Tuček, J., Haloda, J., Filip, J., Prucek, R., Zbořil, R.:

Low-temperature magnetic transition in troilite: A simple marker for highly stoichiometric FeS systems

J. Geophys. Res., 116, B11205 (2011)

JOURNAL OF GEOPHYSICAL RESEARCH, VOL. 116, B11205, doi:10.1029/2011JB008232, 2011

Low-temperature magnetic transition in troilite: A simple marker for highly stoichiometric FeS systems

J. Cuda,[1] T. Kohout,[2,3] J. Tucek,[1] J. Haloda,[4] J. Filip,[1] R. Prucek,[1] and R. Zboril[1]

Received 24 January 2011; revised 29 August 2011; accepted 30 August 2011; published 15 November 2011.

[1] Low-temperature magnetic evolution of troilite sample, extracted from the Cape York IIIA octahedrite meteorite, was investigated by employing macroscopic magnetic measurement, Mössbauer spectroscopy, scanning electron microscopy (SEM) and backscattered electrons (BSE) microscopy, X-ray diffraction (XRD), electron microprobe analysis (EMA), and atomic absorption spectrometry (AAS). The study identified a magnetic transition at ≈70 K manifested itself in a similar manner as previously reported for troilite from the Bruderheim L6 chondrite meteorite. The data show that this transition is unlikely driven by impurity such as chromite and seems to be rather an intrinsic property of troilite. In this study, we unambiguously exclude the relation of this transition to the structural rearrangement like the Morin transition in hematite. Similarly, in-field Mössbauer data do not support the change of the canting angle in the spin structure of FeS above and below the transition. Mössbauer, XRD, and magnetic data, newly measured also for troilite from the Bruderheim L6 chondrite, demonstrate that both studied troilite samples exhibit nearly the same magnetic and structural characteristics. Thus, the nature of the transition occurring at ≈70 K in both samples has identical characteristics and its detection can be used as a simple general marker for highly stoichiometric FeS systems.

Citation: Cuda, J., T. Kohout, J. Tucek, J. Haloda, J. Filip, R. Prucek, and R. Zboril (2011), Low-temperature magnetic transition in troilite: A simple marker for highly stoichiometric FeS systems, *J. Geophys. Res.*, *116*, B11205, doi:10.1029/2011JB008232.

1. Introduction

[2] Sulphides, including iron bearing ones as pyrhottite group $Fe_{1-x}S$ (such as troilite FeS stoichiometric end-member), daubreelite (i.e., $FeCr_2S_4$), alabandite (i.e., (Fe, Mn)S), or pentlandite (i.e., (Fe, Ni)S) are major components in most of extraterrestrial materials. Some of them undergo magnetic transitions at low temperatures making them, together with metallic FeNi, an important magnetic phase [*Kohout et al.*, 2010]. In this work, we present new data on the low temperature magnetic properties, zero-field and in-field Mössbauer study of troilite below and above a magnetic transition taking place at ≈70 K, first reported by *Kohout et al.* [2007].

[3] Troilite (FeS) is the end-member of the pyrrhotite group with a stoichiometric or near stoichiometric iron and sulfur content with the range of 50.00–48.72 atomic percent of iron with hexagonal 2C superstructure of an NiAs type [*Hägg and Sucksdorff*, 1933] below the crystallographic α-transition at ≈413 K. At this temperature, iron sulfide transforms from high-temperature NiAs-type structure ($P6_3mmc$ symmetry) to the troilite structure ($P\bar{6}2c$). Magnetic properties of troilite have been extensively studied by a number of authors above room temperature [*Haraldsen*, 1937, 1941; *Hirahara and Murakami*, 1958; *Murakami and Hirahara*, 1958; *Murakami*, 1959; *Schwarz and Vaughan*, 1972; *Gosselin et al.*, 1976; *Horwood et al.*, 1976; *Li and Franzen*, 1996]. The superexchange interaction between iron atoms in the adjacent layers mediated by the non-magnetic sulfur atoms gives rise to an antiferromagnetic behavior below the Néel temperature T_N of ≈588 K [*Wang and Salveson*, 2005] with spins perpendicular to the *c*-axis of the NiAs subcell. Moreover, the spin-flip transition is observed at ≈445 K where spins rotate to a direction parallel to the *c*-axis.

[4] The low temperature magnetic study by *Kohout et al.* [2007], performed on a powdered fraction extracted from the Bruderheim L6 chondrite, revealed an existence of the magnetic transition at ≈70 K in troilite. However, the nature of this transition has not been addressed in details. Thus, there is a need to search for this transition in other troilite samples in order to explain its nature and to distinguish whether it is a special feature related to the Bruderheim troilite only, or whether it is a general phenomenon characteristic to highly stoichiometric FeS systems.

[5] In this study, we investigate the nature of this low-temperature magnetic behavior on troilite sample extracted from the Cape York IIIAB meteorite. Additionally, we re-investigated troilite from the Bruderheim L6 chondrite with experimental techniques not used in the previous

[1]Regional Centre of Advanced Technologies and Materials, Departments of Physical Chemistry and Experimental Physics, Palacky University, Olomouc, Czech Republic.
[2]Department of Physics, University of Helsinki, Helsinki, Finland.
[3]Institute of Geology, Academy of Sciences of the Czech Republic v.v i., Prague, Czech Republic.
[4]Czech Geological Survey, Prague, Czech Republic.

0148-0227/11/2011JB008232

study by *Kohout et al.* [2007] (new data acquired on the Bruderheim troilite are presented in the auxiliary material).[1]

[6] *Gattacceca et al.* [2011] recently presented low temperature magnetic investigations of chromite in various ordinary chondrites and points out that the Curie temperature of certain chromite compositions may be close to the transition temperature observed in troilite. As chromite, below its Curie temperature, carries a significantly stronger magnetic moment than troilite in the same temperature range, there is a chemical and structural requirement to verify a possible magnetic role of chromite as an inclusion in the studied troilite samples.

2. Experiment

[7] The FeS_Cape_York troilite sample is a polycrystalline troilite extract from the Cape York IIIAB iron octahedrite meteorite. The Cape York meteorite is an ancient find from Greenland with around 60 t reported in today's collections. Our troilite extract was kindly provided by Dr. Roman Skála from the Institute of Geology, Academy of Sciences of the Czech Republic.

[8] The FeS_Bruderheim troilite sample, identical with the sample used in earlier studies [*Kohout et al.*, 2007, 2010], is a powdered troilite extract from a Bruderheim L6 chondrite. The Bruderheim meteorite fall occurred in Alberta, Canada, on March 4, 1960, and subsequently over 300 kg of the meteorite were recovered. Our troilite extract was kindly provided by Peter Wasilewski from the NASA Goddard Space Flight Center.

[9] Natural chromite from the Bulguzi locality, Albania (the sample was taken from the mineralogical collection of the Moravian Museum in Brno, Czech Republic; Sample No. A3159/1962), was used for illustrating the limits of quantitative phase analysis calculated from the XRD data.

[10] In order to validate the troilite crystal structure, stoichiometry, and content of impurities, an X-ray powder diffraction (XRD), electron microprobe analysis (EMA), and atomic absorption spectrometry (AAS) were used. X-ray diffraction patterns of powdered samples were recorded at room temperature on a PANalytical X'Pert PRO (The Netherlands) instrument in the Bragg-Brentano geometry with an Fe-filtered CoK_α radiation (40 kV, 30 mA). Samples were placed on a zero-background and rotating single-crystal Si slides, gently pressed in order to obtain sample thickness of about 0.5 mm and scanned in the 2θ range of 10–90° in steps of 0.017°. The acquired patterns were evaluated using the X'Pert HighScore Plus software (PANalytical), PDF-4+ and ICSD databases.

[11] EMA was carried out using a MICROSPEC 3PC Wavelength dispersive X-ray spectroscopy (WDS) system on a CamScan 3200 scanning electron microscope (SEM) at the Czech Geological Survey. The same SEM was used also in backscattered electrons (BSE) mode. The analyses were performed on a polished flat surface of troilite grains using an accelerating voltage of 20 kV, 22 nA beam current, 1 μm beam size and ZAF correction procedures. The analyzed chemical elements included Fe, S, P, Ti, Cr, Mn, Ni, and Co. Well characterized pyrite, GaP, tephroite, rutile, and pure elements were used as standards. In any cases, all data reported are averages from 33 (Bruderheim) and 31 (Cape York) single point analyses.

[12] Scanning electron microscope (i.e., SEM) images of whole grains were obtained on a Hitachi SU-6600 (FEG, SE image resolution of 1.2 nm at 30 kV). The micrographs were collected with an acceleration voltage of 10.0 kV at a working distance of 5.00 mm. Sample material was fixed on carbon conductive discs. No coating method was used.

[13] A Quantum Design MPMS XL-7 superconducting quantum interference device (SQUID) has been used for the macroscopic magnetic measurements. The temperature dependence of the magnetization was recorded in the sweep mode employing following measurement procedures: (1) induced magnetization (induced-FC) measurements, (2) field-cooled measurements of remanence (rem-FC), (3) zero-field-cooled measurements of remanence (rem-ZFC), and (4) room temperature saturation isothermal magnetization cycle (RT SIRM cycle). The details on the measurements are provided in the auxiliary material. Hysteresis loops were recorded at various temperatures in external magnetic fields ranging from −7 to +7 T.

[14] For Mössbauer measurements at various temperatures, we used Mössbauer spectrometer with a ^{57}Co(Rh) source of γ-rays and the values of the derived hyperfine Mössbauer parameters are referred to the metallic iron (α-Fe) at room temperature. Furthermore, in the case of in-field Mössbauer measurements, a parallel geometry has been employed when incoming γ-rays propagate along the direction of an external magnetic field of 5 T. Zero- and in-field Mössbauer spectra were fitted by means of the Lorentzian line shapes using the least squares method featured in the MossWinn computer program.

[15] Upon completion of all magnetic measurements, the troilite samples were tested for bulk chromium and iron content of troilite using AAS. The samples (≈15 mg each) were dissolved in 1 ml of 36% HCl and consequently diluted by deionized water to a volume equal to 20 ml in the volumetric flasks. These solutions were 100 times diluted for determination of iron content; for determination of Cr content, the prepared 20 ml solutions were analyzed without any dilution. Bulk chromium and iron concentrations were determined by the AAS technique with flame ionization using a ContrAA 300 (Analytik Jena AG, Germany) equipped with a high-resolution Echelle double monochromator (spectral bandwidth of 2 pm at 200 nm) and with a continuum radiation source (xenon lamp). The absorption lines used for these analyses were 248.3270 nm for iron and 357.8687 nm for chromium. The calibration standards were prepared using an Iron Standard for AAS (1001 mg/L, Fluka) and using K_2CrO_4 (Sigma-Aldrich, ≥99.5%).

3. Results and Discussion

3.1. SEM, XRD, and Chemical Composition of the FeS_Cape_York Troilite Sample

[16] The SEM image of the powdered FeS_Cape_York sample is depicted in Figure 1a whereas Figure 1b shows details of surface of single fragment of particular sample randomly selected from those depicted in Figure 1a. The detailed investigation performed at a higher resolution revealed a presence of ultrafine particles in the FeS_Cape_York sample

[1] Auxiliary materials are available in the HTML. doi:10.1029/2011JB008232.

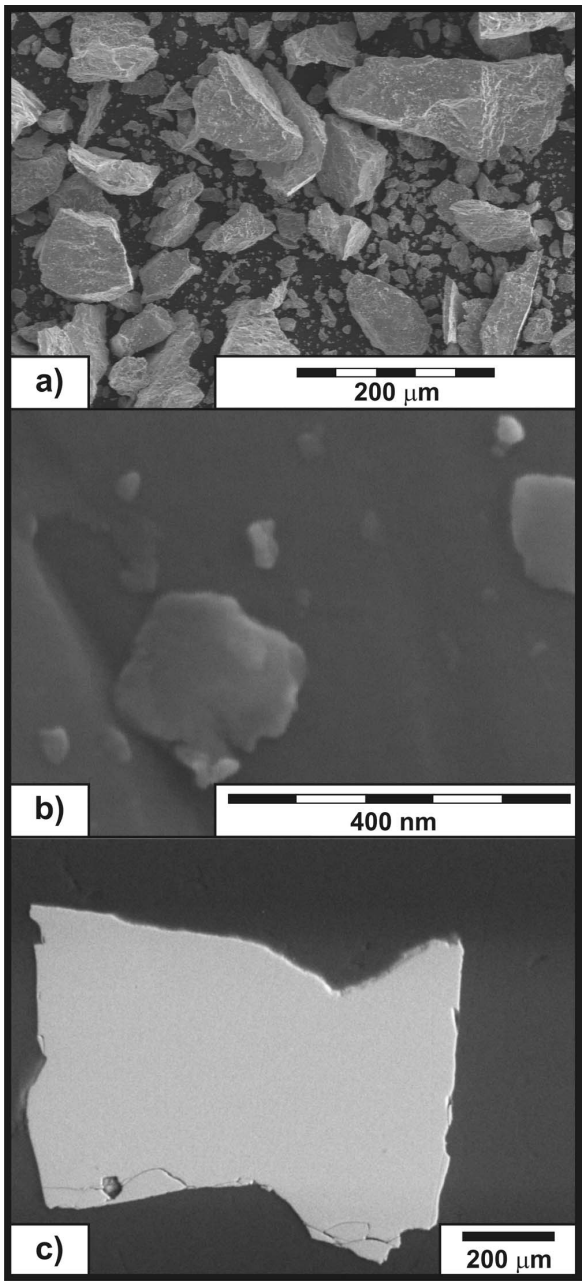

Figure 1. SEM images of (a) the powdered FeS_Cape_York sample and (b) nanosized particles on the grain surface of the powdered FeS_Cape_York sample; (c) BSE image of polished fragment of the FeS_Cape_York sample.

(originating from grind/crush process of meteorite sample) randomly distributed on the surface of larger particles and with diameters ranging from 15 to 280 nm.

[17] The XRD pattern of the investigated powdered sample, acquired at room temperature, is shown in Figure 2. It perfectly correlates with the marked troilite structure (PDF No. 01-080-1026) without any indication of the presence of other phases. The Rietveld refinement was used exclusively to evaluate the cell parameters of the FeS_Cape_York sample. They were found to be a = 5.966(5) Å and c = 11.757(7) Å. The obtained values of the cell parameters are in good agreement with those previously reported for the troilite structure [*Keller-Besrest and Collin*, 1990; *Skála et al.*, 2006].

[18] The composition of the FeS_Cape_York sample was estimated according to a d(102) method described by *Arnold* [1962] and *Arnold and Reichen* [1962] indicating approximately 50 atomic percent of iron; however, more precise results were obtained by means of EMA from which the iron-to-sulfide ratios can be expressed by the chemical formula given by $Fe_{0.994}S$ (see Table S1 in the auxiliary material). The findings presented above demonstrate that the FeS_Cape_York sample is a very near stoichiometric iron sulfide and can be considered as a representative of highly stoichiometric troilite with only minor presence of other elements (see Table S1 in the auxiliary material).

3.2. Macroscopic Magnetic Properties of the FeS_Cape_York Sample

[19] The induced-FC magnetization curves in external magnetic fields up to 1 T, 2.5 T rem-ZFC, rem-FC and RT SIRM cycle thermomagnetic data as well as the determination of transition temperature acquired for the FeS_Cape_York sample are shown in Figure 3. All the low-temperature evolutions of magnetic response show an increase in magnetization values at ≈70 K on cooling and the temperature of the transition is independent on the value of external magnetic fields up to 1 T as observed on induced–FC curves (see Figure 3a).

[20] The hysteresis loops around the origin exhibit a different profile as the troilite system passes through the transition (see Figures 4a, 5a corrected the paramagnetic slope at

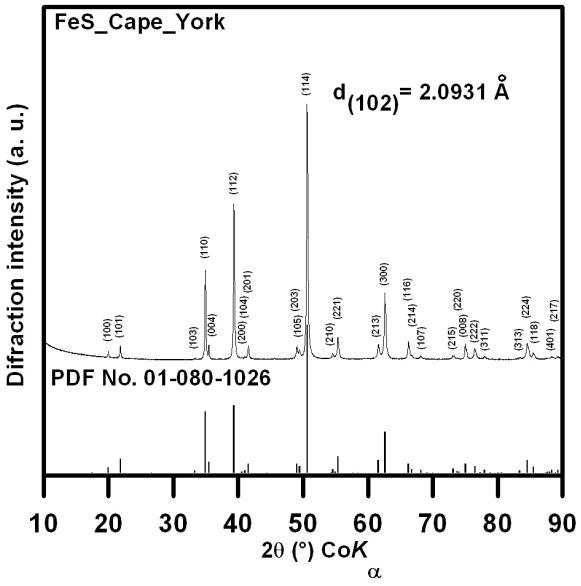

Figure 2. XRD pattern of the FeS_Cape_York sample, acquired at room temperature.

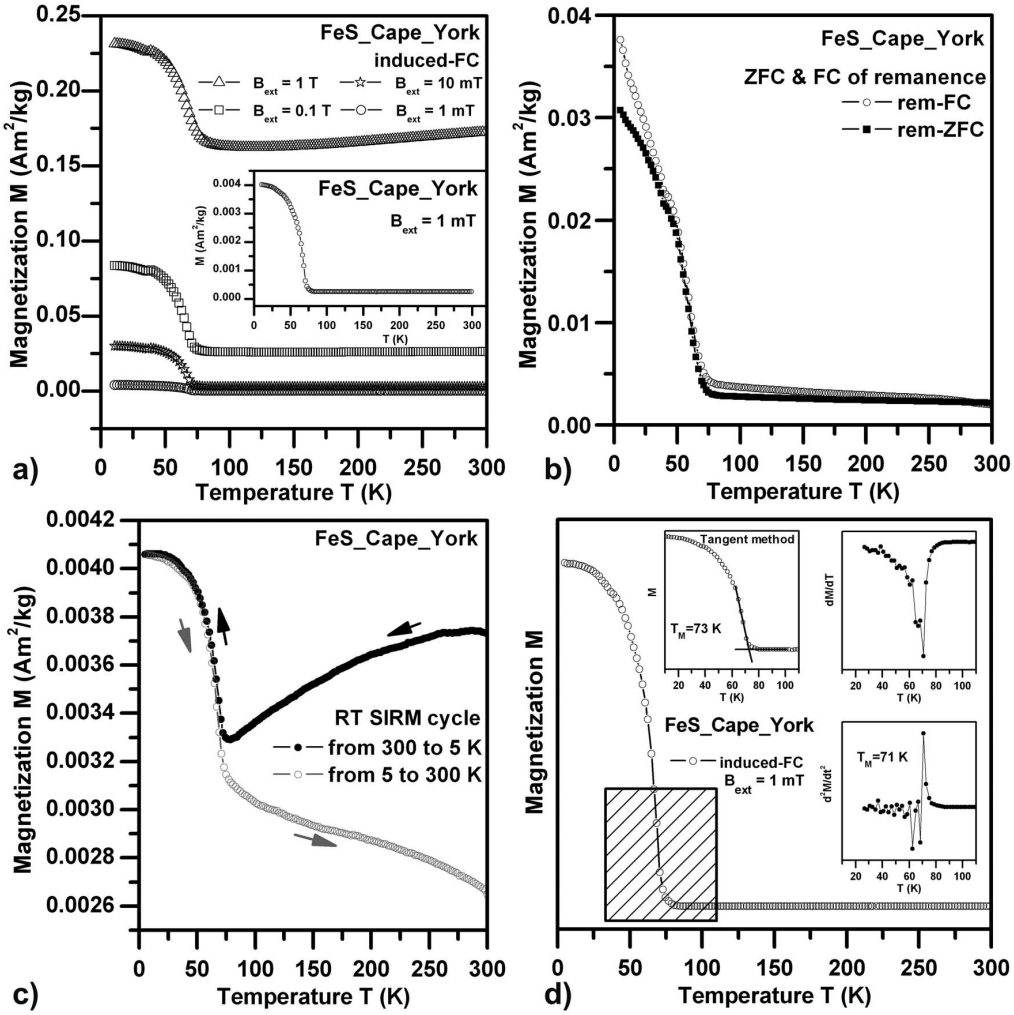

Figure 3. (a) Induced-FC magnetization curves in external magnetic fields up to 1 T recorded for the FeS_Cape_York sample, (b) ZFC-FC curves of remanent magnetization imprinted by a field of 2.5 T, (c) RT SIRM cycle imprinted by a field of 2.5 T, and (d) estimation of magnetic transition temperature for the FeS_Cape_York, T_M, on the induced-FC magnetization curve (1 mT) by means of the tangent method and maximum of curvature.

10 K, Table 1, and Figure S1 in Text S2 in the auxiliary material for details). Above 70 K, the shape of the hysteresis loops is very close to that reported for antiferromagnetic materials and indicates that the direction of the atomic magnetic moment is not easily affected by an external magnetic field. On the other hand, as the temperature falls below 70 K, the hysteresis loops around the origin have an S-shape with an increase in the area of the hysteresis loop and a tendency to saturation. These properties are typical for ferromagnetic, ferrimagnetic, and/or canted antiferromagnetic arrangements of magnetic moments.

[21] Macroscopic magnetic response at ≈70 K can be easily interpreted if we consider a dramatic increase in the magnetization curves (see Figure 3) being consistent with the change in the profile of the hysteresis loop around origin. Then, the magnetic data indicate a thermodynamic-like transition from a high-temperature antiferromagnetic regime to a low-temperature ordered state of ferromagnetic, ferrimagnetic, and/or canted antiferromagnetic nature.

3.3. Zero-Field Mössbauer Spectroscopy of the FeS_Cape_York Sample

[22] The zero-field Mössbauer spectra above and below ≈70 K (see Figure 6a) are symmetrical with respect to the center of spectrum and show only one sextet component. This indicates a magnetically ordered state and a presence of only one type of Fe position in the FeS troilite structure.

[23] In order to confirm or exclude the Morin-type spin reorientation phenomenon in the FeS troilite at ≈70 K as suggested by *Kohout et al.* [2007], we monitored a temperature

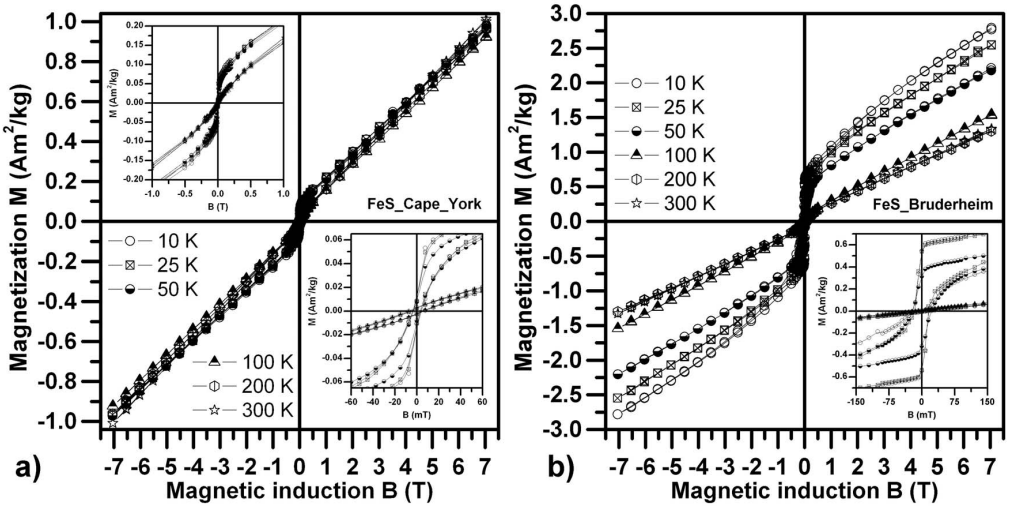

Figure 4. Representative hysteresis loops at 10, 25, 50, 100, 200, and 300 K, summarized for comparison: (a) the FeS_Cape_York sample and (b) the FeS_Bruderheim sample.

evolution of the zero-field quadruple splitting parameter (ΔE_Q) when passing through ≈70 K (see Table 2). If the Morin-like transition takes place, changes in the ΔE_Q-value would be observed due to the spin reorientation. For example, the quadruple splitting abruptly converts from +0.37 mm/s to −0.19 mm/s as a result of transformation from an antiferromagnetic state to weakly ferromagnetic one during heating through the Morin transition (≈265 K) in hematite [*Vandenberghe et al.*, 1990; *Zboril et al.*, 2002]. However, we do not observe any significant change of ΔE_Q above and below ≈70 K in our case. Thus, the low-temperature magnetic phenomenon at ≈70 K (see Figure 3) is not a structurally driven transition in comparison to the Morin transition in hematite at ≈265 K.

3.4. In-Field Mössbauer Spectroscopy of the FeS_Cape_York Sample

[24] To our best knowledge, the low-temperature Mössbauer spectra of the FeS_Cape_York troilite sample (see Figure 6b and Table 2) or generally of any FeS system in external magnetic fields have not been reported yet.

[25] As one can see, two sextets have been used in order to correctly fit the experimental spectral profile above and below ≈70 K. The need of two sextets to fit the Mössbauer spectra is rather surprising because only one Fe crystallographic position surrounded by sulfur atoms is expected for the FeS systems. This observation may indicate that the application of the external magnetic field causes the separation of two magnetic sublattices in the FeS structure.

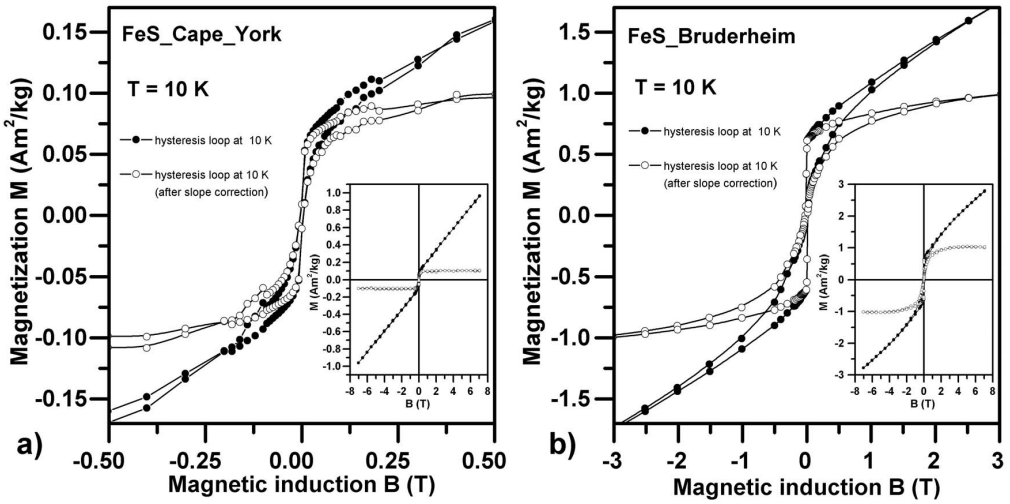

Figure 5. Hysteresis loop at 10 K and the same hysteresis loop after the paramagnetic slope correction: (a) the FeS_Cape_York sample and (b) the FeS_Bruderheim sample.

Table 1. Parameters of the Hysteresis Loops of the FeS_Cape_York and the FeS_Bruderheim Sample at 10 K After the Paramagnetic Slope Has Been Subtracted[a]

Sample	T (K)	M_{S+} (+7 T) ±0.001 (Am^2/kg)	M_{S-} (−7 T) ±0.001 (Am^2/kg)	B_{C+} ± 0.1 (mT)	B_{C-} ± 0.1 (mT)	M_{R+} ± 0.001 (Am^2/kg)	M_{R-} ± 0.001 (Am^2/kg)
FeS_Cape_York	10	0.107	−0.101	1.2	−2.4	0.009	−0.011
FeS_Bruderheim	10	1.022	−1.013	14.6	−22.4	0.545	−0.545

[a]M_{S+} (+7 T) is the saturation magnetization at +7 T, M_{S-} (−7 T) is the saturation magnetization at +7 T, B_{C+} is the positive coercivity, B_{C-} is the negative coercivity, M_{R+} is the positive remanent magnetization, and M_{R-} is the negative remanent magnetization.

Similar interpretation was suggested by *Cuda et al.* [2010] for non-ideal antiferromagnetic behavior of synthetic ilmenite which magnetically hardens and shows anomalous magnetic behavior at low temperatures. Then, the spectral area under the two sextets has to be in the ratio of 1:1 because 50% of Fe atomic magnetic moments belong to each magnetic sublattice. However, the hypothesis of different effect of external magnetic field on the two magnetic sublattices cannot be confirmed or ruled out in FeS systems. Thus, we do not make any other conclusion using this interpretation on the basis of different external magnetic field influences.

[26] Furthermore, during the fitting procedure, the relative line intensities of both sextets were set to 3:x:1:1:x:3 in order to identify an eventual increase and/or decrease in the intensities of the second and fifth lines in the in-field Mössbauer spectra below and above ≈70 K. There is no change detected in the intensities of the second and fifth of individual sextets implying that the spin structures under the external magnetic field remain the same above and below the magnetic transition at ≈70 K.

3.5. Low-Temperature Magnetization Data and Zero-Field and In-Field Mössbauer Spectra of the FeS_Bruderheim Sample

[27] The troilite extract from the Bruderheim L6 chondrite (FeS_Bruderheim sample), which is identical with the sample used in the earlier study [*Kohout et al.*, 2007] and exhibits the same change in the temperature dependence of magnetization at ≈70 K, has been re-investigated employing new low-temperature magnetization measurements (especially hysteresis loops) and zero-field and in-field Mössbauer spectroscopy. Moreover, characterization of the particle size, crystal structure, and chemical composition have been performed in order to supplement the early study [*Kohout et al.*, 2007].

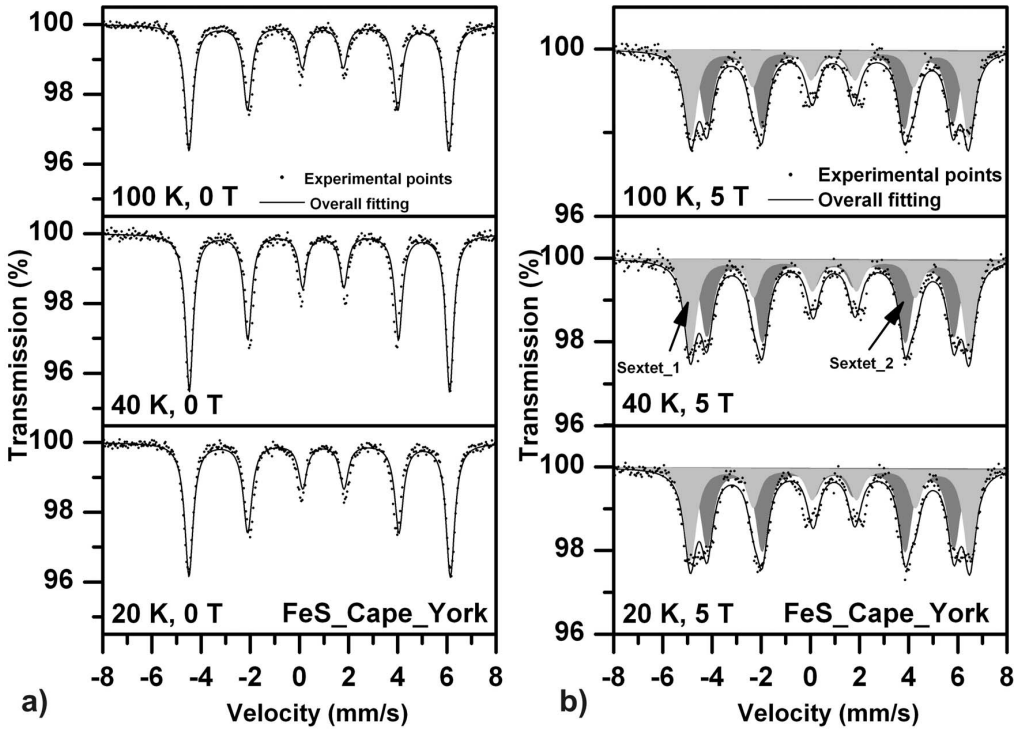

Figure 6. (a) Zero-field Mössbauer spectra of the FeS_Cape_York sample recorded below and above transition of ≈70 K and (b) in-filed Mössbauer spectra recorded below and above the transition at ≈70 K in the external magnetic field of 5 T for the FeS_Cape_York sample.

Table 2. Hyperfine Parameters of Zero-Field and In-Field Mössbauer Spectra of the FeS_Cape_York Sample at Various Temperatures[a]

Sample	B_{ext} (T)	T (K)	Sextet	$\delta \pm 0.02$ (mm/s)	$\Delta E_Q \pm 0.02$ (mm/s)	$B_{hf} \pm 0.3$ (T)	$B_{eff} \pm 0.3$ (T)	$\Gamma \pm 0.02$ (mm/s)	RA ± 3%
FeS_Cape_York	0	20		0.90	−0.15	33.0	—	0.42	100
	0	40		0.89	−0.15	32.9	—	0.38	100
	0	100		0.87	−0.15	32.9	—	0.41	100
	5	20	Sextet_1	0.89	−0.18	—	35.4	0.59	47
			Sextet_2	0.88	−0.13	—	31.2	0.59	53
	5	40	Sextet_1	0.89	−0.19	—	35.3	0.59	47
			Sextet_2	0.88	−0.15	—	31.2	0.59	53
	5	100	Sextet_1	0.86	−0.14	—	35.1	0.59	47
			Sextet_2	0.86	−0.13	—	31.1	0.59	53

[a] B_{ext} is external magnetic field, T is the temperature of the measurement, δ is the isomer shift, ΔE_Q is the quadrupole splitting, B_{hf} is the magnetic hyperfine field, B_{eff} is the effective field (i.e., the vector sum of hyperfine field and external magnetic field), Γ is the linewidth and RA the relative area of individual sextets.

[28] The acquired data correspond well with those derived for the FeS_Cape_York sample confirming their similarity. This makes possible to generalize our study for troilite systems. Here we summarize briefly acquired data for the FeS_Bruderheim sample:

[29] 1. The sizes of large and ultrafine particles are close to the particle sizes present in the FeS_Cape_York sample (see Figures S2a and S2b in Text S2 in the auxiliary material).

[30] 2. The Rietveld refinement of the XRD pattern gives lattice parameters a = 5.966(2) Å and c = 11.749(7) Å, and no traces of other phases were detected (see Figure S3a in Text S2 in the auxiliary material).

[31] 3. The FeS_Bruderheim sample is (similarly to the FeS_Cape_York sample) nearly stoichiometric FeS with the chemical formula of $Fe_{0.988}S$ with only minor presence of other elements as documented by EMA (see Table S1 in the auxiliary material).

[32] 4. The strength of the applied magnetic fields (up to 1 T) does not affect the temperature at which a rapid increase in the induced-FC magnetization curve occurs (see Figure S3b in Text S2 in the auxiliary material).

[33] 5. We observe a change in the hysteresis loop profile around the origin when passing through 70 K (see Figure 4b and Figure S4 in Text S2 in the auxiliary material for details).

[34] 6. The zero-field and in-field Mössbauer spectra of the FeS_Bruderheim sample displays the same characteristics as found for the FeS_Cape_York sample (see Figure S5 in Text S2 and Table S2 in the auxiliary material).

[35] 7. The magnetic response of the FeS_Bruderheim sample is roughly 10 times higher in comparison to the FeS_Cape_York sample in almost all measurements. This enhancement of magnetization can be caused by several aspects the influence of which is very difficult to determine. At this point, we can exclude impurity presence and particle-size effects because both samples have similar particle size as it is evident from the SEM images (see Figures 1a and 1b for the FeS_Cape_York and Figures S2a and S2b in Text S2 in the auxiliary material for the FeS_Bruderheim sample).

[36] To estimate the magnetic transition temperature more precisely, we have employed a method based on finding the temperature at which the thermomagnetic curve exhibits the maximum curvature around 70 K (Figure 3d for the FeS_Cape_York and Figure S6 in Text S2 in the auxiliary material for the FeS_Bruderheim sample). According to this procedure, we get a magnetic transition temperature of 71 K and 67 K for the FeS_Cape_York and FeS_Bruderheim sample, respectively. These temperature estimates are more precise compared to those previously reported by *Kohout et al.* [2007, 2010].

3.6. Test for Presence of Chromite Impurity in Our Troilite Samples

[37] As discussed above, *Gattacceca et al.* [2011] proposed an alternative interpretation of the observed magnetic transition in the troilite and attributes this solely to the Curie point of possible chromite impurity in our troilite samples. Based on the data published by *Kohout et al.* [2007] for the troilite from the Bruderheim meteorite (FeS_Bruderheim), *Gattacceca et al.* [2011] calculate the required chromite contamination in the FeS_Bruderheim sample to be around 4 wt%. If we take into account a value of saturation magnetization for pure chromite (16 Am^2/kg) [*Gattacceca et al.*, 2011] and for the FeS_Bruderheim sample (1 Am^2/kg derived from measured the hysteresis loop at 10 K, see Figure 5b and Table 1), we obtain a higher value of the required chromite contamination equal to 6.25 wt% in the FeS_Bruderheim extract.

[38] Similarly, due to approximately 10 times lower magnetic response of the FeS_Cape_York sample, a chromite content of 0.63 wt% would be needed in the sample to explain the saturation magnetization of 0.1 Am^2/kg at 10 K (see Figure 5a and Table 1).

[39] In order to test this hypothesis, we reviewed our magnetic data concerning both our FeS_Bruderheim and FeS_Cape_York troilite samples for such chromite contamination through following detailed mineralogical, chemical, and structural analysis:

[40] 1. To visually and compositionally check the purity of our investigated troilite samples, we employed a scanning electron microscopy over the polished samples in the BSE mode being sensitive for compositional variations. The acquired BSE images (see Figure 1c for FeS_Cape_York and Figure S2c in Text S2 in the auxiliary material for FeS_Bruderheim) do not show any inclusions in our troilite samples down to a micron scale.

[41] 2. To further exclude a significant presence of impurities such as chromite even on a submicron scale, the troilite samples were subjected to the AAS elemental analysis. The AAS analysis was performed on the identical samples on which all above presented magnetic data were collected using a Quantum Design MPMS XL-7 magnetometer. The AAS analysis revealed a very low content of chromite (see

Table S1 in the auxiliary material). If the FeS_Bruderheim sample contains 4–6 wt% of chromite required to reproduce the magnetic changes at ≈70 K with observed magnitude, roughly 2 wt% of total chromium should be detected by the AAS analysis. Similarly, roughly 0.2 wt% of chromium should be detected in the FeS_Cape_York sample. The results of the AAS analysis clearly reveal much lower total chromium content in both troilite samples (1000 times lower for the FeS_Bruderheim sample and 10 times lower for the FeS_Cape_York sample). Moreover, the FeS_Bruderheim sample, having lower chromium content, exhibits an order of magnitude higher magnetic response compared to that observed for the FeS_Cape_York sample, thus giving no positive correlation between the chromium content and magnetic properties.

[42] 3. The EMA on individual grains reveal similar low concentration levels of chromium as derived from the AAS (see Table S1 in the auxiliary material). Apart from S and Fe, EMA indicates also a very low content of other elements such as Mn, Ni, and Co. This implies that possible separate phases formed by such elements, being thus in an extremely low concentration, would not account for the observed dramatic change in troilite magnetic properties below ≈70 K.

[43] 4. The search for a troilite inclusion was also conducted on a Bruderheim meteorite thin section using SEM, EMA and in BSE mode on a submicron scale. Few chromite grains were observed in association with troilite, but never encapsulated within troilite.

[44] 5. To test a detectability of the chromite impurity within the troilite by XRD, a test sample was prepared by mixing 3 wt% of natural chromite with synthetic FeS. The chromite diffractions are unambiguously identified in the resulting XRD pattern of synthetic FeS (see Figure S7 in Text S2 in the auxiliary material) and subsequent quantitative phase analysis employing the Rietveld refinement yielded ≈2 wt% of chromite similar to our initial mixing content. Therefore, we can conclude that even slightly lower chromite concentrations would be detectable in the XRD patterns of the FeS samples. On the contrary, no indications of chromite diffractions were observed in the FeS_Bruderheim and FeS_Cape_York sample as well as in original synthetic FeS sample. The reason why the synthetic FeS sample was not used for magnetic measurements is that it contains also ≈4 wt% of metallic iron producing a high magnetic background.

[45] 6. From the magnetic viewpoint, the RT SIRM cycle can partially help interpret the nature of the transition. From the absence of a magnetization recovery at the transition temperature during RT SIRM cooling in the chromite bearing meteorite samples, *Gattacceca et al.* [2011] argue that the transition is caused by a chromite transition from the paramagnetic to the ordered magnetic state. However, the partial recovery of the magnetic moment at ≈70 K upon cooling of the RT SIRM can be seen in our troilite samples (see Figure 3c). Thus, the mechanism behind the transition in our troilite samples is different; the transition proceeds most likely from the antiferromagnetic to the ferromagnetic, ferrimagnetic, and/or canted antiferromagnetic state and is not related to hypothetical chromite impurity and its Curie point. Furthermore, the shape of the induced FC magnetization curves in our troilite samples does not resemble the well-known Curie-Weiss law [*Dunlop and Özdemir*, 1997; *Blundell*, 2001] on heating at temperatures above 70 K which does not support the chromite contamination case (the transition from the ordered magnetic state to the paramagnetic one).

[46] The above mentioned data did not revealed chromite to be present within our samples in required quantities and thus, we cannot attribute the observed magnetic phenomena to the chromite contamination as proposed by *Gattacceca et al.* [2011]. To our best knowledge, other Fe and S bearing minerals and/or with relevant substitution do not exhibit similar transition or Curie temperature at ≈70 K. Thus, we interpret this magnetic transition to be an intrinsic property of a highly stoichiometric and chemically pure troilite.

4. Conclusions

[47] The observation of identical magnetic behavior of both studied troilite samples confirms that the magnetic transition at ≈70 K could be a general troilite material property. The detailed magnetic (especially the RT SIRM cycle measurements), structural (XRD measurements), and chemical analysis (AAS, EMA, BSE) ruled out presence of chromite with concentrations required to account for the observed magnetic changes at ≈70 K as suggested by *Gattacceca et al.* [2011]. There is also no indication of such transition in non-stoichiometric pyrrhotites ($Fe_{1-x}S$). Moreover, the ≈70 K magnetic transition has been recently independently observed by *Hoffmann et al.* [2011] in the troilite extract from the iron Nantan IIICD meteorite. Thus, a presence of this magnetic transition is unique for stoichiometric (FeS) end-member of pyrrhotite group – troilite.

[48] The magnetic transition proceeds from the high-temperature antiferromagnetic state to the low-temperature ferromagnetic, ferrimagnetic, and/or canted antiferromagnetic regime (associated with a rapid increase in the magnetization). Both investigated samples show that this transition is not affected by the strength of the external magnetic field (up to 1 T) and is manifested by a change in the profile of the hysteresis loops around the origin. Furthermore, Mössbauer spectroscopy measurements exclude that this magnetic transition resembles the characteristics of the Morin-type (i.e., structurally driven) transition.

[49] As discussed in the review work by *Kohout et al.* [2010], troilite is widely present in various extraterrestrial materials (i.e., cosmic dust) and thus, a change in its magnetic properties below ≈70 K has to be considered in modeling and interpreting the magnetism of extraterrestrial bodies such as comets. On the contrary, other extraterrestrial materials as ordinary chondrites and their parent bodies – stony asteroids – may contain a significant amount of chromite which has its Curie point reported within a similar temperature range as for troilite and much stronger magnetic response compared to troilite [*Gattacceca et al.*, 2011]. Thus, in these materials, chromite clearly magnetically dominates at similar low temperatures over troilite.

[50] **Acknowledgments.** This work has been supported by the grant agency of the Academy of Sciences of the Czech Republic (grants KAN115600801 and KJB300130903), projects of the Ministry of Education of the Czech Republic (projects 1M6198959201 and MSM6198959218),

Academy of Sciences of the Czech Republic Research Plan (project AV0Z 30130516), Operational Program Research and Development for Innovations – European Social Fund (CZ.1.05/2.1.00/03.0058), and the internal grant of Palacky University in Olomouc, Czech Republic (PrF_2010_010). We would like to thank Roman Skála and Peter J. Wasilewski for providing troilite samples. Sample of natural chromite used within this study was kindly provided by the Moravian Museum in Brno, Czech Republic.

References

Arnold, R. G. (1962), Equilibrium relations between pyrrhotite and pyrite from 325° to 743°C, *Econ. Geol.*, *57*, 72–90, doi:10.2113/gsecongeo.57.1.72.

Arnold, R. G., and L. E. Reichen (1962), Measurement of the metal content of naturally occurring, metal-deficient, hexagonal pyrrhotite by an *x*-ray spacing method, *Am. Mineral.*, *47*, 105–111.

Blundell, S. (2001), *Magnetism in Condensed Matter*, Oxford Univ. Press Inc., New York.

Cuda, J., R. Zboril, O. Schneeweiss, J. Tucek, V. Prochazka, M. Maslan, and P. Tucek (2010), Mössbauer study and macroscopic/global magnetic behavior of powdered Ilmenite ($FeTiO_3$) sample, in *Mössbauer Spectroscopy in Materials Science: 2010, AIP Conference Proceedings*, vol. 1258, edited by J. Tucek and M. Miglierini, pp. 55–67, Am. Inst. of Phys., Melville, N. Y.

Dunlop, D., and Ö. Özdemir (1997), *Rock Magnetism: Fundamentals and Frontiers*, Cambridge Univ. Press, Cambridge, U. K., doi:10.1017/CBO9780511612794.

Gattacceca, J., P. Rochette, F. Lagroix, P.-E. Mathé, and B. Zanda (2011), Low temperature magnetic transition of chromite in ordinary chromites, *Geophys. Res. Lett.*, *38*, L10203, doi:10.1029/2011GL047173.

Gosselin, J. R., M. G. Townsend, R. J. Tremblay, and A. H. Webster (1976), Mössbauer effect in single-crystal $Fe_{1-x}S$, *J. Solid State Chem.*, *17*, 43–48, doi:10.1016/0022-4596(76)90199-7.

Hägg, G., and I. Sucksdorff (1933), Die Kristallstruktur von Troilit und Magnetkies, *Z. Phys. Chem. B*, *22*, 444–452.

Haraldsen, H. (1937), Magnetochemische Untersuchungen. XXIV. Eine thermomagnetische Untersuchung der Umwandlungen im Troilit-Pyrrhotin-Gebiet des Eisen-Schwefel-Systems, *Z. Anorg. Allg. Chem.*, *231*, 78–96, doi:10.1002/zaac.19372310110.

Haraldsen, H. (1941), Über die Hochtemperaturumwandlungen der Eisen (II)-Sulfidmischkristalle, *Z. Anorg. Allg. Chem.*, *246*, 195–226, doi:10.1002/zaac.19412460207.

Hirahara, E., and M. Murakami (1958), Magnetic and electrical anisotropies of iron sulfide single crystals, *J. Phys. Chem. Solids*, *7*, 281–289, doi:10.1016/0022-3697(58)90278-6.

Hoffmann, V. H., M. Torii, M. Funaki, R. Hochleiter, M. Kaliwoda, T. Michouchi, and M. Zolensky (2011), Magnetic phases of Almahata Sitta: New results, *Lunar Planet. Sci.*, *XLII*, Abstract 2191.

Horwood, J. L., M. G. Townsend, and A. H. Webster (1976), Magnetic susceptibility of single-crystal $Fe_{1-x}S$, *J. Solid State Chem.*, *17*, 35–42, doi:10.1016/0022-4596(76)90198-5.

Keller-Besrest, F., and G. Collin (1990), Structural aspects of the α transition in stoichiometric FeS: Identification of the high-temperature phase, *J. Solid State Chem.*, *84*, 194–210, doi:10.1016/0022-4596(90)90319-S.

Kohout, T., A. Kosterov, M. Jackson, L. J. Pesonen, G. Kletetschka, and M. Lehtinen (2007), Low-temperature magnetic properties of the Neuschwanstein EL6 meteorite, *Earth Planet. Sci. Lett.*, *261*, 143–151, doi:10.1016/j.epsl.2007.06.022.

Kohout, T., A. Kosterov, J. Haloda, P. Týcová, and R. Zbořil (2010), Low-temperature magnetic properties of iron-bearing sulfides and their contribution to magnetism of cometary bodies, *Icarus*, *208*, 955–962, doi:10.1016/j.icarus.2010.03.021.

Li, F., and H. F. Franzen (1996), Phase transitions in near stoichiometric iron sulfide, *J. Alloys Compd.*, *238*, 73–80, doi:10.1016/0925-8388(96)02207-4.

Murakami, M. (1959), Alpha-transformation mechanism of the antiferromagnetic iron sulfide, *Sci. Rep. Tohoku Univ., Ser. 1*, *43*, 53–61.

Murakami, M., and E. Hirahara (1958), A certain anomalous behavior of iron sulfides, *J. Phys. Soc. Jpn.*, *13*, 1407, doi:10.1143/JPSJ.13.1407.

Schwarz, E. J., and D. J. Vaughan (1972), Magnetic phase relations of pyrrhotite, *J. Geomagn. Geoelectr.*, *24*, 441–458, doi:10.5636/jgg.24.441.

Skála, R., I. Císařová, and M. Drábek (2006), Inversion twinning in troilite, *Am. Mineral.*, *91*, 917–921, doi:10.2138/am.2006.1999.

Vandenberghe, R. E., E. De. Grave, and C. Landuydt (1990), Some aspects concerning the characterization of iron oxides and hydroxides in soils and clays, *Hyperfine Interact.*, *53*, 175–195, doi:10.1007/BF02101046.

Wang, H., and I. Salveson (2005), A review on the mineral chemistry of the non-stoichiometric iron sulphide, $Fe_{1-x}S$ ($0 \leq x \leq 0.125$): Polymorphs, phase relations and transitions, electronic and magnetic structures, *Phase Transit.*, *78*, 547–567, doi:10.1080/01411590500185542.

Zboril, R., M. Mashlan, and D. Petridis (2002), Iron(III) oxides from thermal processes-synthesis, structural and magnetic properties, Mossbauer spectroscopy characterization, and applications, *Chem. Mater.*, *14*, 969–982, doi:10.1021/cm0111074.

J. Cuda, J. Filip, R. Prucek, J. Tucek, and R. Zboril, Regional Centre of Advanced Technologies and Materials, Department of Physical Chemistry, Palacky University, Slechtitelu 11, 783 71 Olomouc, Czech Republic. (zboril@prfnw.upol.cz)

J. Haloda, Czech Geological Survey, Geologická 6, 152 00 Praha 5, Czech Republic.

T. Kohout, Department of Physics, University of Helsinki, PO Box 64, FI-00014 Helsinki, Finland. (tomas.kohout@helsinki.fi)

Příloha C

Čuda, J., Kohout, T., Tuček, J., Filip, J., Medřík, I., Mašláň, M., Zbořil, R.:

Mössbauer study and magnetic measurement of troilite extract from natan iron meteorite

MSMS 2012, *Conference Proceedings*, 1489, 145–153 (2012)

Mössbauer Study and Magnetic Measurement of Troilite Extract from Natan Iron Meteorite

J. Čuda[a], T. Kohout[b,c], J. Tuček[a], J. Filip[a], I. Medřík[a], M. Mashlan[d] and R. Zbořil[a]

[a] *Regional Centre of Advanced Technologies and Materials, Departments of Physical Chemistry and Experimental Physics, Faculty of Science, 17. listopadu 1192/12, Palacky University, Olomouc, Czech Republic*
[b] *Department of Physics, University of Helsinki, Helsinki, Finland*
[c] *Institute of Geology, Academy of Sciences of the Czech Republic, Prague, Czech Republic*
[d] *Department of Experimental Physics, Faculty of Science, 17. listopadu 1192/12, Palacky University, Olomouc, Czech Republic*

Abstract. We focused on the troilite in-field Mössbauer spectrum at 5 K in order to confirm or rule out the interpretation of two sextets for other troilite system extracted from the Natan IIICD iron meteorite. Beside the Mössbauer spectroscopy investigation, the global magnetic response of troilite extract was measured. Detailed analysis of field-cooled (FC) induced magnetization (10 mT) showed a similar profile to daubreelite ($FeCr_2S_4$) at temperatures below ~170 K. Induced-FC, temperature dependence of remanent magnetization, and room temperature saturation isothermal remanent magnetization (RT SIRM) magnetization do not show any significant change at low temperatures (~70 K) related to prior magnetic studies for troilite. In order to quantify a magnetic response of the troilite extract from the Nantan IIICD iron meteorite, the hysteresis loops at 5 and 300 K were measured in external magnetic fields up to 7 T. Hysteresis parameters of coercive field (B_C) and saturation magnetization (M_S) were found to be 56 mT and 2 Am^2/kg at 5 K, respectively. At room temperature, the values of these parameters are lower (B_C ~ 14 mT and M_S ~ 1.44 Am^2/kg).

Keywords: Troilite, zero- and in-field Mössbauer spectroscopy, magnetization measurements, Natan IIICD iron meteorite
PACS: 76.80.+y, 91.25.F

INTRODUCTION

Very rarely occurring troilite mineral (FeS) is the end-member of the pyrrhotite group with a stoichiometric or nearly stoichiometric iron and sulfur content. Troilite has one crystallographic position of iron and crystallizes in the $P\bar{6}2c$ space group [1] below the crystallographic α-transition (at ~413 K) when the crystal symmetry can be described as a 2C NiAs superstructure with hexagonal lattice parameters $a = (3)^{1/2} - a_{NiAs}$ and $c = 2c_{NiAs}$ [2]. Passing the α-transition temperature, the troilite crystal structure changes to a high-temperature NiAs-type structure with $P6_3mmc$ symmetry. Above room temperature, magnetic properties of troilite have been a subject of many studies [3–10]. Magnetic susceptibility measurements carried out on a synthetic

Mossbauer Spectroscopy in Materials Science - 2012
AIP Conf. Proc. 1489, 145-153 (2012); doi: 10.1063/1.4759483

sample crystal ($Fe_{0.996}S$) revealed antiferromagnetic ordering with iron magnetic moments lying along the *c*-axis of the NiAs subcell (c_{NiAs}) below the α-transition [11].

Pale/dark grayish brown troilite is usually associated with other iron sulphides and can be mostly found in the extraterrestrial materials. In these systems, the presence of troilite can be documented by observation of its Néel temperature at ~600 K [12] and usually low change in the low-temperature (LT) magnetic behavior taking place at ~70 K [13,14]. The nature of LT magnetic "transition" is still an open issue. Kohout et al. [13] described the magnetic evolution at ~70 K as a Morin-like transition based on LT magnetization measurement of troilite extract from meteorite. However, other authors ascribed this behavior to the presence of chromite impurity in the sample based on LT magnetic response of chromite in ordinary chondrites [15]. Recently, two very pure nature troilite originated from a meteorite were investigated [14]. The presence of the Morin-like transition in the temperature range from 5 to 300 K and the presence of chromite impurity responsible for LT magnetic response below ~70 K were excluded. To the best of our knowledge, LT in-field Mössbauer spectra of the FeS system has been published only in one paper [14]. The spectra were fitted by means of two sextet components. This conclusion is quite interesting because only one crystallographic position of iron is expected in the FeS system. Thus, the question arises whether the fitting of two sextet components is necessary to correctly interpret the in-field Mössbauer spectra of the FeS system.

In the present paper, we re-examine the low-temperature Mössbauer spectra and performed magnetization measurements for troilite sample derived from meteorite having different origin than in previous studies [13,14]. We focus on correctness of the fit of the in-field Mössbauer spectra. In addition, we monitor global magnetic behavior of troilite extracted from the Natan IIICD iron meteorite in order to find the well known signs of troilite magnetic properties such as (i) an increase in the magnetic response at ~70 K observed in temperature dependence of magnetization and (ii) a profile change around the origin of LT hysteresis loops observed for previously studied troilite system [14].

EXPERIMENTAL DETAILS

The FeS_Natan sample is a polycrystalline fragment from the Natan iron meteorite. The Natan meteorite impacted in Natan County, Guangxi, China, and it is a nickel-iron meteorite with an average composition of 92.35% iron and 6.96% nickel, being classified as a IIICD coarse octahedrite. Our troilite extract was kindly provided by Viktor Hoffman from the Department of Geosciences, University of Tuebingen, Germany.

The crystal structure of the studied sample was investigated by X-ray powder diffraction (XRD). After magnetization measurement, the FeS_Natan sample was powdered and its XRD pattern was recorded at room temperature on a PANalytical X'Pert PRO (The Netherlands) instrument in the Bragg-Brentano geometry with an Fe-filtered CoK_α radiation (40 kV, 30 mA). Samples were spread on a zero-background Si slides and continuously scanned with a resolution of 0.017°. The

acquired patterns were evaluated using the X'Pert HighScore Plus software (PANalytical) in combination with PDF-4+ and ICSD databases.

A ^{57}Fe Mössbauer spectrometer with a ^{57}Co(Rh) source of γ-rays was used for Mössbauer measurements. The values of the derived hyperfine Mössbauer parameters are referred to the metallic iron (α-Fe) at room temperature. For in-field Mössbauer measurements, a parallel geometry was used with an external magnetic field of 5 T applied parallel to the γ-rays propagation. Both zero- and in-field Mössbauer spectra were fitted by Lorentzian line shapes using the least squares method in the MossWinn computer program. The FeS_Natan sample was powdered prior to Mössbauer spectroscopy measurements.

The magnetic response of the studied sample was investigated using a SQUID magnetometer (MPMS XL-7 magnetometer, Quantum Design). The temperature dependence of magnetization was recorded in the sweep mode employing following measuring procedures: (i) field-cooled induced magnetization (induced-FC) measurement; (ii) zero-field induced magnetization (induced-ZFC) measurement; (iii) field-cooled remanent magnetization (rem-FC); (iv) zero-field-cooled remanent magnetization (rem-ZFC); and (v) room temperature saturation isothermal remanent magnetization (RT SIRM) cycle. The measurement procedures are described in details elsewhere [14].

RESULTS AND DISCUSSION

XRD Analysis

The XRD pattern of the FeS_Natan sample, acquired at room temperature, is depicted in Fig. 1. It confirms the presence of crystalline troilite with a crystal structure below α-transition (PDF No. 01-089-4076). However, the occurrence of other peaks belonging to impurity of daubreelite structure (PDF No. 01-089-2617) is evident. The Rietveld refinement was used exclusively to evaluate the content of two

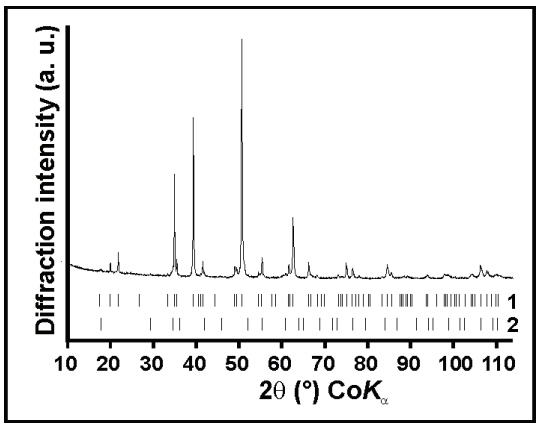

FIGURE 1. XRD pattern of the powdered FeS_Natan sample. The respective PDF cards are 01-089-4076 (FeS; troilite) and 01-089-2617 ($FeCr_2S_4$; daubreelite).

phases in the studied sample. Quantitative phase analysis indicates that the FeS_Natan sample is made up of ~94% of troilite and only ~6% of daubreelite. The presence of small amount of other phases in the FeS_Natan can be found with respect to the troilite separation from the compact meteorite. However, we expect that their contents are well below 2%.

Mössbauer Study

The zero-field ^{57}Fe Mössbauer spectra collected at 5 K and at room temperature are depicted in Fig. 2a and 2b, respectively. At first sight, the spectral profiles are symmetrical and can be sufficiently described by one sextet component, indicating well crystalline magnetically ordered material. The hyperfine parameters of zero-field Mössbauer spectra are listed in Table 1. When fitting the Mössbauer spectra, we found that the asymmetry parameter (η) of the electric field gradient (EFG) is equal to 0. Furthermore, the azimutal angle (ϕ) the internal hyperfine magnetic field (B_{hf}) makes with axes of the EFG and together with the angle (θ) between B_{hf} and the principal axis V_{zz} of the EFG tensor were set to zero. This restrictions corresponds to simplified, however, more frequently used model for fitting troilite spectra rather than a model proposed by Grandjean et al. [16] with η = 0.3, θ = 48°, and ϕ = 49°. Except the change of the isomer shift (δ) due to its temperature dependence, we do not observe any significant variation in the hyperfine parameters between the spectra recorded at room temperature and at 5 K (see Table 1). This confirms results suggested by Cuda et al. [14] that the Morin-like transition does not occur in the troilite system at ~70 K. If the Morin-like transition took place, the significant change in the quadruple splitting parameter (ΔE_Q) would be observed due to spin reorientation. For example, in hematite system upon cooling through ~265 K, ΔE_Q is changed from – 0.19 mm/s to + 0.37 mm/s [17,18].

The in-field Mössbauer spectrum of the FeS_Natan sample measured at 5 K and in an external magnetic field of 5 T is depicted in Fig. 2c. The spectrum was fitted with a hyperfine magnetic field distribution method. The distribution of effective hyperfine magnetic field (see Fig. 2d) unambiguously shows only one local maximum at ~33.6 T. Thus, only one sextet component should be used for correct fitting of in-field Mössbauer data as expected since there is only one crystallographic position of iron in FeS. The possible fitting of two sextet components ascribed to two independent magnetic sublattices under high applied magnetic fields seems not to be fully reflecting physical properties and crystallographic arrangement in the FeS system. Thus, possible explanation based on non-ideal antiferromagnetic behavior, as observed in antiferromagnetic material [19], should not be used to interpret the in-field Mössbauer spectrum of the troilite system.

Last but not least, comparing zero-field (see Fig. 2b) and in-field (see Fig. 2c) Mössbauer spectra recorded at 5 K, the increasing values of intensities of the 2nd and 5th resonant lines are observed together with broadening of line peaks. Moreover, the effective hyperfine magnetic field (B_{eff}) value is slightly larger than B_{hf} (see Table 1). If we take into account that these Mössbauer experimental data at 5 K and in 5 T correspond to an averaged spectrum over all possible field directions in the powdered (i.e., polycrystalline) FeS_Natan sample, then the fitting model known for an

antiferromagnetic material showing a spin-flop transition must be used [20,21], i.e., one sextet component. This is in good agreement with distribution of B_{eff} showing only one dominant maximum (see Fig. 2d).

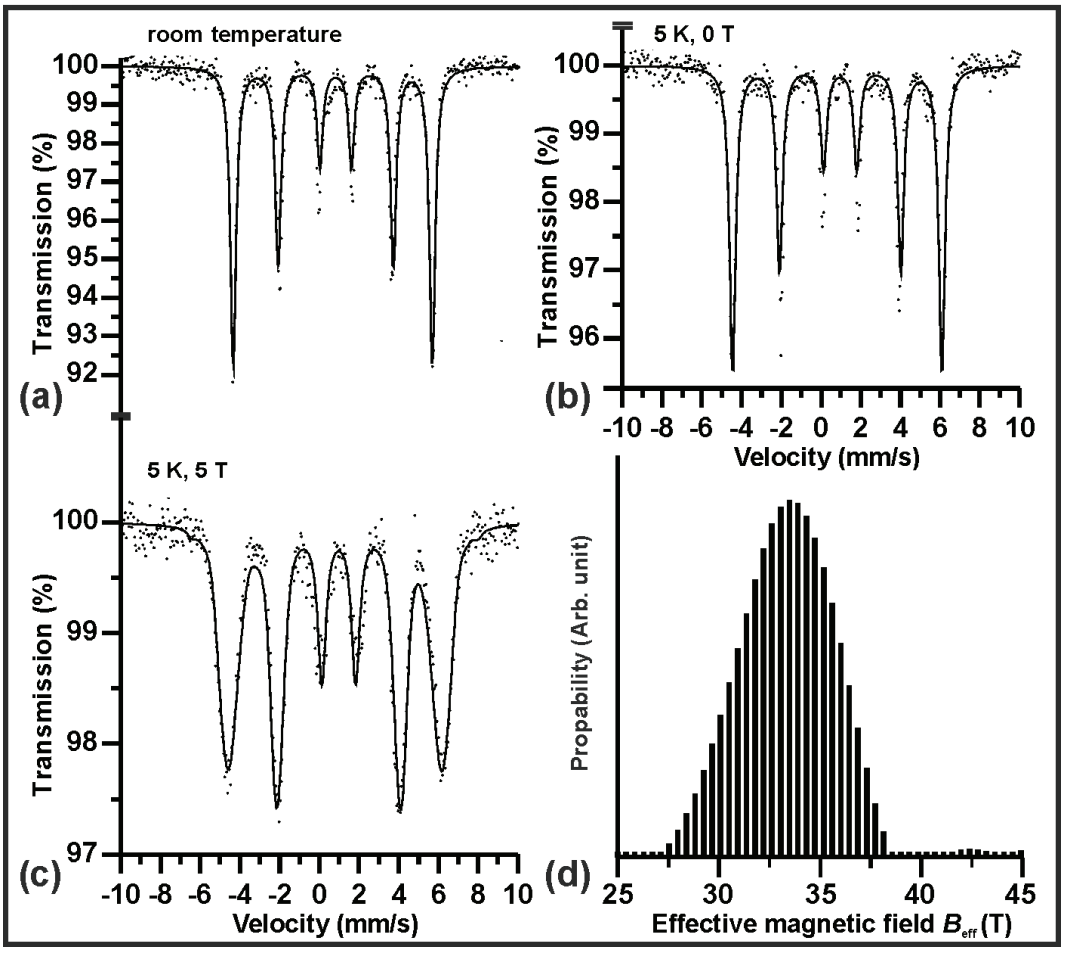

FIGURE 2. Mössbauer spectra of the FeS_Natan sample measured at (a) room temperature, (b) 5 K and 0 T, and (c) 5 K and 5 T. (d) Distribution of the effective hyperfine magnetic field (B_{eff}) derived from the Mössbauer spectrum recorded at 5 K and in 5 T.

TABLE 1. Hyperfine parameter values, derived from the recorded Mössbauer spectra of the FeS_Natan sample where T is the temperature of measurement, B_{ext} is the external magnetic filed, δ is the isomer shift, ΔE_Q is the quadrupole splitting, B_{hf} is the magnetic hyperfine field, B_{eff} is the effective magnetic field (i.e., B_{eff} is a vector sum of B_{ext} and B_{hf}), Γ is the linewidth, and A is relative spectra area of each component.

T (K)	B_{ext} (T)	$\delta \pm 0.01$ (mm/s)	$\Delta E_Q \pm 0.01$ (mm/s)	$B_{\mathrm{hf}} \pm 0.3$ (T)	$B_{\mathrm{eff}} \pm 0.3$ (T)	$\Gamma \pm 0.01$ (mm/s)	A (%)
300	0	0.76	– 0.15	31.2	----------	0.35	100
5	0	0.89	– 0.14	32.8	----------	0.38	100
5	5	0.88	– 0.18	----------	33.7	----------	100

Macroscopic Magnetization Measurements

The hysteresis loops describing the troilite extract from the Nantan IIICD iron meteorite at various temperatures are depicted in Fig. 3a and the derived hysteresis parameters are summarized in Table 2. As one can clearly see, the hysteresis loops are typical for ferromagnetic and/or ferrimagnetic materials for which non-zero values of coercive field, S-shape of hysteresis loop and tendency to saturation at high external magnetic field are frequently observed. If we take into account known value of saturation magnetization (M_S) for daubreelite (M_S ~ 32 Am^2/kg at 80 K) [22] and possible occurrence of this phase in the FeS_Natan sample (~6% from XRD measurement), we can well describe the hysteresis loops at 5 and 100 K as a manifestation of daubreelite impurity in the FeS_Natan sample. Generally, we can assume another magnetic material contributing to these hysteresis loops besides daubreelite and troilite. At room temperature, daubreelite is paramagnetic and troilite is antiferromagnetic. Then, observation of ferromagnetic and/or ferrimagnetic sign at 300 K (see Fig. 3a) is unexpected and would imply a presence of another magnetic impurity with a quite high value of M_S. We can clearly say that the hysteresis loops reflect impurities in the FeS_Natan sample rather than low magnetic response of most abundant troilite phase in the studied sample. Thus, when passing through ~70 K, the change in the profile of hysteresis loop around the origin, associated with pure troilite[14] is not observable in the studied system.

The temperature dependence of the induced-FC and induced-ZFC are shown in Fig. 3b. In this case, the magnetization vs. temperature curves yield a change of the trend at ~169 K and below this temperature, the curve behavior is very similar to that published for daubreelite [23–27]: (i) the sudden increase in magnetization seems to be a demonstration of daubreelite Curie temperature (T_C ~ 150–170 K) the value of which depends on its exact chemical composition; and (ii) magnetic transition (characterized by spin-glass-like features and cubic-to-triclinic symmetry reduction within a crystallographic domain) may manifest itself by a higher local maximum at ~70 K in the induced-FC curve (see Fig. 3b).

The pure troilite is rarely occurring mineral and there are only two very pure troilite systems which show magnetic “characteristic” anomaly at ~70 K [13,14]; however, the nature of this transition is still unknown. In order to expand the number of troilite samples showing LT thermodynamic-like transition from a high-temperature antiferromagnetic regime to a low-temperature ordered state of ferromagnetic, ferrimagnetic and/or canted antiferromagnetic origin accompanied by enhancement in magnetization values at ~70 K [14], we monitored the temperature evolution of induced FC (see Fig. 3b), remanent FC and ZFC (see Fig. 3c), and RT SIRM (see Figure 3d) values. However, similarly to hysteresis loops, these measurements are affected by impurity in the FeS_Natan sample. Thus, the demonstration of troilite magnetic behavior is overshadowed by the magnetic response of the impurity (i.e., daubrelite and possibly by another phase with a quite high value of M_S).

TABLE 2. Parameters of hysteresis loops of the FeS_Natan sample, measured at 5 K, 100 K, and room temperature, after slope correction, where M_{max+} is the maximum magnetization at + 7 T, M_{min-} is the maximum magnetization at – 7 T, B_{C+} is the "up-down" coercivity, B_{C-} is the "down-up" coercivity, M_{R+} is the "up-down" remanent magnetization, and M_{R-} is the "down-up" remanent magnetization.

T (K)	$M_{max+} \pm 0.01$ (Am^2/kg)	$M_{max-} \pm 0.01$ (Am^2/kg)	$B_{C+} \pm 1$ (mT)	$B_{-} \pm 1$ (mT)	$M_{R+} \pm 0.01$ (Am^2/kg)	$M_{R-} \pm 0.01$ (Am^2/kg)
5	2.01	– 2.02	56	– 58	0.81	– 0.82
100	1.96	– 1.97	20	– 20	0.59	– 0.59
300	1.44	– 1.44	14	– 14	0.39	– 0.39

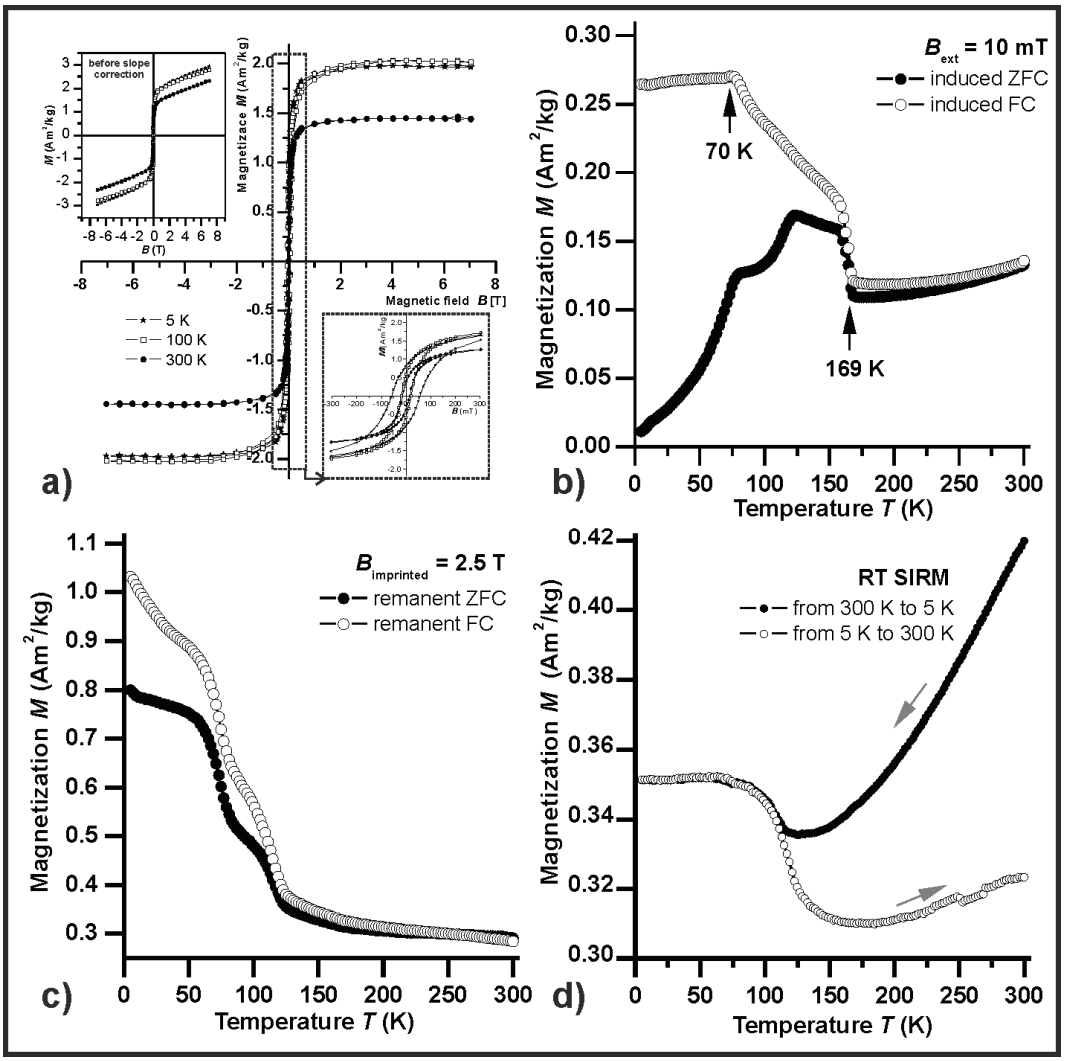

FIGURE 3. Macroscopic magnetic response of the FeS_Natan sample: (a) hysteresis loops at 5, 100, and 300 K, (b) field-cooled induced (induced-FC) magnetization and zero-field induced (induced-ZFC) magnetization, (c) field-cooled measurement of remanence (rem-FC) and zero-field-cooled measurement of remanence (rem-ZFC), and (d) room temperature saturation isothermal magnetization (RT SIRM) cycle.

CONCLUSIONS

In the present study, the polycrystalline fragment from the Natan iron meteorite (FeS_Natan sample) was studied by employing zero-field and in-field ^{57}Fe Mössbauer spectroscopy and magnetization measurements. Following conclusions can be drawn from the obtained results:

(1) From the temperature evolution of the zero-field Mössbauer spectra of the FeS_Natan sample, recorded at room temperature and at 5 K, we do not observe any significant change of hyperfine parameters which would support the suggestion of Morin-like transition occurring within this temperature range.
(2) The low-temperature in-field Mössbauer spectra of the FeS system should be fitted by means of one sextet component as it is typical for antiferromagnetic material showing a spin-flop transition under external magnetic fields.
(3) Magnetization measurements show a dominant magnetic behavior of impurity in the FeS_Natan sample which overshadows the magnetic response of troilite (FeS) in the sample. Thus, it was not possible to observe low-temperature troilite magnetic properties.

ACKNOWLEDGMENTS

The authors gratefully acknowledge the support by the Grant Agency of the Academy of Sciences of the Czech Republic (Grant No. KJB300130903), Institute of Geology ASCR, v.v.i., Research Plan (Project No. AV0Z 30130516), Czech Science Foundation (GACR P108/11/1350), the internal grant of Palacky University in Olomouc, Czech Republic (Project No. PrF_2011_013), the LH - KONTAKT II research project (Project No. LH12079 of the Ministry of Education, Youth and Sports of the Czech Republic), and the Operational Program Research and Development for Innovations – European Regional Development Fund (CZ.1.05/2.1.00/03.0058 of the Ministry of Education, Youth and Sports of the Czech Republic).

REFERENCES

1. H. T. Evans, *Science* **167**, 621–623 (1970).
2. G. Hägg and I. Sucksdorff, *Phys. Chem. B* **22**, 444–452 (1933).
3. H. Haraldsen, *Z. Anorg. Allg. Chem*. **231**, 78–96 (1937).
4. H. Haraldsen, *Z. Anorg. Allg. Chem.* **246**, 195–226 (1941).
5. E. Hirahara and M. Murakami, *J. Phys. Chem. Solids* **7**, 281–289 (1958).
6. M. Murakami and E. Hirahara, *J. Phys. Soc. Jpn.* **13**, 1407–1407 (1958).
7. M. Murakami, *Science Reports, Tohoku University, Series 1*, **43**, 53–61 (1959).
8. E. J. Schwarz and D. J. Vaughan, *J. Geomag. Geoelectr.* **24**, 441–458 (1972).
9. J. R. Gosselin, M. G. Townsend, R. J. Tremblay and A. H. Webster, *J. Solid State Chem.* **17**, 43–48 (1976).
10. F. Li and H. F. Franzen, *J. Alloy. Compd.* **238**, 73–80 (1996).
11. J. L. Horwood, M. G. Townsend and A. H. Webster, *J. Solid State Chem.* **17**, 35–42 (1976).
12. H. Wang, and I. Salveson, *Phase Transit.* **78**, 547–567 (2005).
13. T. Kohout, A. Kosterov, M. Jackson, L. J. Pesonen, G. Kletetschka and M. Lehtinen, *Earth Planet. Sci. Lett.* **261**, 143–151 (2007).

14. J. Cuda, T. Kohout, J. Tucek, J. Haloda, J. Filip, R. Prucek and R Zboril, *J. Geophysic. Res.* **116**, B11205 (2011).
15. J. Gattacceca, P. Rochette, F. Lagroix, P. –E. Mathé and B. Zanda, *Geophys. Res. Lett.* **38**, L10203 (2011).
16. F. Grandjean, G. L. Long, D. Hautot and D. L. Whitney, *Hyperfine Interact.* **116**,105–115 (1998).
17. R. E. Vandenberghe, E. De. Grave and C. Landuydt, *Hyperfine Interact.* **53**, 175–196 (1990).
18. R. Zboril, M. Mashlan and D. Petridis, *Chem. Mater.* **14**, 969–982 (2002).
19. J. Cuda, R. Zboril, O. Schneeweiss, J. Tucek, V. Prochazka, M. Maslan and P. Tucek, "Mössbauer Study and Macroscopic/Global Magnetic Behavior of Powdered Ilmenite ($FeTiO_3$) Sample", in *Mössbauer Spectroscopy in Materials Science – 2010*, edited by J. Tuček and M. Miglierini, AIP Conference Proceedings 1258, Melville, NY: American Institute of Physics, 2010, pp. 55–67.
20. Q. A. Pankhurst and R. J. Pollard, *J. Phys.-Condens. Matter* **2**, 7329–7337 (1990).
21. C. E. Johnson, *J. Phys. D-Appl. Phys.* **29**, 2266–2273 (1996).
22. A. Kosterov, T. Kohout, M. Jackson, G. Kletetschka and M. Lehtinen, *American Geophysical Union, Fall Meeting 2007, abstract #GP24A-06* (2007).
23. V. Tsurkan, M. Baran, R. Szymczak, H. Szymczak and R. Tidecks, *Physica B* **296**, 301–305 (2001).
24. V. Tsurkan, I. Fita, M. Baran, R. Puzniak, D. Samusi, R. Szymczak, H. Szymczak, S. Klimm, M. Klemm, S. Horn and R. Tidecks, *J. Appl. Phys.* **90**, 875–881 (2001).
25. V. Tsurkan, J. Hemberger, M. Klemm, S. Klimm, A. Loidl, S. Horn and R. Tidecks, *J. Appl. Phys.* **90**, 4639–4644 (2001).
26. D. Maurer, V. Tsurkan, S. Horn and R. Tidecks, *J. Appl. Phys.* **93**, 9173–9176 (2003).
27. C. Müller, V Zestrea, V. Tsurkan, S. Horn, R. Tidecks and A. Wixforth, *J. Appl. Phys.* **99**, 023906 (2006).

Příloha D

Čuda, J., Kohout, T., Filip, J., Tuček, J., Kosterov, A., Haloda, J., Skála, R., Santala, E., Medřik, I., Zbořil, R.:

Low-temperature magnetism of alabandite: Crucial role of surface oxidation

Am. Miner., 98, 1550–1556 (2013)

American Mineralogist, Volume 98, pages 1550–1556, 2013

Low-temperature magnetism of alabandite: Crucial role of surface oxidation

Jan Čuda,[1,*] Tomáš Kohout,[2,3] Jan Filip,[1] Jiří Tuček,[1] Andrei Kosterov,[4,5] Jakub Haloda,[6] Roman Skála,[3] Eero Santala,[7] Ivo Medřík,[1] and Radek Zbořil[1]

[1]Regional Centre of Advanced Technologies and Materials, Departments of Physical Chemistry and Experimental Physics, Faculty of Science, Palacký University Olomouc, 17. listopadu 12, 771 46 Olomouc, Czech Republic
[2]Department of Physics, University of Helsinki, P.O. Box 64, 00014 Helsinki University, Finland
[3]Institute of Geology, Academy of Sciences of the Czech Republic v.v.i., Rozvojová 269, 165 00 Prague, Czech Republic
[4]Earth Physics Department, Faculty of Physics, Saint Petersburg University 198504 Peterhoff, Saint Petersburg, Russia
[5]Resource Center "Geomodel," Saint Petersburg University 198504 Peterhoff, Saint Petersburg, Russia
[6]Czech Geological Survey, Geologická 6, 152 00 Praha 5, Czech Republic
[7]Department of Chemistry, University of Helsinki, P.O. Box 55, 00014 Helsinki University, Finland

Abstract

Manganese(II) monosulphide crystallizes into three different polymorphs (α-, β-, and γ-MnS). Out of these, α-MnS, also known as mineral alabandite, is considered the most stable and is widespread in terrestrial materials as well as in extraterrestrial objects such as meteorites.

In this study, a low-temperature antiferromagnetic state of α-MnS was investigated using macroscopic magnetic measurements as induced and remanent field-cooled (FC) and zero-field-cooled (ZFC) magnetizations and magnetic hysteresis. Both natural alabandite and synthetic samples show: (1) Néel temperatures in a narrow temperature range around 153 K, and (2) a rapid increase of the magnetization around 40 K. An anomalous magnetic behavior taking place at about 40 K was previously ascribed to the magnetic transition from a high-temperature antiferromagnetic to a low-temperature ferromagnetic state documented for non-stoichiometric α-MnS slightly enriched in manganese. However, our detailed microscopic observations and, in particular, oxidation experiments indicate that the anomalous magnetic behavior around 40 K is caused by the presence of an oxide layer of ferrimagnetic hausmannite (Mn_3O_4) on the surface of α-MnS rather than being an intrinsic property of nearly stoichiometric α-MnS.

Keywords: Alabandite (MnS), hausmannite (Mn_3O_4), troilite (FeS), magnetism

Introduction

Alabandite is a manganese sulfide with theoretical composition MnS crystallizing in the cubic lattice of galena type (PbS). It occurs as an accessory mineral at many localities worldwide, mainly in epithermal base-metal sulfide veins, in low-temperature manganese deposits (Doelter 1926; Hewett and Rove 1930; Anthony et al. 2012) and also in marine sediments (Lepland and Stevens 1998). Locally, it is an important ore mineral of Mn. Its name is derived from its supposed discovery locality at Alabanda, Turkey. The type locality of alabandite is Sacarîmb, Romania (Anthony et al. 2012).

Apart from terrestrial localities, alabandite is also relatively abundant in certain types of meteorites, e.g., in E chondrites (Keil 1968; Zhang et al. 1995; Zhang and Sears 1996; Brearley and Jones 1998) and related achondritic aubrites (Keil and Fredriksson 1967; Ryder and Murali 1987; Lin et al. 1989; Mittlefehldt et al. 1998). It was also reported in some ureilites (Fioretti and Molin 1998) and winonaites (Mason and Jarosewich 1967).

Alabandite is paramagnetic at room temperature and orders antiferromagnetically below its Néel temperature T_N ~148 K (Heikens et al. 1977). A slightly higher T_N (~153 K) was later published by Pearce et al. (2006). A structural transition occurs at T ~130 K, which is interpreted as an abrupt inversion of the rhombohedral distortion of the f.c.c. lattice along [111] plane accompanied by a discontinuous change in the magnetic susceptibility observed in alabandite single crystals (Heikens et al. 1977).

Magnetic susceptibility and induced field-cooled and zero-field-cooled magnetization (in an external magnetic field of 10 mT) of antiferromagnetic alabandite below its T_N are low, typically in the range of 10^{-7} m^3/kg and 3–4 mAm^2/kg, respectively. The substitution of Mn^{2+} ions by Fe^{2+} has a pronounced effect on the Néel temperature, which increases with increasing iron content reaching ~185 K for the $Fe_xMn_{1-x}S$ system with $x = 0.2$ (Petrakovski et al. 2002). Still more iron-rich alabandite samples ($x > 0.25$) exhibit ferrimagnetic behavior above room temperature with Curie temperatures T_C between 730 K ($x = 0.27$) and 860 K ($x = 0.38$) (Loseva et al. 1998; Petrakovski et al. 2002). However, magnetization of this ferrimagnetic-ordered alabandite is weak, close to that of paramagnetic MnS.

It was reported that iron-free MnS samples with a slight excess of Mn show antiferro- to ferromagnetic transition at T ~40 K (Petrakovski et al. 2001). This transition manifests itself in a sharp increase by two orders of magnitude of induced magnetization on cooling. Such a sharp change in magnetic properties can significantly increase the magnetic response of alabandite at low temperatures and can potentially contribute to low-temperature

* E-mail: jan.cuda@upol.cz

0003-004X/13/0809–1550$05.00/DOI: http://dx.doi.org/10.2138/am.2013.4348

magnetic properties of extraterrestrial bodies (Kohout et al. 2010). A similar low-temperature magnetic transition is observed in troilite (FeS) (Kohout et al. 2007; Cuda et al. 2011) or at ~25 K for ilmenite ($FeTiO_3$) (Cuda et al. 2010). Moreover, Gattacceca et al. (2011) recently reported that chromite with Curie temperature in the 40–80 K range exists in certain meteorites and may significantly modify their low-temperature magnetic properties. Therefore, the verification, interpretation and quantification of this magnetic phenomenon in alabandite samples and its comparison to low-temperature magnetic properties of troilite and chromite are required and are the subject of this study.

Materials and methods

The basic characteristics of our samples are summarized in Table 1. Natural polycrystalline sample of alabandite (NA) originating from Broken Hill, New South Wales, Australia, sample Bm 1972,294, was kindly provided by the Natural History Museum, London. Additionally, nearly stoichiometric α-MnS was synthesized adopting two alternative procedures.

SA1 sample was prepared using a slightly modified solvothermal process of Biswas et al. (2007). First, manganese acetate [$(CH_3CO_2)Mn{\cdot}4H_2O$, purity >99.0%, Sigma Aldrich] and thiourea (CH_4N_2S, purity >99.0%, Sigma Aldrich) was mixed in a molar ratio of 1:3 with a water solvent, loaded into an ace pressure tube (Sigma Aldrich) and placed into a furnace at 190 °C for 17 h. Subsequently, the dried product was annealed in a helium atmosphere at temperatures up to 450 °C.

Sample SA2 was synthesized by direct thermal fusion of sulfur (purity >98.0%, Sigma Aldrich) and manganese (purity >99.0%, Sigma Aldrich) powders in stoichiometric molar ratio. The precursors were annealed twice in a sealed quartz tube under reduced pressure for 12 h at 700 °C including sample homogenization between two subsequent runs.

Measurements of the macroscopic magnetic response such as induced and remanent field-cooled (FC) and zero-field-cooled (ZFC) magnetizations and magnetic hysteresis measurements were carried out at the Institute for Rock Magnetism, University of Minnesota, and at the Regional Centre of Advanced Technologies and Materials, Palacký University Olomouc, using MPMS5S and MPMS XL-7 (both Quantum Design) SQUID magnetometers. Details of FC and ZFC measurement procedure are provided in supplementary material[1].

X-ray diffraction (XRD) patterns of all samples were recorded with a PANalytical X'Pert PRO MPD diffractometer (iron-filtered Co$K\alpha$ radiation: $\lambda = 0.178901$ nm, 40 kV, and 30 mA) in the Bragg-Brentano geometry. Samples were placed on a zero-background Si slides and scanned in a continuous mode (resolution of 0.017° 2θ, scan speed of 0.0016° 2θ per s). The identification of crystalline phases and Rietveld refinements were obtained using the software High Score Plus (PANalytical) in conjunction with the PDF-4+ and ICSD databases (ICSD collection codes: MnS, 41331; Mn_3O_4, 31094; Mn_2O_3, 76087; S, 63082). Peak shapes were modeled using the pseudo-Voigt function, separately refining the Caglioti parameters (*u*, *v*, *w*), unit-cell parameters, and a scale factor for each phase.

The bulk chemical composition of the SA2 sample was determined using a quantitative X-ray wavelength-dispersive spectral analysis on a MICROSPEC 3PC X-ray wavelength-dispersive system (WDS) on a CamScan 3200 scanning electron microscope (SEM) at the Czech Geological Survey. The analyses were performed using an accelerating voltage of 20 kV, 25 nA beam current, 1 μm beam size, and the ZAF correction procedures. The counting times were 30 s for all analyzed elements. A combination of natural and synthetic standards was used for calibration.

A SEM TESCAN VEGA 3XM instrument at the Institute of Geology, Academy of Sciences of the Czech Republic, has been used to document surface features of the natural alabandite (NA sample). To avoid potential deterioration of the sample, the specimen has not been coated and the SEM has been operated at low-vacuum mode. Energy-dispersive X-ray (EDX) spectra of individual phases observed on the surface of the studied specimen have been acquired with a Bruker XFlash detector. Subsequently, a part of the sample has been polished and analyzed with an electron microprobe (EMPA) CAMECA SX-100 instrument at the Institute of Geology, Academy of Sciences of the Czech Republic, to determine the stoichiometry of the sample interior.

Results and discussion

Characterization and low-temperature magnetic properties of α-MnS

XRD patterns of a natural alabandite (NA) and of two synthetic α-MnS (SA1 and SA2) samples are shown in Figures 1a, 1b, and 1c. They perfectly correspond to the cubic structure of α-MnS (PDF No. 01-088-2223). In the NA sample, some amount of elemental sulfur (16% by Rietveld refinement) and hausmannite (see below) has been found in addition to the alabandite main phase. The presence of sulfur on the NA sample surface was also confirmed by SEM/EDX (Fig. S1 of the auxiliary material). In

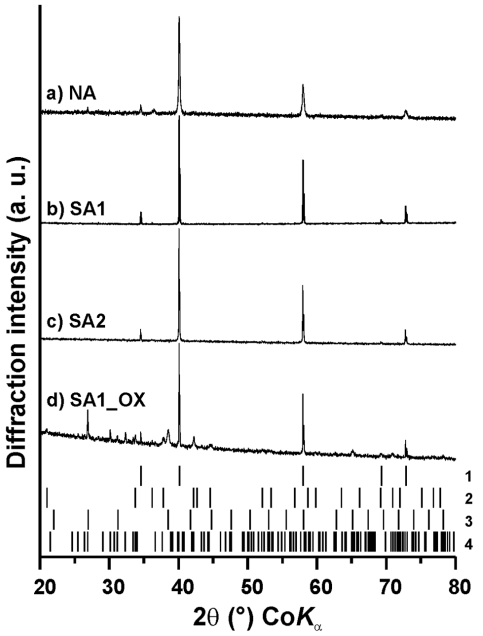

Figure 1. XRD patterns of the samples: (**a**) NA, (**b**) SA1, (**c**) SA2, and (**d**) SA1_OX. Phase fractions derived from a Rietveld refinement of the SA1_OX sample are: 24.0(2) wt% of MnS, 23(1) wt% of Mn_3O_4, 22.9(4) wt% of Mn_2O_3, and 30(1) wt% of sulfur. The respective PDF cards shown below XRD patterns are: 1 = 01-088-2223 (MnS); 2 = 01-075-1560 (Mn_3O_4); 3 = 01-089-4836 (Mn_2O_3); 4 = 01-078-1888 (S).

[1] Deposit item AM-13-801, supplemental data and figure. Deposit items are available two ways: For a paper copy contact the Business Office of the Mineralogical Society of America (see inside front cover of recent issue) for price information. For an electronic copy visit the MSA web site at http://www.minsocam.org, go to the American Mineralogist Contents, find the table of contents for the specific volume/issue wanted, and then click on the deposit link there.

Table 1. Alabandite samples

Sample	Description of sample preparation	Stoichiometry of alabandite	Stoichiometry by means of
NA	natural alabandite	$Mn_{1.007}S$	EMPA on polished speciment
SA1	solvothermal process	n.d.	
SA2	direct thermal synthesis from S and Mn powders	$MnS_{0.998}S$	SEM/ WDS on polished speciment
SA1_OX	oxidation product of sample SA1	n.d.	

Note: n.d. stands for not determined values.

contrast, EMPA of the NA sample interior did not reveal any presence of sulfur or hausmannite. A SEM-WDS analysis of the SA2 sample shows a similar result. Based on the information provided above, all three studied samples can be considered as being representative of alabandite with only a minor presence of other phases limited to the surface of the individual grains.

Temperature dependence of induced FC and ZFC magnetizations at 10 mT (Fig. 2) as well as remanent FC and ZFC magnetizations (imprinted by 2.5 T at 5 K; Fig. 3) yield Néel temperatures (T_N) for natural and synthetic samples in a narrow temperature range around 153 K as expected for alabandite (Pearce et al. 2006). The Néel temperature manifests itself through peaks on the induced magnetization curves, and through merging of the FC and ZFC remanent magnetization curves at T_N.

In all alabandite samples, a feature at 40 ± 2 K is further observed, manifested through a rapid increase of the magnetic response with decreasing temperature (Figs. 2 and 3). An enhanced magnetic response is also seen in the hysteresis properties at 5 K, namely, an S-shaped hysteresis loop and a tendency to saturation in a high external magnetic field (Fig. 4). Such a behavior is typical for ferro/ferrimagnetic materials rather than for an antiferromagnetic one.

An enhanced magnetic response below 40 ± 2 K is similar to that reported for iron-free α-MnS samples slightly enriched in Mn with respect to a stoichiometric α-MnS and interpreted as an antiferro- to ferromagnetic transition at 40 K upon cooling (Petrakovski et al. 2001). However, in our case both NA and SA2 samples are highly stoichiometric examples of alabandite (Table 1). According to our measurements, the enhanced magnetic response at around 40 K occurs in all studied samples and its amplitude does not correlate with Mn/S ratio. Thus, a question arises whether such low-temperature behavior is limited to alabandite samples slightly enriched in Mn as reported by Petrakovski et al. (2001), or it is a general phenomenon occurring in stoichiometric or Mn-depleted alabandite samples as well. Alternatively, a presence of small amounts of another phase on alabandite grain surfaces identified above may be responsible for the observed low-temperature magnetic behavior and will be evaluated in following section.

Effects of surface oxidation on low-temperature magnetic properties of α-MnS

To confirm or exclude the role of manganese oxides on the magnetic response of α-MnS (sulfur should not significantly influence the low-temperature magnetic properties of alabandite), we artificially oxidized the SA1 sample by hydrogen peroxide (H_2O_2). About 20 mg of SA1 material was briefly submerged in hydrogen peroxide and air-dried at room temperature for 20 h (sample labeled as SA1_OX). Subsequently, XRD and magnetic measurements were carried out following the same procedures as for other samples (Figs. 1d and 5).

Upon hydrogen peroxide treatment, the surface of MnS was partially oxidized into a manganese oxide phases and thus the ratio of alabandite to manganese oxides in the SA1_OX sample changed compared to the original SA1 sample. The presence of manganese oxide Mn_3O_4, known also as the mineral hausmannite, was confirmed by XRD analysis in the SA1_OX sample (Fig. 1d). Hausmannite has a Curie temperature T_C of ~41–43 K (Dwight

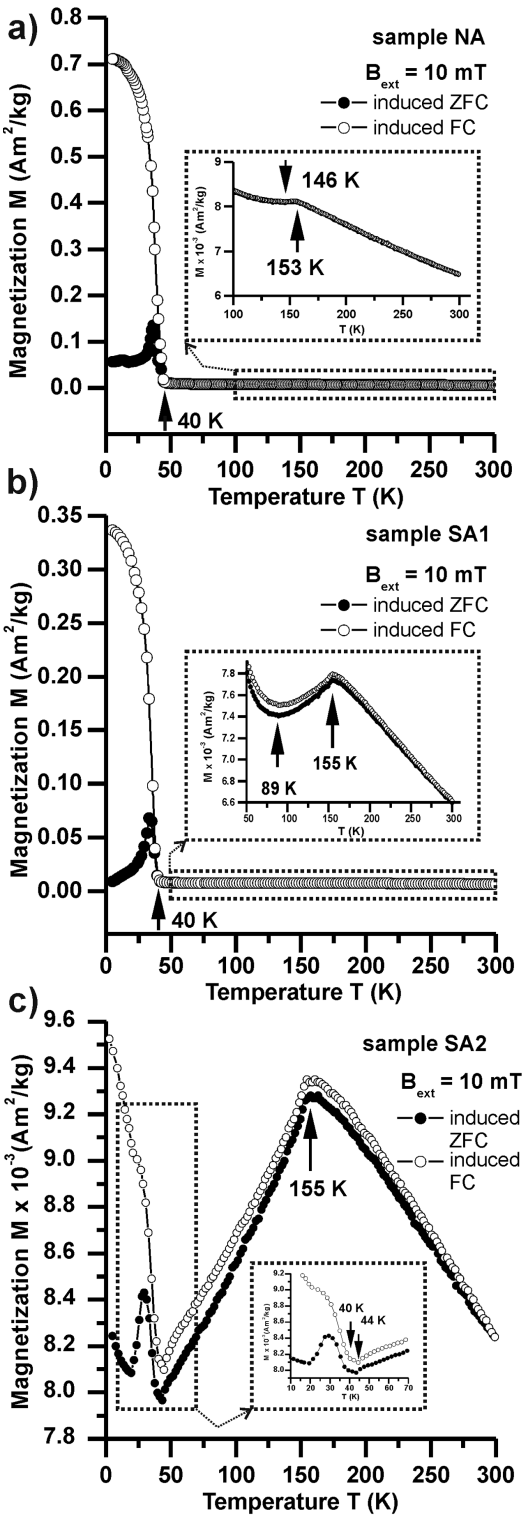

FIGURE 2. Induced ZFC and FC magnetization curves in an external magnetic field of 10 mT for samples: (**a**) NA, (**b**) SA1, and (**c**) SA2.

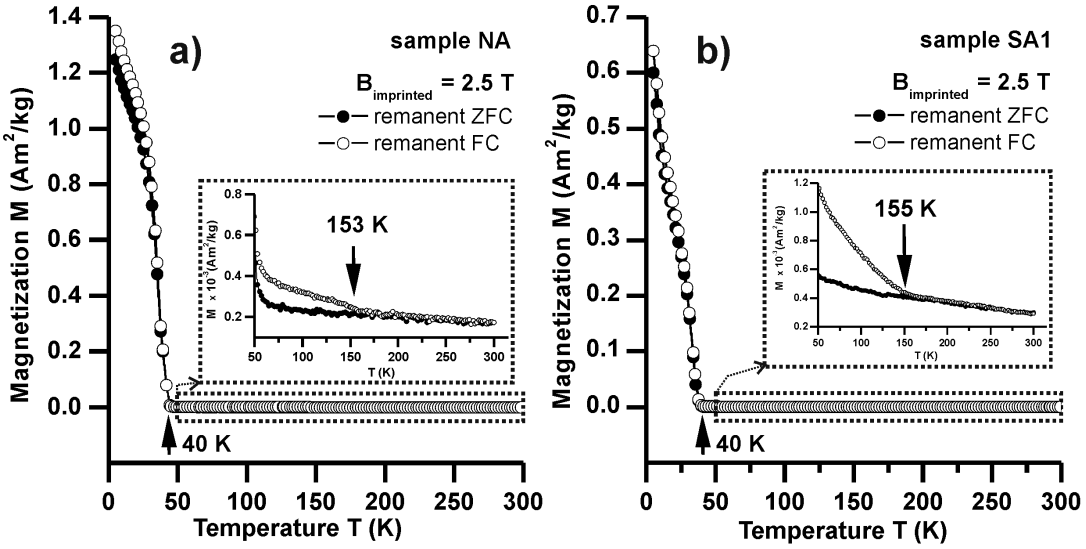

FIGURE 3. ZFC-FC curves of remanent magnetization imprinted by a field of 2.5 T for samples: (**a**) NA and (**b**) SA1.

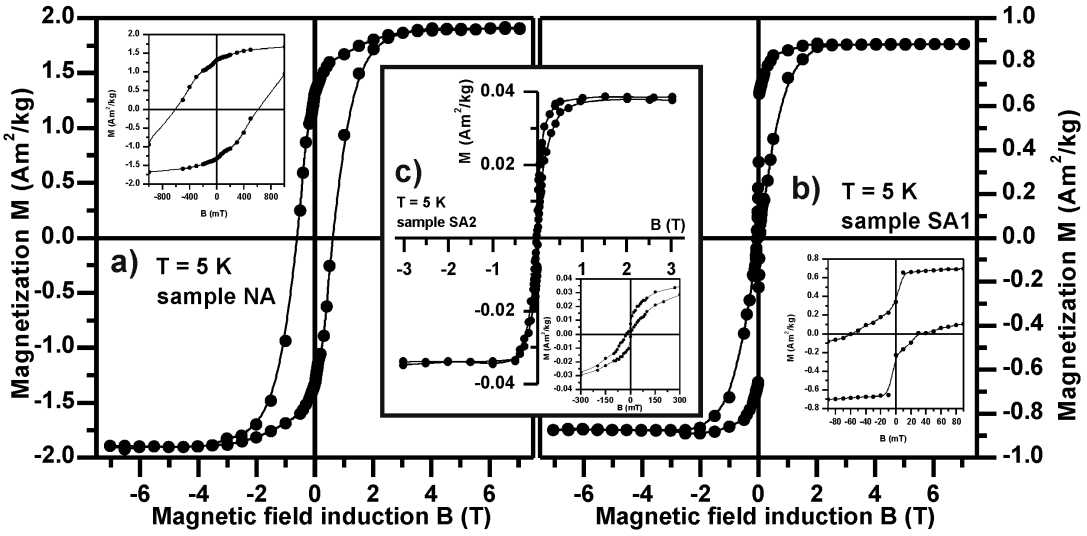

FIGURE 4. Hysteresis loops of samples: (**a**) NA, (**b**) SA1, and (**c**) SA2, measured at 5 K (the high-field slope has been subtracted).

and Menyuk 1960; Robie and Hemingway 1985). It is very close to the temperature where an enhanced magnetic response of alabandite is observed upon cooling, making hausmannite a meaningful candidate to explain the observed low-temperature magnetic behavior of alabandite. Other phases identified in the XRD pattern are bixbyite [α-Mn_2O_3, antiferromagnetic below 80 K (Robie and Hemingway 1985) or 90 K (Mukherjee et al. 2006)] and sulfur [diamagnetic (O'Handley 2000; Blundell 2001)]. These phases do not have any magnetic transitions around 40 K, which would explain the observed magnetic behavior at this temperature.

The oxidized SA1_OX sample shows a significant increase (by a factor of eight) in its magnetic response below 40 ± 2 K compared to the unoxidized α-MnS sample (insets in Fig. 5). The dependence of the magnitude of the 40 K magnetic response on the amount of manganese oxides, including hausmannite, suggests that the low-temperature behavior observed in studied alabandite samples is not an intrinsic property of alabandite itself, but rather hausmannite governs the low-temperature magnetic response below ~40 K. A similar example was described for antiferromagnetic MnO nanoparticles with Mn_3O_4 surface layers (Berkowitz et al. 2008).

Assuming that ferromagnetic-like hysteresis loops measured at 5 K are produced entirely by Mn_3O_4, it is possible to estimate its content in the studied samples. However, caution is needed

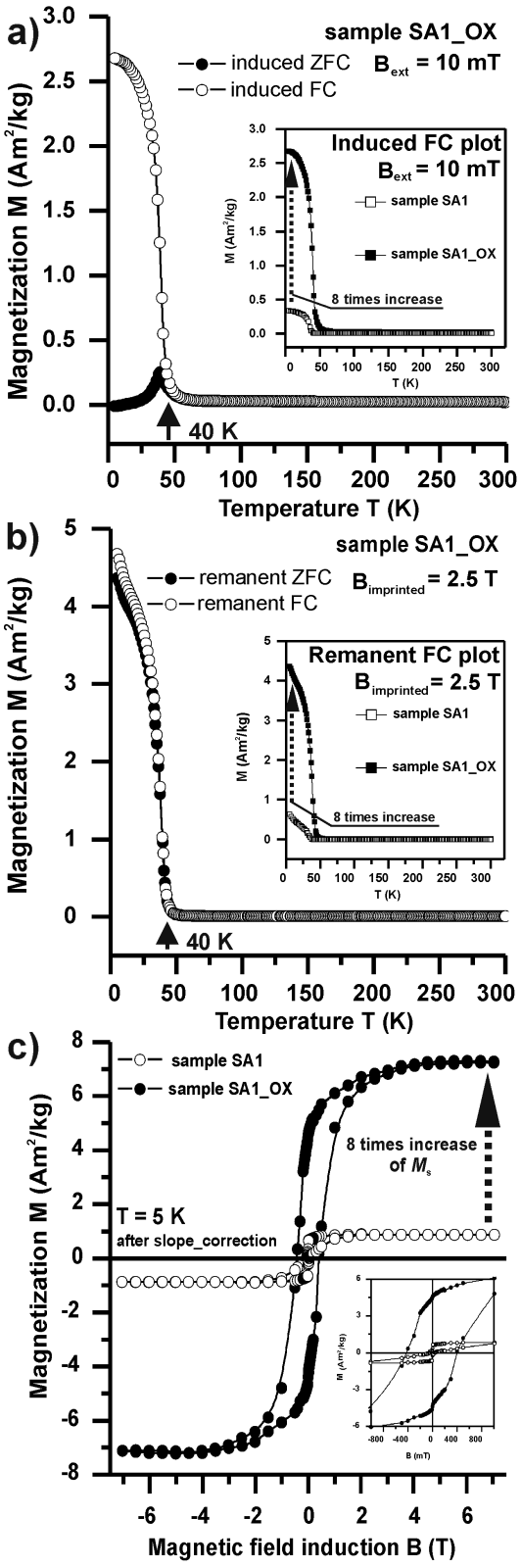

when interpreting the hysteresis data, since, unlike many other compounds of spinel type, Mn_3O_4 does not reach magnetic saturation even in fields as high as 34 T (Nielsen and Roeland 1976). A corresponding saturation magnetization value, determined from extrapolation to zero magnetic field of the magnetization field dependence measured along the [010] direction, amounts to 47.2 Am^2/kg. Experiments performed in much lower maximum fields, which are more appropriate to compare with ours, yielded respectively lower values of the high-field magnetization extrapolated to zero field (M_E): 34.2 Am^2/kg (1.4 Bohr magnetons per formula unit) for the 1 T field (Wickham and Croft 1958) and 38.1 Am^2/kg (1.56 Bohr magnetons per formula unit) for the 14 T field (Jacobs 1959).

For our experiments, carried out in a maximum field of 7 T, we adopted an intermediate value of 36 Am^2/kg. The M_E of the SA1_OX sample (i.e., after oxidation) amounts to 7.3 Am^2/kg at 5 K (Table 2) corresponding to a presence of ~20 wt% of hausmannite. This is in a reasonably good agreement with the result of a Rietveld refinement where the amount of hausmannite in this oxidized sample appears to be 22.9(4) wt%. The remaining difference may be due to a small size of at least a fraction of hausmannite grains as suggested by broad diffraction peaks of hausmannite in the XRD pattern (Fig. 1d; see also Siskova et al. 2012 and Markova et al. 2012). Indeed, nanosized Mn_3O_4 shows considerably reduced M_E values as determined from hysteresis loops measured in maximum fields up to 7 T (Winkler et al. 2004; Vázquez-Olmos et al. 2005).

We expect that hausmannite governs the magnetic response below 40 K in other studied samples as well. Comparing, as above, the M_E values at 5 K (Table 2) with the Mn_3O_4 M_E bulk value of 36 Am^2/kg, we can estimate the hausmannite content. Approximately 2.4, 0.1, and 5.3 wt% of hausmannite are required to produce the low-temperature magnetic response observed in SA1 (before oxidation), SA2, and natural alabandite (NA) samples, respectively. These values are close to, or below, the detection limit of XRD measurements and thus not observed in the XRD pattern of these samples except for NA sample [6.9(4) wt% of Mn_3O_4 as obtained by Rietveld refinement].

Furthermore, a profile of the temperature-dependent induced FC magnetization curve of samples NA, SA1, and especially SA1_OX displays a tendency to follow the Curie-Weiss law above 40 K. The hysteresis loops below 40 K show also shift along the field (horizontal) axis toward negative values (compare B_{C+} and B_{C-} in Table 2), which seems to be a manifestation of the exchange interaction between antiferromagnetic and ferro- or ferrimagnetic phases (Nogues and Schuller 1999). An exchange bias or exchange anisotropy is present in bi-layers (or multi-layers) of magnetic materials, which in our case are represented by alabandite (antiferromagentic) and hausmannite (ferrimagentic). On the

◀**FIGURE 5.** (**a**) Induced ZFC and FC magnetization curves in an external magnetic field of 10 mT for the SA1_OX sample. Induced FC curves of SA1 before and after oxidation are displayed for comparison in the inset. (**b**) ZFC-FC curves of remanent magnetization imprinted by a field of 2.5 T for the SA1_OX sample. Remanent-FC curves of SA1 before and after oxidation are displayed for comparison in the inset. (**d**) Hysteresis loops of the SA1 sample before and after oxidation at 5 K after slope correction.

TABLE 2. Parameters of the hysteresis loops of samples NA, SA1, SA2, and SA1_OX at 5 K after the high-field slope has been subtracted

Sample	T (K)	M_{E+} (Am^2/kg)	M_{E-} (Am^2/kg)	B_{C+} (mT)	B_{C-} (mT)	M_{R+} (Am^2/kg)	M_{R-} (Am^2/kg)
NA	5	1.910 ± 0.001	1.905 ± 0.001	424 ± 1	−608 ± 1	1.315 ± 0.001	−1.326 ± 0.001
SA1	5	0.882 ± 0.001	−0.874 ± 0.001	29 ± 1	−59 ± 1	0.344 ± 0.001	−0.225 ± 0.001
SA2	5	0.039 ± 0.001	−0.035 ± 0.001	4 ± 1	−24 ± 1	0.008 ± 0.001	−0.002 ± 0.001
SA1_OX	5	7.277 ± 0.001	7.235 ± 0.001	395 ± 1	−426 ± 1	4.564 ± 0.001	−4.376 ± 0.001

Notes: M_{E+} is the positive saturation magnetization, M_{E-} is the negative saturation magnetization, B_{C+} is the positive coercivity, B_{C-} is the negative coercivity, M_{R+} is the positive remanent magnetization, and M_{R-} is the negative remanent magnetization.

other hand, we cannot exclude a random canting of the particle surface spins caused by competing antiferromagnetic exchange interactions at the surface of hausmannite particles producing an exchange anisotropy between their core and surface spins.

In the SA2 sample with an extremely low (~0.1%) hausmannite content, the magnetic signal above 40 K does not show a tendency to follow the Curie-Weiss law, and the low-temperature behavior is dominated by a stronger alabandite antiferromagnetic response than a paramagnetic behavior of Mn_3O_4 present in the oxidized surface layer of alabandite grains.

Upon heating in the temperature range between T_C of hausmannite and T_N of alabandite, the decreasing paramagnetic response of hausmannite overlaps with the slightly increasing antiferromagnetic response of alabandite. A local minimum in the induced FC curve can be observed in this temperature range and it is shifted to the higher temperatures with increasing hausmannite content (insets in Fig. 2). In this case, it appears that there is a direct correlation between the amount of hausmannite present in the sample and temperature at which the minimum occurs. The estimated temperatures are 44 ± 1, 89 ± 1, and 146 ± 1 K for SA2, SA1, and NA samples, respectively, and follow positive trends with increasing hausmannite content. For SA1_OX sample, we do not observe the minimum in temperature range from 40 to 155 K because the paramagnetic response of hausmannite (and perhaps also of bixbyite) dominates over the antiferromagnetic response of α-MnS.

Last but not least, the temperature dependence of induced ZFC measurements of NA, SA1, SA2, and SA1_OX samples exhibits a sharp peak below the Curie temperature ascribed to hausmannite, and then on subsequent heating drops down to a very low values (Figs. 2 and 5a). The observed peak can be interpreted as a Hopkinson peak observed just prior to the transition from a magnetically ordered state to a paramagnetic one (Dunlop and Özdemir 1997) rather than as an effect accompanying a magnetic transition from a ferromagnetic to an antiferromagnetic state as suggested by Petrakovski et al. (2001).

The positive correlation between Mn enrichment and the magnitude of the 40 K feature observed in synthetic alabandite by Petrakovski et al. (2001) can be explained as the extra Mn added that did not enter the alabandite structure and rather reacted with oxygen to produce manganese oxides including hausmannite. Thus, a higher addition of Mn resulted in a higher production of hausmannite causing a higher amplitude of the 40 K feature.

Comparison to other low-temperature magnetic minerals

A similar low-temperature magnetic transition, as described above in the alabandite-hausmannite system, is observed at ~70 K in the other monosulfide-troilite FeS (Kohout et al. 2007; Cuda et al. 2011). Gattacceca et al. (2011) recently reported that chromite with Curie temperature in 40–80 K range exists in certain meteorites and chromite contamination within troilite samples may be responsible for the observed ~70 K feature in troilite. In this respect alabandite with hausmanite contamination is analogous to troilite with a proposed chromite contamination. Thus, in the following paragraph we briefly compare the alabandite-hausmannite system to the troilite and chromite.

At the first look both systems show a very similar behavior with a sharp increase in both induced and remanent magnetization and an onset of a ferromagnetic-like hysteresis below the transition temperature. The difference between these two systems is in the nature of the contaminant. Hausmannite is of similar composition to alabandite (both manganese-bearing phases) and is localized at the surface of alabandite grains. Thus it can be easily overlooked in EMPA analysis of polished grains. In contrast, a chromite contamination is supposed to be present within the interior of troilite grains and thus should be more easily observable. Thorough analytical data [EMPA and SEM-BSE observation of polished grain sections, atomic absorption spectroscopy, XRD, and Mössbauer spectroscopy of bulk troilite samples in Cuda et al. (2011)] reveals a chromium content of one to three orders of magnitude lower than as predicted for a chromite amount compatible with low-temperature magnetic observations. Another difference can be observed on induced ZFC magnetization curves. While in the alabandite-hausmannite case the ZFC induced magnetization stays well below FC and shows a pronounced Hopkinson peak just below T_C of hausmannite (Fig. 2), the ZFC curve of troilite does not show obvious presence of a Hopkinson peak [Fig. 3 in Kohout et al. (2007)]. Thus, the nature of the contaminant or mechanism of the low-temperature transition in troilite is likely to be different than as proposed for chromite (or similar to alabandite-hausmannite case).

CONCLUDING REMARKS

Based on our detailed investigation, the low-temperature phenomenon at ~40 K, previously observed in some synthetic alabandite samples and ascribed to nonstoichiometry of the latter, is not an intrinsic property of alabandite. It appears to be a result of a ferri- to paramagnetic transition of hausmannite (Mn_3O_4) present in an oxidized surface layer on crystals/grains of alabandite. The presence of hausmannite even in amounts below 1 wt% can have a detectable effect on the magnetic response of alabandite, which is otherwise a purely antiferromagnetic material below its Néel temperature of ~153 K without any other low-temperature magnetic transitions. This conclusion rules out pristine alabandite to significantly contribute to remanent or induced magnetism of minor Solar System bodies. In contrary, no prove of similar contamination has been found in troilite showing a similar transition at ~70 K.

Acknowledgments

The authors gratefully acknowledge the support by the Grant Agency of the Academy of Sciences of the Czech Republic (KJB300130903), Institute of Geology ASCR, v.v.i., research project (RVO67985831), Czech Science Foundation (GACR P108/11/1350), the internal grant of Palacký University in Olomouc, Czech Republic (PrF_2013_014) and the Operational Program Research and Development for Innovations-European Regional Development Fund (CZ.1.05/2.1.00/03.0058 of the Ministry of Education, Youth and Sports of the Czech Republic), and by a Visiting Fellowship at the Institute for Rock Magnetism, which is funded by the Instruments and Facilities program of the National Science Foundation. We also thank Vlasta Böhmová and Zuzana Korbelová for their assistance with SEM/EDX, EPMA analyses and Zdenka Marková for her assistance with MnS sample preparation.

References cited

Anthony, J.W., Bideaux, R.A., Bladh, K.W., and Nichols M.C. (2102) Handbook of Mineralogy. Mineralogical Society of America, Chantilly, Virginia, http://www.handbookofmineralogy.org/ (viewed Jan.13.2012).

Berkowitz, A.E., Rodriguez, G.F., Hong, J.I., An, K., Hyeon, T., Agarwal, N., Smith D.J., and Fullerton E.E. (2008) Antiferromagnetic MnO nanoparticles with ferrimagnetic Mn_3O_4 shells: Doubly inverted core-shell system. Physical Review B, 77, 024403.

Biswas, S., Kar, S., and Chaudhuri, S., (2007) Growth of different morphological features of micro and nanocrystalline manganese sulfide via solvothermal process. Journal of Crystal Growth, 299, 94–102.

Blundell, S. (2001) Magnetism in Condensed Matter. Oxford University Press, New York.

Brearley, A.J., and Jones, R.H. (1998) Chondritic meteorites. In J.J. Papike, Ed., Planetary Materials, 36, p. 3–264. Reviews in Mineralogy, Mineralogical Society of America, Chantilly, Virginia.

Cuda, J., Zboril, R., Schneeweiss, O., Tucek, J., Prochazka, V., Maslan, M., and Tucek, P. (2010) Mössbauer study and macroscopic/global magnetic behavior of powdered ilmenite ($FeTiO_3$) sample. In J. Tucek and M. Miglierini, Eds., Mössbauer Spectroscopy in Materials Science: 2010, AIP Conference Proceedings, vol. 1258, pp. 55–67. American Institute of Physics, Melville, New York.

Cuda, J., Kohout, T., Tucek, J., Haloda, J., Filip, J., Prucek, R., and Zboril, R. (2011) Low-temperature magnetic transition in troilite: A simple marker for highly stoichiometric FeS systems. Journal of Geophysical Research, 116, B11205.

Doelter, C. (1926) Handbuch der Mineralchemie, 4, 485. Verlag von Theodor Steinkopff, Dresden.

Dunlop, D.J., and Özdemir, Ö. (1997) Rock Magnetism Fundamentals and Frontiers. Cambridge University Press, U.K.

Dwight, K., and Menyuk, N. (1960) Magnetic properties of Mn_3O_4 and the canted spin problem. Physical Review, 119, 1470–1479.

Fioretti, A.M., and Molin, G. (1998) Alabandite in ureilite Frontier Mountain 95028. Meteoritics and Planetary Science, 33, A46–47.

Gattacceca, J., Rochette, P., Lagroix F., Mathé, P.E., and Zanda, B. (2011) Low temperature magnetic transition of chromite in ordinary chromites. Geophysical Research Letters, 38, L10203.

Heikens, H.H., Wiegers, G.A., and Van Bruggen, C.F. (1977) On the nature of a new phase transition in α-MnS. Solid State Communications, 24, 205–209.

Hewett, D.F., and Rove, O.N. (1930) Occurrence and relations of alabandite. Economic Geology, 25, 36–56.

Jacobs, I.S. (1959) Evidence for triangular moment arrangements in $MO \cdot Mn_2O_3$. Journal of Physics and Chemistry of Solids, 11, 1–11.

Keil, K. (1968) Mineralogical and chemical relationships among enstatite chondrites. Journal of Geophysical Research, 73, 6945–6976.

Keil, K., and Fredriksson, K. (1967) Electron microprobe analysis of some rare minerals in the Norton County achondrite. Geochimica et Cosmochimica Acta, 27, 939–942.

Kohout, T., Kosterov, A., Jackson, M., Pesonen, L.J., Kletetschka, G., and Lehtinen, M. (2007) Low-temperature magnetic properties of the Neuschwanstein EL6 meteorite. Earth and Planetary Science Letters, 261, 143–151.

Kohout, T., Kosterov, A., Haloda, J., Týcová, P., and Zbořil, R. (2010) Low temperature magnetic properties of iron bearing sulfides and their contribution to magnetism of cometary bodies. Icarus, 208, 955–962.

Lepland, A., and Stevens, R.L. (1998) Manganese authigenesis in the Landsort Deep, Baltic Sea. Marine geology, 151, 1–25.

Lin, Y.T., El Goresy, A., and Hutcheon, I.D. (1989) The first meteoritic silver minerals in Pena Blanca Springs Enstatite Achondrite: Assemblages, Compositions and silver isotopes. Twentieth Lunar and Planetary Science Conference (1989), Abstract no. 1291.

Loseva, G.V., Ryabinkina, L.I., and Balaev, A.D. (1998) Ferromagnetism and the metal-insulator transition in the magnetic semiconductor system $Fe_xMn_{1-x}S$. Physics of the Solid State, 40, 250–251 (Translated from Fizika Tverdogo Tela 40, 276–277).

Markova, Z., Šišková, K., Filip, J., Šafářová, K., Prucek, R., Panáček, A., Kolář, M., and Zbořil, R. (2012) Chitosan-based synthesis of magnetically-driven nanocomposites with biogenic magnetite core, controlled silver size, and high-antimicrobial activity. Green Chemistry, 14, 2550–2558.

Mason, B., and Jarosewich, E. (1967) The Winona meteorite. Geochimica et Cosmochimica Acta, 31, 1097–1099.

Mittlefehldt, D.W., McCoy, T.J., Goodrich, C.A., and Kracher A. (1998) Non-chondritic meteorites from asteroidal bodies. In J. J. Papike, Ed., Planetary Materials, 36, p. 4–99. Reviews in Mineralogy, Mineralogical Society of America, Chantilly, Virginia.

Mukherjee, S., Pal, A.K., Bhattacharya, S., and Raittila, J. (2006) Magnetism of Mn_2O_3 nanocrystals dispersed in a silica matrix: Size effects and phase transformations. Physical Review B, 74, 104413.

Nielsen, O.V., and Roeland, L.W. (1976) High-field magnetization for Mn_3O_4 single crystals. Journal of Physics C: Solid State Physics, 9, 1307–1311.

Nogues, J., and Schuller J.K. (1999) Exchange bias. Journal of Magnetism and Magnetic Materials, 192, 203–232.

O'Handley, R.C. (2000) Modern Magnetic Materials Principles and Applications. Wiley, New York.

Pearce, C.I., Pattrick, R.A.D., and Vaughan, D.J. (2006) Electrical and magnetic properties of sulfides. In D.J. Vaughan, Ed., Sulfide Mineralogy and Geochemistry, 61, p. 127–180. Reviews in Mineralogy and Geochemistry, Mineralogical Society of America, Chantilly, Virginia.

Petrakovski, G.A., Ryabinkina, L.I., Abramova, G.M., Velikanov, D.A., and Bovina, A.F. (2001) Antiferromagnet–ferromagnet transition in α-Mn_xS manganese sulfides. Physics of the Solid State, 43, 493–495 (Translated from Fizika Tverdogo Tela 43, 474–476).

Petrakovski, G.A., Ryabinkina, L.I., Abramova, G.M., Balaev, A.D., Romanova, O.B., and Makovetski, G.I. (2002) Magnetic properties of $Fe_xMn_{1-x}S$ sulfides exhibiting the magnetoresistive effect. Physics of the Solid State, 44, 1925–1928 (Translated from Fizika Tverdogo Tela 44, 1836–1839).

Robie, R.A., and Hemingway, B.S. (1985) Low-temperature molar heat capacities and entropies of MnO_2 (pyrolusite), Mn_3O_4 (hausmannite), and Mn_2O_3 (bixbyite). The Journal of Chemical Thermodynamics, 17, 165–181.

Ryder, G., and Murali, A.V. (1987) Mineralogy and chemistry of antarctic aubrites. Meteoritics, 22, 495–496.

Siskova, K., Tucek, J., Machala, L., Otyepkova, E., Filip, J., Safarova, K., Pechousek, J., and Zboril, R. (2012) Air-stable nZVI formation mediated by glutamic acid: Solid-state storable material exhibiting 2D chain morphology and high reactivity in aqueous environment. Journal of Nanoparticle Research, 14, 805.

Vázquez-Olmos, A., Redón, R., Mata-Zamora, M.E., Morales-Leal, F., Fernández-Osorio, A.L., and Saniger, J.M. (2005) Structural and magnetic study of Mn_3O_4 nanoparticles. Reviews on Advanced Materials Science, 10, 362–366.

Wickham, D.G., and Croft, W.J. (1958) Crystallographic and magnetic properties of several spinels containing trivalent manganese. Journal of Physics and Chemistry of Solids, 7, 351–360.

Winkler, E., Zysler, R.D., and Fiorani, D. (2004) Surface and magnetic interaction effects in Mn_3O_4 nanoparticles. Physical Review B, 70, 174406–174405.

Zhang, Y., and Sears, D.W.G. (1996) The thermometry of enstatite chondrites: A brief review and update. Meteoritics, 31, 647–655.

Zhang, Y., Benoit, P.H., and Sears, D.W.G. (1995) The classification and complex thermal history of the enstatite chondrites. Journal of Geophysical Research, 100, 9417–9438.

Manuscript received September 12, 2012
Manuscript accepted March 28, 2013
Manuscript handled by Lars Ehm

Příloha E

Kohout, T., Čuda, J., Filip, J., Bradley, T., Britt, D., Tuček, J., Skála, R., Kletetschka, G., Kašlík, J., Malina, O., Šišková, K., Zbořil, R.:

Space weathering simulations through controlled growth of iron nanoparticles on olivine surface

přijato v časopise *Icarus* (9. 4. 2014)

Space weathering simulations through controlled growth of iron nanoparticles on olivine

T. Kohout[1,2], J. Čuda[3], J. Filip[3], D. Britt[4], T. Bradley[4], J. Tuček[3], R. Skála[1], G. Kletetschka[1,5], J. Kašlík[3], O. Malina[3], K. Šišková[3], and R. Zbořil[3]

1. Institute of Geology, Academy of Sciences of the Czech Republic, Prague, Czech Republic
2. Department of Physics, University of Helsinki, Finland
3. Regional Centre of Advanced Technologies and Materials, Faculty of Science, Departments of Experimental Physics and Physical Chemistry, Palacký University, Olomouc, Czech Republic
4. Department of Physics, University of Central Florida, Orlando, USA
5. Faculty of Science, Charles University in Prague, Czech Republic

Abstract

Airless planetary bodies are directly exposed to space weathering. The main spectral effects of space weathering are darkening, reduction in intensity of silicate mineral absorption bands, and an increase in the spectral slope towards longer wavelengths (reddening). Production of nanophase metallic iron ($npFe^0$) during space weathering plays major role in these spectral changes. A laboratory procedure for the controlled production of $npFe^0$ in silicate mineral powders has been developed. The method is based on a two-step thermal treatment of low-iron olivine, first in ambient air and then in hydrogen atmosphere. Through this process, a series of olivine powder samples was prepared with varying amounts of $npFe^0$ in the 7-20 nm size range. A logarithmic trend is observed between amount of

npFe^0 and darkening, reduction of 1 µm olivine absorption band, reddening, and 1 µm band width. Olivine with a population of physically larger npFe^0 particles follows spectral trends similar to other samples, except for the reddening trend. This is interpreted as the larger, ~40-50 nm sized, npFe^0 particles do not contribute to the spectral slope change as efficiently as the smaller npFe^0 fraction. A linear trend is observed between the amount of npFe^0 and 1 µm band center position, most likely caused by Fe^{2+} disassociation from olivine structure into npFe^0 particles.

Introduction

Airless planetary bodies are directly exposed to the space environment and thus to space weathering. Space weathering is caused by a combination of solar wind and solar radiation, micrometeorite bombardment, and cosmic radiation that can alter the physical, chemical, and crystallographic properties of airless regoliths. Among other effects, space weathering causes changes in the visible, IR and UV spectra of exposed surface material making it difficult to compare weathered asteroidal and lunar spectra to those of unweathered silicate minerals, meteorites, and lunar samples.

Lunar type space weathering

Lunar samples delivered to Earth by the Apollo program during the 1960's and 1970's significantly contributed to our understanding of space weathering. It was the first time that direct laboratory studies were possible on a material exposed for long periods to the space environment and, therefore, modified by space weathering. Numerous early studies (e.g. Adams and Jones, 1970, McCord and Johnson, 1970, Adams and McCord, 1971, 1973, and McCord and Adams, 1973) found that, compared to artificially crushed fresh Apollo rock samples, spectra of lunar soils are darker, have

reduced intensity of silicate mineral absorption bands, and their spectral slope increases towards longer wavelengths (reddening).

Reviews by Hapke (2001) or Chapman (2004) provide an understanding of the mechanisms involved in space weathering. Earlier lunar soil studies indicated that space weathering may cause an accumulation of dark agglutinitic glass formed by surface melting of regolith by micrometeorite impacts (Adams and McCord, 1970). Agglutinitic glass is an important optical agent influencing reflectance spectra of lunar regolith. However, its presence could not explain all of the spectral discrepancies in lunar soils and planetary surfaces, especially the spectral reddening (Pieters et al., 1993). Hapke et al. (1975) suggested that optical effects of space weathering may be caused by metallic submicroscopic iron particles (SMFe), also referred to as nanophase iron ($npFe^0$) particles, within the vapor deposition rims on lunar soil grains. This $npFe^0$ is believed to originate from disassociation of Fe from Fe-bearing minerals through solar wind sputtering and micro-impact-generated vapor (e.g. Keller and McKay, 1993; 1997, Hapke, 2001), and its concentration is highest in the fine fraction of lunar soils (Pieters et al, 1993; Taylor et al., 2001). Support for this theory came later from transmission electron microscopy (TEM). TEM observations showed the presence of such $npFe^0$ particles in lunar soil grain coatings (e.g. Keller and McKay, 1997; Hapke, 2001). The typical size range of $npFe^0$ particles is ~1-10 nm in vapor deposition rims and ~10-100 nm in agglutinates (e.g. Keller and Clemett, 2001).

S-type asteroid space weathering

As in the case of lunar rocks, spectral discrepancies are also observed between meteorites and asteroids (e.g. Hapke, 2001 and Chapman, 2004). Silicate rich S-complex asteroids are represented by

absorption bands characteristic of olivine (at wavelengths around 1 μm) and pyroxene (at wavelengths around 1 and 2 μm). Spectra of ordinary chondrite meteorites contain similar absorption bands, but, compared to asteroids, the bands in meteorites are usually more intense and the overall spectral slope is flatter. Numerous laboratory simulations (involving laser irradiation and ion bombardment, e.g. Brunetto et al., 2005) of ordinary chondrites and detailed spectral observations of asteroids and meteorites (e.g. Marchi et al., 2005; Lazzarin et al., 2006) show that space weathering effects on chondritic materials and S-complex asteroids display similarities to lunar soils where solar wind ion bombardment induces atom displacements and micrometeorite bombardment forms $npFe^0$ particles. Direct evidence of $npFe^0$ particle formation on the surface of S-type asteroids was recently reported by Noguchi et al. (2011) in a study of surface coatings of regolith grains obtained from asteroid 25143 Itokawa by the Hayabusa sample return mission. However, compared to lunar weathering, the mechanism of asteroidal space weathering is more complex and its various effects (e.g. absorption band weakening, darkening, and reddening) do occur in spectra, with a highly varying intensity, even on the same asteroids (e.g. Chapman, 2004; Hiroi et al., 2006; Gaffey, 2010).

Observations of young asteroid families shows that space weathering occurs relatively rapidly, within 10^6 years after the breakup of the parent body (Vernazza et al., 2009). Similar to lunar type weathering, space weathering on asteroids affects a thin surface regolith layer only and this layer can be disturbed by geological processes such as landslides, as observed on Eros by Clark et al. (2001), or by tidal forces during close planetary encounters (Binzel et al., 2010).

Space weathering laboratory simulations

Laboratory production of $npFe^0$ particles similar to those observed in space-weathered lunar soils was achieved by direct mineral or glass reduction (Allen et al., 1993) short duration laser irradiation (e.g. Sasaki et al., 2001; 2002; 2003; Brunetto et al., 2005; Lazzarin et al., 2006; Markley et al., 2013), ion bombardment (e.g. Marchi et al.; 2005, Lazzarin et al.; 2006), direct mineral / glass synthesis (Liu et al, 2007), or microwave irradiation (Tang et al., 2012) on various silicate minerals, meteorites or lunar rocks. Since then, laser irradiation together with ion bombardment has become a common laboratory tool for space weathering simulation, capable of reproducing most spectral changes. However, these methods do not provide sufficient control over $npFe^0$ particle size and concentration and, thus, do not enable quantitative space weathering simulations.

Only a handful of studies were devoted to control the size and quantity of $npFe^0$ and to verify its effect on spectral properties. For example, Allen et al. (1996) produced 6 nm sized $npFe^0$ particles on a silica gel substrate with 6 nm pores through impregnating the pores with ferric nitrate solution and subsequent reduction of iron in a hydrogen atmosphere. Noble et al. (2007) enhanced this technique with silica gel substrates featuring pore sizes of 2.3, 6, 25 and 50 nm resulting in a better control of $npFe^0$ size and concentration. The changes in optical properties of such treated samples resembled the space weathering effects observed in lunar soils and it was possible to evaluate the influence of $npFe^0$ particle size on spectral red slope.

In this work we present a new method of controlled $npFe^0$ production on surface of olivine grains. We also evaluate the influence of $npFe^0$ concentration and particle-size on olivine spectral darkening and reddening, as well as intensity reduction, shape, and position of the olivine 1 µm absorption band.

Materials and methods

Samples

Natural olivine from Åheim, Norway was used in this study. A pale green, polycrystalline olivine sample was thin-sectioned, and analyzed using a CAMECA SX-100 electron microprobe (Table 1). Another part of the sample was crushed and inclusion-free fragments were hand-picked using an optical microscope. Subsequently, the olivine grains were pulverized in an agate mortar and sieved to obtain fine (10-80 μm) powder. Part of the powder was preserved for reference measurements while the rest was thermally treated in a two-step heating method to achieve the formation of $npFe^0$ on the surface of olivine grains.

$npFe^0$ production and characterization

A two-step thermal treatment method was developed to produce $npFe^0$ on the surface of olivine grains. Furthermore, $npFe^0$ abundance and particle size control was achieved through variations in temperature and duration of the treatment steps.

In the first step, the olivine powder was heated in air (under oxidizing condition) using a Linn LM 112.07 muffle furnace. Various temperatures and heating durations were tested (Table 2) in order to induce partial oxidation of the iron ions that were liberated from the olivine structure, primarily those close to the surface of the olivine grains. The temperatures were selected to be low enough to preserve the olivine structure undamaged (e.g. Barcova et al., 2003; Michel et al., 2013).The oxidation of Fe^{2+} ions leads to a charge imbalance in the olivine structure causing diffusion of Fe^{3+} atoms to the surface where they precipitate in the form of Fe^{3+} oxide nanoparticles and create vacancies in the olivine crystal structure (Zboril et al., 2003; Barcova et al., 2003).

In the second step, the Fe^{3+} oxide nanoparticles were reduced into $npFe^0$ in a hydrogen atmosphere (using a steady hydrogen flow at 500°C for 1 hour with an Anton Paar XRK900 reactor). The reduction process was monitored in-situ using X-ray powder diffraction (XRD). The freshly produced $npFe^0$ particles were surface-passivated for 30 minutes in 30°C gas mixture flow of N_2 with 2% O_2 to minimize oxidation upon contact with ambient air.

The XRD was performed using a PANalytical X'Pert PRO MPD diffractometer (iron-filtered CoK_α radiation: λ = 0.178901 nm, 40 kV and 30 mA) in the Bragg-Brentano geometry and equipped with an X´Celerator detector, that has programmable divergence and diffracted beam anti-scatter slits. The samples were placed into a shallow cavity sample holder (made of Macor) and repeatedly-scanned in the 2θ range of 5–120° (resolution of 0.017° in 2θ) at specific temperatures. SRM640 (Si) and SRM660 (LaB6) commercial standards from NIST (National Institute of Standards and Technology) were used for evaluation of the line positions and instrumental line broadening, respectively. Identification of crystalline phases was performed using the High Score Plus (PANalytical) software in conjunction with the PDF-4+ database.

The size and concentration of $npFe^0$ was determined using a combination of transmission electron microscopy (TEM), frequency dependence of magnetic susceptibility, and magnetic hysteresis measurements, Composition of the $npFe^0$ was verified using scanning transmission electron microscopy equipped with energy-dispersive X-ray spectroscopy (STEM-EDX).

The TEM observations and STEM-EDX analysis was done using a Teknai F30 TEM/STEM with an EDAX Si/Li EDX spectrometer. The TEM observations of $npFe^0$ particles were done on sharp, thin edges of olivine powder grains placed on a copper grid holder.

The frequency dependence of magnetic susceptibility was tested using a ZH instruments SM-100/105 susceptibility meters at 16, 32, 64, 128 and 256 kHz frequency steps and 160 A/m RMS field intensity.

The magnetic hysteresis measurements were accomplished using a Princeton Measurements Micromag Model 3900 VSM (Vibrating Sample Magnetometer). All magnetizations were normalized by sample. First, a hysteresis loop of the olivine precursor was measured. This loop was subsequently used for background subtraction (to subtract paramagnetic/diamagnetic contribution of olivine and sample holder) of all thermally-treated olivine sample hysteresis loops. After background subtraction, any residual paramagnetic/diamagnetic slope was removed. Resulting hysteresis loops correspond to $npFe^0$ produced in our samples. The concentration of $npFe^0$ can be estimated by comparison of the sample saturation magnetization to that of a pure metallic iron (218 Am^2/kg, Dunlop and Özdemir, 2001, p. 51).

For room-temperature ^{57}Fe Mössbauer measurements, a Mössbauer spectrometer with a $^{57}Co(Rh)$ source of γ-rays was used. The values of the derived hyperfine Mössbauer parameters are attributed to metallic iron (α-Fe) at room temperature. Mössbauer spectra were fitted by means of the Lorentzian line shapes using the least squares method featured in the MossWinn analysis program. To obtain a qualitatively resolved Mössbauer spectrum for low $npFe^0$ concentration, a long measurement time was applied (22 days).

The spectral measurements of fresh and modified olivine samples were done in visible – near infrared (VIS-NIR) range of 350-2400 nm using an Analytical Spectral Devices FieldSpec Pro spectrometer calibrated with a Labsphere SRS-99-020 Spectralon white standard. The reflectance is determined at 550 nm. The spectral slope is calculated as the difference in normalized reflectance at 1689 nm and 630 nm divided by 1059 nm. The normalized reflectance was calculated as reflectance divided by

reflectance at 550 nm. The 1 μm absorption band depth is calculated as the normalized average reflectance at 630 and 1689 nm minus the band minimum. The 1 μm absorption band minimum position was manually read from the data files. To further study shift of the band minimum in our samples the modified Gaussian model (MGM, Sunshine et al., 1999, MATLAB code available on RELAB web page http://www.planetary.brown.edu/mgm/index.html) was applied to the spectral data.

Results

The combination of the two successive thermal treatment steps resulted in a formation of $npFe^0$ (α-Fe, bcc structure) on the olivine grains with a well-controlled particle size and distribution over the surface. The characteristics of such $npFe^0$ particles is comparable to the $npFe^0$ observed in space weathered extraterrestrial materials. Table 3 summarizes spectral properties of the thermally-treated olivine samples and $npFe^0$ concentration estimate derived from magnetic hysteresis measurements. There is a quasi-exponential trend in the $npFe^0$ concentration with increasing temperature of the first heating step (Fig. 1). Longer duration of the first heating step also increases the $npFe^0$ concentration. Due to the quasi-exponential trend between $npFe^0$ concentration and first step heating temperature, the samples heated to temperatures in excess of 750°C become very rich in $npFe^0$ and their reflectance spectra become very low. Thus, in order to reduce the amount of $npFe^0$ in the 850°C sample to the level of other samples, the duration of the first heating step was reduced to 30 seconds. The size of the $npFe^0$ particles in all samples as seen by TEM (Fig. 2) is in ~5-20 nm range with the majority (~90%) being in the 7-15 nm range. An exception is the sample heated to 850°C (850s30) where an additional population of larger ~40-50 nm $npFe^0$ particles can be observed (Fig. 3). The larger particles most likely formed by sintering of smaller particles into clusters.

The above mentioned $npFe^0$ particle range is supported by a frequency dependence of the magnetic susceptibility data which occurs in particles that are in a superparamagnetic (SP) state that requires iron particles smaller than ~8 nm (Kneller and Luborsky, 1963; Dunlop and Özdemir, 2001, p. 131). No detectable systematic frequency dependence was observed in any sample, indicating that majority of the $npFe^0$ particles were larger than the ~8 nm threshold.

One single $npFe^0$ particle was investigated by high-resolution TEM in order to determine the lattice spacing on the single nanoparticle. Lattice fringes of 0.19 ±0.05 nm were observed (Fig. 4) which is consistent with the spacing of (110) of α-Fe d_{110} = 0.203 nm (Noguchi et al., 2011). The surface passivation of $npFe^0$ on the olivine limited the formation of iron oxides to a thin shell on the metallic nanoparticle core (cf. Filip et al., 2007 and Siskova et al., 2012). This is well documented on STEM-EDX data as little oxygen (mostly originating from olivine background) is detected in individual $npFe^0$ particles (Fig. 5).

Additionally, the modified olivine samples were studied by means of zero-field ^{57}Fe Mössbauer spectroscopy at room temperature. Only paramagnetic doublet (isomer shift δ = 1.12 mm/s and quadrupole split ε_Q = 2.96 mm/s) and the singlet (δ = 0.53 mm/s), both originating from Fe^{2+} in the two olivine octahedral sites with different point symmetries, are visible in the spectra. The ferromagnetic sextet component corresponding to ferromagnetic metallic iron is not observed due to $npFe^0$ amount being below Mössbauer spectroscopy resolution.

The reflectance spectra of fresh and modified olivine samples were measured in 350-2400 nm (VIS-NIR) range. A progressive trend in the reflectance reduction (darkening), in 1 μm absorption band depth reduction, slope change (reddening), shift in 1 μm band center position, and 1 μm band width at half depth is observed with the increasing $npFe^0$ concentration (Fig. 6).

Discussion

The size range of the npFe^0 (~5-20 nm) produced in olivine powders by our method is slightly larger than that found in vapor deposition rims (~3 nm), but considerably smaller than the nanophase iron found in agglutinates (e.g. Pieters et al., 2000; Hapke, 2001, Keller and Clemett, 2001). The presence of the npFe^0 is also seen in the strong alteration of the VIS-NIR spectra. Compared to spectra of the fresh olivine, samples with artificially produced npFe^0 show spectral changes similar to these seen in naturally space-weathered lunar soils and asteroid surfaces (e.g. Hapke, 2001; Chapman, 2004). This gives us a confidence that despite slight differences between our samples and natural space weathering products (npFe^0 particles on mineral grain surfaces vs. within coating rims, possible presence of a thin oxide shell on our npFe^0 particles) our laboratory simulations are good proxy for natural space weathering and closely resemble optical effects of the fine nanophase iron fraction including slope change (Noble et al., 2007). The changes in olivine spectral parameters are quantified in Table 3. Because the npFe^0 particle size is kept constant (with exception of 850s30 sample), the spectral changes can be studied as a function of increasing npFe^0 concentration. The results indicate that there is a linear trend between amount of npFe^0 and the 1 μm band center position (Fig. 7) and a logarithmic trend between the amount of npFe^0 and the reflectance (Fig. 8), 1 μm absorption band depth (Fig. 8), spectral slope (Fig. 9) and the 1 μm band width at half depth (Fig. 10).

The linear trend between amount of npFe^0 and the 1 μm band center position is in contrast with results of previous studies (Hiroi and Sasaki, 2001; Sasaki et al., 2002; 2003; Brunetto et al,. 2005) where no significant changes of the band position were observed during simulated space weathering. However, compared to these studies, our samples cover a broader range of npFe^0 amount and related

spectral changes. It is apparent that for samples with less $npFe^0$ (below 0.01 wt% and spectral changes of a similar magnitude as in above-mentioned studies) there is no significant change in band position. However, with higher $npFe^0$ the amount of the shift in 1 µm band center became more apparent. The mechanism behind the band shift may be Fe^{2+} disassociation from olivine structure into $npFe^0$ particles. This is also supported by the linear correlation between 1 µm band center and amount of $npFe^0$. The possible occurrence of this process in extremely weathered natural planetary surfaces is uncertain and requires further studies. In general, asteroidal regoliths do not get as mature as lunar regolith and olivine is minor constituent of the lunar regolith.

The band center shift was further studied using the MGM model. As the olivine 1 µm absorption band is a superposition of three individual bands related to the different positions of Fe^{2+} ions in the olivine crystal structure (Burns, 1970), three Gaussian bands were used in the MGM model. The results are summarized in table 4 and figure 10. MGM method gives reliable results for samples with small to moderate $npFe^0$ amounts up to sample 650h1 with 0.023 wt% Fe. (With higher $npFe^0$ content the lower 1 µm band intensity to noise ratio and significant red slope causes unreliable Gaussian modeling of olivine samples.) The MGM results indicate that the shift in 1 µm band is primarily driven by changes in the third Gaussian band centered around 1200 nm (Fig. 11) which is caused (together with the ~840 nm band) by the Fe^{2+} in *M* (2) position (e.g. Burns, 1970). The MGM model figures are available in on-line supplementary material (Figs. S1-S7).

The observed logarithmic trend between slope change and amount of $npFe^0$ provides further insight into natural space weathering. A logarithmic trend between spectral slope change and the space weathering duration has been observed by Nesvorný et al. (2005) and Vernazza et al. (2009) for S-type asteroid families. In combination with our observation of a logarithmic trend between amount of

$npFe^0$ and reflectance, 1 µm absorption band depth, and spectral slope, we have demonstrated four additional characteristics of space weathering: A similar logarithmic trend is valid between space weathering duration and (1) darkening, (2) reduction of 1 µm olivine absorption band, and (3) 1 µm band width at half depth. However, (4) the amount of $npFe^0$ increases linearly with the duration of the space weathering.

The 850s30 sample contains additional population of ~40-50 nm $npFe^0$ particles which accounts for its VIS-NIR spectral properties. The spectrum of this sample follows the trends observed for other samples. However, sample 850s30 does not fully follow the increasing red slope trend (Fig. 9). This is most likely due to the fact that part of its $npFe^0$ is in a form of larger particles, which does not contribute to the red slope. This sample is analogous to lunar soils containing both small $npFe^0$ fraction in vapor deposition rims as well as larger $npFe^0$ particles in agglutinates. The relatively reduced magnitude of the slope change in this sample is in agreement with Noble et al. (2007) who observed insignificant slope change for $npFe^0$ particles larger than ~50 nm.

Conclusions

The two-step thermal treatment method allows for controlled growth of iron nanoparticles on the surfaces of olivine powder grains. This enables quantitative investigations of the role of $npFe^0$ in space weathering and related changes in reflectance spectra. Compared to fresh olivine, our olivine samples with artificially introduced ~5-20 nm sized $npFe^0$ particles exhibit the spectral characteristics of lunar-type space weathering. From a quantitative point of view, a linear trend is observed between the amount of $npFe^0$ and 1 µm band center position. This trend is more pronounced for samples with

$npFe^0$ amounts in excess of 0.015 wt%. The mechanism behind the band shift may be Fe^{2+} disassociation from olivine structure into $npFe^0$ particles.

A logarithmic trend is observed between amount of $npFe^0$ and darkening, reduction of 1 µm olivine absorption band, reddening, and 1 µm band width at half depth. Observations of asteroid families show a logarithmic weathering trend between slope change and duration. Our results reveal four additional characteristics of space weathering: The logarithmic trend with space weathering duration is valid for (1) darkening, (2) reduction of 1 µm olivine absorption band, and (3) 1 µm band width at half depth, while (4) the amount of $npFe^0$ increases linearly with duration.

The olivine sample with an additional population of larger $npFe^0$ particles follows similar spectral trends as other samples, except for the reddening trend. This is interpreted as the larger, (~40-50 nm sized), $npFe^0$ particles do not contribute to the slope change as efficiently as the smaller $npFe^0$ fraction.

Acknowledgements

The work was supported by Ministry of Education, Youth and Sports Czech Republic (grant no. LH12079, LK21303, MSM0021620855), Academy of Finland (grant no. 257487), Czech Science Foundation (grant no. GACR P108/11/1350) and Palacký University, Olomouc, Czech Republic (grant no. PrF_2013_014). We also thank for the support by the Operational Program Research and Development for Innovations – European Regional Development Fund (CZ.1.05/2.1.00/03.0058) and Operational Program Education for Competitiveness – European Social Fund (CZ.1.07/2.3.00/20.0017, CZ.1.07/2.3.00/20.0170, CZ.1.07/2.3.00/20.0155, and CZ.1.07/2.3.00/20.0056) of the Ministry of Education, Youth and Sports of the Czech Republic. This work (publication SSERVI-2014-080) was

directly supported by NASA's Solar System Exploration Research Virtual Institute cooperative agreement notice NNA14AB05A.

References

Adams, J.B., Jones, R.L., 1970. Spectral reflectivity of lunar samples. Science 167, 737-739.

Adams, J.B., McCord, T.B., 1971. Alteration of lunar optical properties: age and composition effects. Science 171, 567-571.

Adams, J.B., McCord, T.B., 1973. Vitrification darkening in the lunar highlands and identification of Descartes material at the Apollo 16 sites. Proceedings of the Lunar and Planetary Science Conference 4, 163-177.

Allen, C.C., Lauer, H.V., Jr., Morris, R.V., and McKay, D.S., 1993, Microscopic iron metal on glass and minerals – —a tool for studying regolith maturity. Icarus 104, 291-300.

Allen, C.C., Morris, R.V., McKay, D.S., 1996. An experimental analog to maturing lunar soil. Proceedings of the Lunar and Planetary Science Conference 37, 13-14.

Barcova, K., Mashlan, M., Zboril, R., Martinec, P., 2003. Mossbauer study of transformation mechanism of Fe cations in olivine after thermal treatments in air. Journal of Radioanalytical and Nuclear Chemistry 255, 529-533. doi: 10.1023/A:1022588500878

Binzel, R.P., Morbidelli, A., Merouane, S., DeMeo, F.E., Birlan, M., Vernazza, P., Thomas, C.A., Rivkin, A.S., Bus, S.J., Tokunaga, A.T., 2010. Earth encounters as the origin of fresh surfaces on near-Earth asteroids. Nature 463, 331-334. doi:10.1038/nature08709.

Brunetto, R., Romano, F., Blanco, A., Fonti, S., Martino, M., Orofino, V., Verrienti, C., 2005. Space weathering of silicates simulated by nanosecond pulse UV excimer laser. Icarus 180, 546-554. doi:10.1016/j.icarus.2005.10.016.

Burns, R.G., 1970. Crystal field spectra and evidence of cation ordering in olivine minerals. American Mineralogist 55, 1608-1632.

Chapman, C.R., 2004. Space weathering of asteroid surfaces. Annual Reviews 32, 539-567. doi:10.1016/j.icarus.2010.05.006.

Clark, B.E., Lucey, P., Helfenstein, P, Bell Iii, J.F., Peterson, C., Veverka, J., Mcconnochie, T., Robinson, M.S., Bussey, B., Murchie, S.L., Izenberg, N.I., Chapman, C.R., 2001. Space weathering on Eros: Constraints from albedo and spectral measurements of Psyche crater. Meteoritics and Planetary Science 36, 1617-1637. doi: 10.1111/j.1945-5100.2001.tb01853.x.

Dunlop, D.J., Özdemir, Ö., 2001. Rock Magnetism: fundamentals and frontiers, Cambridge University Press, Cambridge, 573 pages.

Filip, J., Zbořil, R., Schneeweiss, O., Zeman, J., Černík, M., Kvapil, P., Otyepka, M., 2007. Environmental applications of chemically-pure natural ferrihydrite. Environmental Science & Technology 41, 4367-4374.

Gaffey, M.J., 2010 Space weathering and the interpretation of asteroid reflectance spectra. Icarus 209, 564-574.

Hapke, B., 2001. Space weathering from Mercury to the asteroid belt. Journal of Geophysical Research 106, 10039-10073.

Hapke, B., Cassidy, W., Wells, E., 1975. Effects of vapour-phase deposition processes on the optical chemical and magnetic properties of the lunar regolith, Moon 13, 339-354.

Hiroi, T., Abe, M., Kitazato, K., Abe, S., Clark, B.E., Sasaki, S., Ishiguro, M., Barnouin-Jha, O.S., 2006. Developing space weathering on the Asteroid 25143 Itokawa. Nature 443, 56–58. doi:10.1038/nature05073.

Hiroi, T., Sasaki, S., 2001. Importance of space weathering simulation products in compositional modeling of asteroids: 349 Dembowska and 446 Aeternitas as examples. Meteoritics and Planetary Science 36, 1587-1596.

Keller, L.P., Clemett, S.J., 2001. Formation of nanophase iron in the lunar regolith. Lunar and Planetary Science Conference XXXII, abstract no. 2097.

Keller, L., McKay, D., 1997. The nature and origin of rims on lunar soil grains. Geochimica et Cosmochimica Acta 61, 2331-2340.

Keller, L., McKay, D., 1993. Discovery of vapor deposits in the lunar regolith. Science, 261, 1305-1307. doi: 10.2307/2882155

Kneller, E.F., Luborsky, F.E., 1963. Particle size dependence of coercivity and remanence of single-domain particles. Journal of Applied Physics 34, 656-658.

Lazzarin, M., Marchi, S., Moroz, L.V., Brunetto, R., Magrin, S., Paolicchi, P., Strazzulla, G., 2006. Space Weathering in the Main Asteroid Belt: The Big Picture. The Astrophysical Journal Letters 647, L179–L182, doi: 10.1086/507448.

Liu, Y., Taylor, L.A., Thompson, J.R., Schnare, D.W., Park, J.S., 2007. Unique properties of lunar impact glass: Nanophase metallic Fe synthesis. American Mineralogist 92, 1420-1427.

Lucey, P.G., Noble, S.K., 2008. Experimental test of a radiative transfer model of the optical effects of space weathering. Icarus 197, 348-353. doi: 10.1016/j.icarus.2008.05.008

Markley, M.M., Fuller, M.D., Kletetschka, G., 2013. Magnetic scanning of iron blebs in laser irradiated olivine grains. Meteoritics & Planetary Science 48, A233.

Marchi, S., Brunetto, R., Magrin, S., Lazzarin, M., Gandolfi, D., 2005. Space weathering of near-Earth and main belt silicate-rich asteroids: observations and ion irradiation experiments. Astronomy & Astrophysics 443, 769-775. doi: 10.1051/0004-6361:20053525

McCord, T.B., Johnson, T.V., 1970. Lunar spectral reflectivity (0.30 to 2.50 microns) and implications for remote mineralogical analysis. Science 169, 855-858.

McCord, T.B., Adams, J.B., 1973. Progress in remote optical analysis of lunar surface composition. Moon 7, 453-474.

Michel, R., Ammar, M.R., Poirier, J., Simon, P., 2013. Phase transformation characterization of olivine subjected to high temperature in air. Ceramics International 39, 5287-5294.

Nesvorný, D., Jedlicke, R., Whiteley, R.J., Ivezić, Ž., 2005. Evidence for asteroid space weathering from the Sloan Digital Sky Survey. Icarus 173, 132-152.doi: 10.1016/j.icarus.2004.07.026

Noble, S.K., Pieters, C.M., Keller, L.P., 2007. An experimental approach to understanding the optical effects of space weathering. Icarus 192, 629-642. doi:10.1016/j.icarus.2007.07.021.

Noguchi T., Nakamura T., Kimura M., et al., 2011. Incipient Space Weathering Observed on the Surface of Itokawa Dust Particles. Science 333. 1121-1125. doi: 10.1126/science.1207794.

Pieters, C.M., Taylor, L.A., Noble, S.K., Keller, L.P., Hapke, B., Morris, R.V., Allen, C.C., McKay, D.S., Wentworth, S., 2000. Space weathering on airless bodies: Resolving a mystery with lunar samples. Meteoritics and Planetary Science 35, 1101-1107.

Pieters, C.M., Fischer, E.M., Rode, O., Basu, A., 1993. Optical effects of space weathering: The role of the finest fraction. Journal of Geophysical Research: Planets 98, 20817-20824. doi: 10.1029/93JE02467

Sasaki, S., Kurahashi, E., Yamanaka, C., Nakamura, K., 2003. Laboratory simulation of space weathering: Changes of optical properties and TEM/ESR confirmation of nanophase metallic iron. Advances in Space Research 31, 2537-2542. doi: 10.1016/S0273-1177(03)00575-1

Sasaki, S, Hiroi, T., Nakamura, K., Hamabe, Y., Kurahashi, F., Yamada, M., 2002. Simulation of space weathering by nanosecond pulse laser heating: dependence on mineral composition, weathering trend of asteroids and discovery of nanophase iron particles. Advances in Space Research 29, 783-788.

Sasaki, S., Nakamura, K., Hamabe, Y., Kurahashi, E., Hiroi, T., 2001. Production of iron nanoparticles by laser irradiation in a simulation of lunar-like space weathering. Nature 410, 555-557. doi: 10.1038/35069013

Siskova, K., Tucek, J., Machala, L., Otyepkova, E., Filip, J., Safarova, K., Pechousek, J., Zboril, R., 2012. Air-stable nZVI formation mediated by glutamic acid: solid-state storable material exhibiting 2D chain morphology and high reactivity in aqueous environment. Journal of Nanoparticle Research 14, 805 (13 pages). doi: 10.1007/s11051-012-0805-9

Sunshine, J.M., Pieters, C.M., Pratt, S.F., McNaron-Brown, K.S., 1999. Absorption Band Modeling in Reflectance Spectra: Availability of the Modified Gaussian Model. Lunar and Planetary Science Conference XXX, abstract no. 1306.

Tang, H., Wang, S., Li, X., 2012: Simulation of nanophase iron production in lunar space weathering. Planetary and Space Science 60, 322-327. doi: 10.1016/j.pss.2011.10.006

Taylor, L.A., Pieters, C.M., Morris, R.V., Keller, L.P., McKay, D.S., 2001. Lunar mare soils: Space weathering and the major effects of surface-correlated nanophase Fe. Journal of Geophysical Research: Planets 106, 27985-28000. doi: 10.1029/2000JE001402

Vernazza, P., Binzel, R.P., Rossi, A., Fulchignoni, M., Birlan, M., 2009. Solar wind as the origin of rapid reddening of asteroid surfaces. Nature 458, 993-995. doi:10.1038/nature07956

Zboril, R., Mashlan, M., Barcova, K., Walla, J., Ferrow, E., Martinec, P., 2003. Thermal behaviour of pyrope at 1000 and 1100°C: mechanism of Fe^{2+} oxidation and decomposition model. Physics and Chemistry of Minerals 30, 620-627.

Table 1. Chemical analyses of olivine used in this study.

	1	2	3	4	5	6	7	8	9	10	11	12	13	14	15	16	17	18	19	20	mean	s.d.
analyses in wt.%																						
SiO_2	40.88	41.25	41.75	41.33	41.23	41.26	41.38	41.44	41.19	41.18	41.09	41.77	41.52	41.33	41.64	41.47	41.58	41.41	41.94	41.95	41.43	0.28
Al_2O_3	0.04	b.d.l.	b.d.l.	b.d.l.	b.d.l.	b.d.l.	0.04	b.d.l.	b.d.l.	b.d.l.	b.d.l.	b.d.l.	b.d.l.	b.d.l.	b.d.l.	b.d.l.	b.d.l.	b.d.l.	b.d.l.	b.d.l.	0.04	0.00
FeO^T	6.69	6.67	6.58	6.72	6.67	6.80	6.63	6.69	6.72	6.74	6.67	6.64	6.71	6.75	6.63	6.68	6.67	6.61	6.63	6.68	6.68	0.05
NiO	0.39	0.37	0.41	0.39	0.36	0.38	0.38	0.38	0.38	0.39	0.37	0.40	0.39	0.37	0.38	0.39	0.38	0.39	0.38	0.38	0.38	0.01
MnO	0.13	0.11	b.d.l.	b.d.l.	0.11	0.12	b.d.l.	b.d.l.	0.12	b.d.l.	0.15	0.12	b.d.l.	b.d.l.	0.10	0.13	b.d.l.	b.d.l.	b.d.l.	b.d.l.	0.12	0.01
MgO	51.68	51.25	51.78	51.56	51.83	51.90	51.95	51.35	51.60	51.67	51.61	51.78	51.67	51.40	51.23	51.34	51.68	51.30	51.24	51.07	51.54	0.25
Total	99.80	99.64	100.52	100.00	100.21	100.44	100.38	99.85	100.00	99.97	99.90	100.71	100.28	99.86	99.97	100.01	100.30	99.71	100.20	100.07	100.09	0.28
coeficients of empirical formulae in a.p.f.u. calculated on the basis of 4 oxygens in formula unit																						
Si	0.992	1.001	1.003	0.999	0.995	0.994	0.996	1.003	0.997	0.996	0.995	1.002	1.001	1.000	1.006	1.002	1.001	1.003	1.010	1.011	1.000	0.005
Al	0.001						0.001														0.001	
Fe	0.136	0.135	0.132	0.136	0.135	0.137	0.133	0.135	0.136	0.136	0.135	0.133	0.135	0.137	0.134	0.135	0.134	0.134	0.134	0.135	0.135	0.001
Ni	0.008	0.007	0.008	0.008	0.007	0.007	0.007	0.007	0.007	0.008	0.007	0.008	0.008	0.007	0.007	0.008	0.007	0.008	0.007	0.007	0.007	0.000
Mn	0.003	0.002			0.002	0.002			0.002		0.003	0.002			0.002	0.003					0.002	0.000
Mg	1.869	1.854	1.854	1.858	1.865	1.865	1.865	1.852	1.861	1.864	1.864	1.852	1.856	1.855	1.845	1.850	1.856	1.852	1.839	1.836	1.856	0.009
Total	3.008	2.999	2.997	3.001	3.005	3.006	3.003	2.997	3.003	3.004	3.005	2.998	2.999	3.000	2.994	2.998	2.999	2.997	2.990	2.989	3.000	0.005
Forsterite content in mol. %																						
Fo	93.2	93.2	93.3	93.2	93.3	93.2	93.3	93.2	93.2	93.2	93.2	93.3	93.2	93.1	93.2	93.2	93.2	93.3	93.2	93.2	93.2	0.1

Notes: b.d.l. indicates values below detection limit; Ti, Cr, Ca, Na, and K were found to be below detection limit in all analyses

Measurement details: microprobe CAMECA SX-100; accelerating voltage 15kV / sample current 10nA: Na*K*α (standard: jadeite; detection limit 550 ppm), Si*K*α (quartz; 480 ppm), Mg*K*α (diopside; 950 ppm), K*K*α (sanidine; 240 ppm), Ca*K*α (diopside; 260 ppm), Ti*K*α (rutile; 320 ppm), Al*K*α (jadeite; 330 ppm), Mn*K*α (rhodonite; 700 ppm), Cr*K*α (Cr_2O_3; 600 ppm); 20kV / 10nA: Fe*K*α (magnetite; 450 ppm), Ni*K*α (NiSi; 230 ppm); beam diameter 2 µm.

Table 2. Conditions of sample processing. T_1 and t_1 are the temperature and time of the first heating step (in air). T_2 and t_2 are the temperature and time of the second heating step (in hydrogen). N/A – not applicable.

Sample	T_1 (°C)	t_1 (s)	T_2 (°C)	t_2 (s)
Raw olivine	N/A	N/A	N/A	N/A
400h1	400	3600	500	3600
450h1	450	3600	500	3600
500h1	500	3600	500	3600
550h1	550	3600	500	3600
600h1	600	3600	500	3600
650h1	650	3600	500	3600
700h1	700	3600	500	3600
750h1	750	3600	500	3600
850s30	850	30	500	3600

Table 3. Overview of sample spectral parameters, saturation magnetization (J_s) and calculated $npFe^0$ concentration. Iron concentration is calculated as the sample saturation magnetization divided by the saturation magnetization of pure iron (218 Am^2/kg). * – not possible to reliably determine.

Sample	Slope (μm^{-1})	1µm depth	Albedo at 550 nm	1um band center (nm)	1µm band width at half depth (nm)	J_s (mAm^2/kg)	Fe (wt%)
Olivine	0.031	0.21	0.78	1053	466	0	0.0
400h1	0.15	0.18	0.61	1048	356	16.44	0.0075
450h1	0.17	0.18	0.60	1048	347	18.43	0.0085
500h1	0.25	0.20	0.42	1048	306	24.59	0.011
550h1	0.22	0.15	0.52	1046	265	27.78	0.013
600h1	0.36	0.16	0.34	1045	222	31.89	0.015
650h1	0.41	0.10	0.28	1041	165	49.71	0.023
700h1	0.57	0.026	0.16	1031	118	128.7	0.059
750h1	0.69	0.00	0.11	970	*	253.2	0.12
850s30	0.36	0.034	0.28	1034	139	106.3	0.049

Table 4. Modified Gaussian model parameters of the olivine absorption band. C1-3 are the three Gaussian centers. FWHM1-3 are the full widths at half maximum. S1-3 are the Gaussian strengths. RMSD is the root mean square deviation.

	C1 (nm)	C2 (nm)	C3 (nm)	FWHM1 (nm)	FWHM2 (nm)	FWHM3 (nm)	S1	S2	S3	RMSD
Raw olivine	826	1022	1229	124	221	465	-0.0863	-0.239	-0.276	2.27E-02
400h1	837	1026	1202	170	181	436	-0.093	-0.195	-0.265	4.73E-03
450h1	834	1025	1201	166	184	450	-0.0916	-0.192	-0.27	7.28E-03
500h1	847	1032	1194	214	169	442	-0.126	-0.188	-0.303	3.77E-03
550h1	835	1028	1195	175	180	454	-0.0821	-0.161	-0.237	5.88E-03
600h1	853	1039	1187	265	160	464	-0.104	-0.134	-0.277	2.86E-03
650h1	846	1040	1171	280	154	487	-0.0697	-0.101	-0.226	2.77E-03

Fig. 1. The relation between the temperature of first heating step (in air) and amount of iron produced in form of iron nanoparticles. The heating duration was 1 hour for all displayed samples.

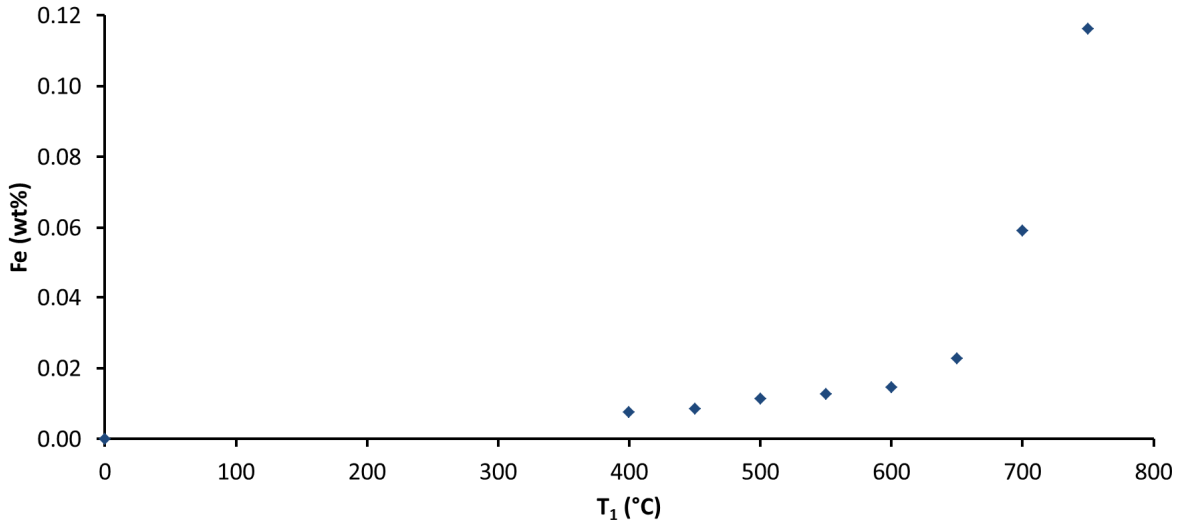

Fig. 2. TEM image of ~5-20 nm sized nanoparticles on olivine powder grains (sample 600h1).

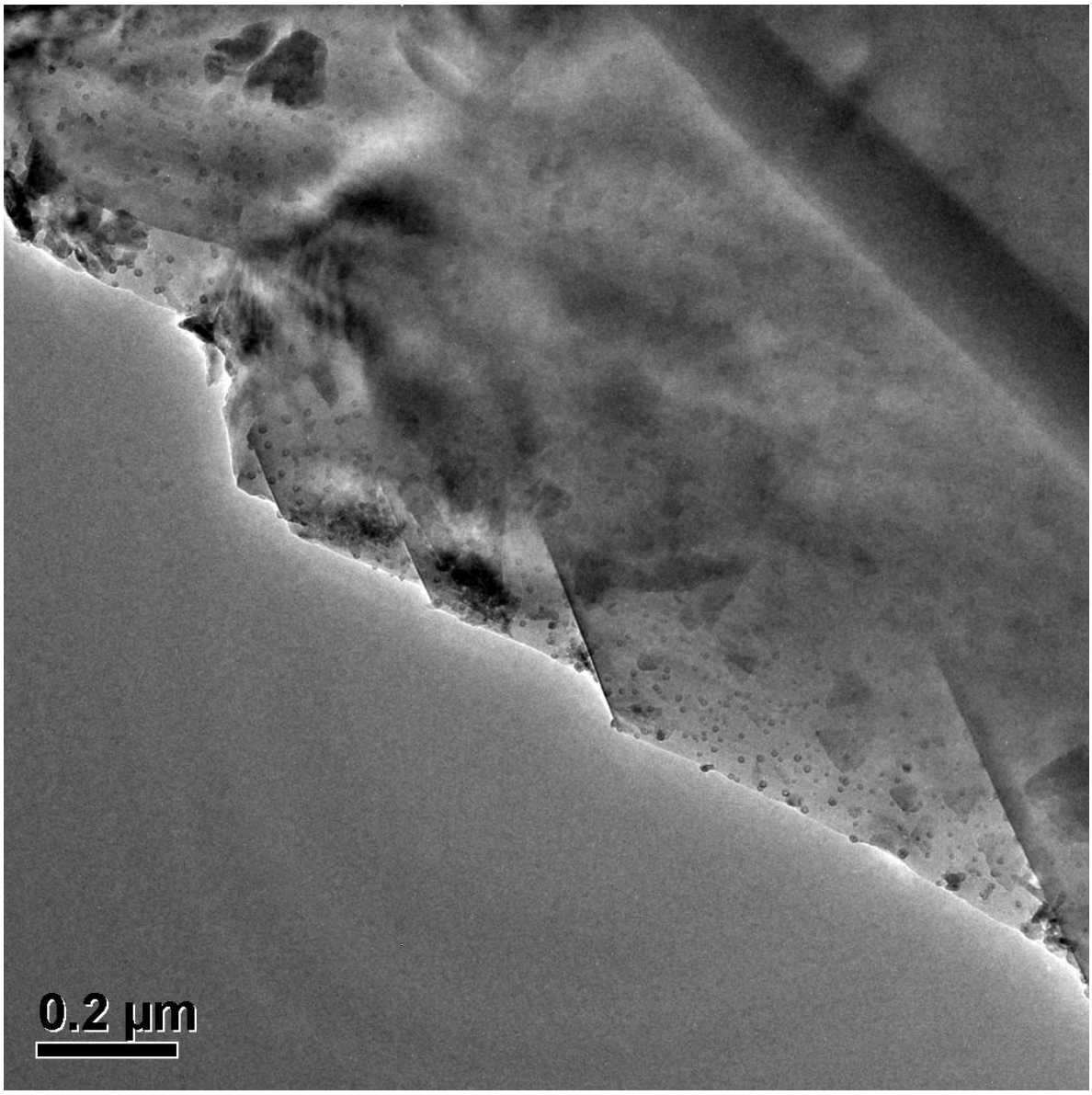

Fig. 3. TEM image of nanoparticles on olivine powder grains of the 850s30 sample. Two populations can be observed (~5-20 nm and ~40-50 nm).

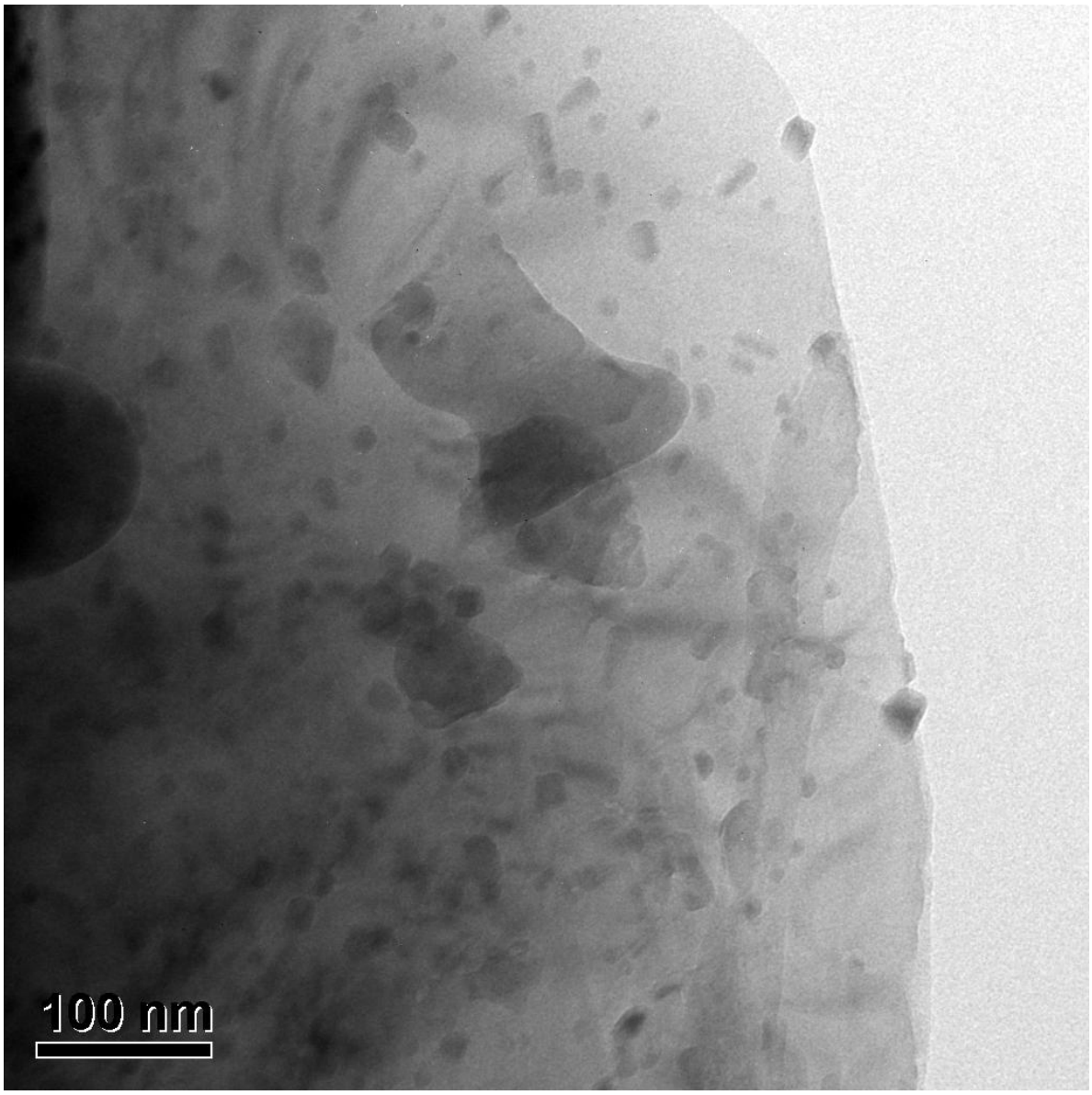

Fig. 4. High resolution TEM image of a single iron nanoparticle. The lattice fringes are highlighted by yellow circle. The lattice spacing is 0.19 ±0.05 nm.

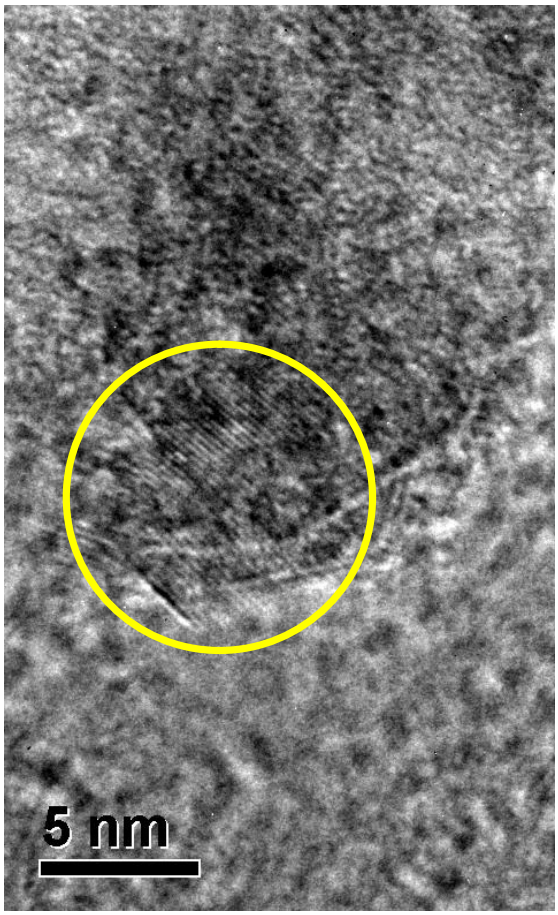

Fig. 5. STEM EDX spectra of an individual iron nanoparticle. These data show that iron nanoparticle oxidation was kept to minimum since only a minor peak of oxygen is observed and that is most likely caused by the olivine background (also indicated by a minor peak of silica and magnesium). Peak of copper is the signal of the sample holder.

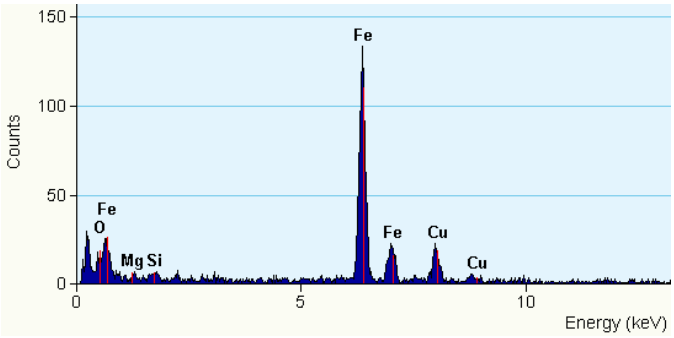

Fig. 6. VIS-NIR reflectance spectra (up – absolute values, down – normalized at 550 nm) of the fresh and modified olivine samples with increasing $npFe^0$ concentration (in wt%) as determined from the saturation magnetization. All samples show the continuous trend of 1 μm olivine absorption band reduction and increasing red slope with increasing amount of the $npFe^0$. The 850°C sample does not follow the increasing red slope trend because it contains additional larger $npFe^0$ particles that do not contribute to the red slope.

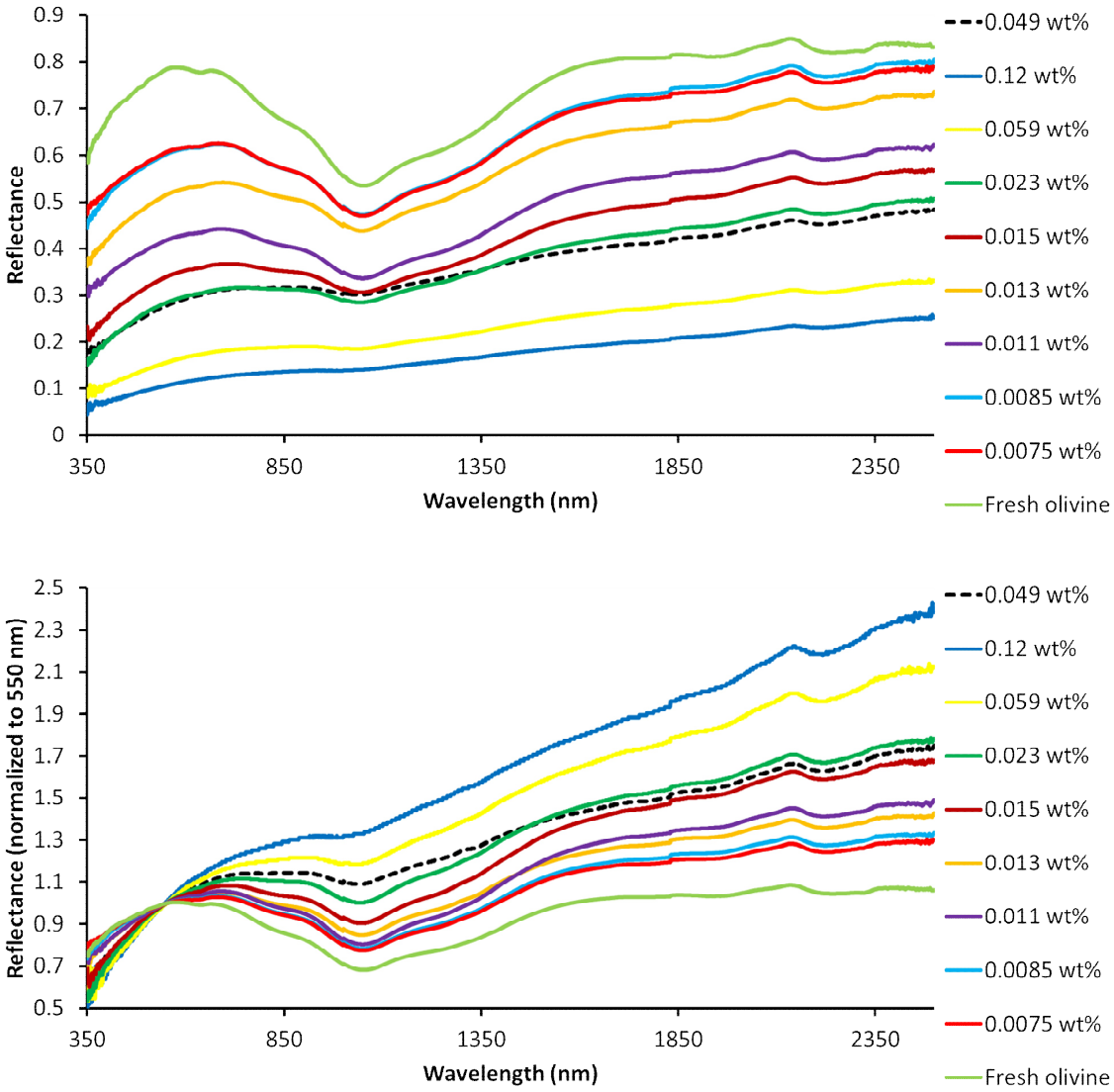

Fig. 7. The linear trend (black line) between the $npFe^0$ amount and the position 1 µm band center. R^2 is the root mean square deviation of the fit.

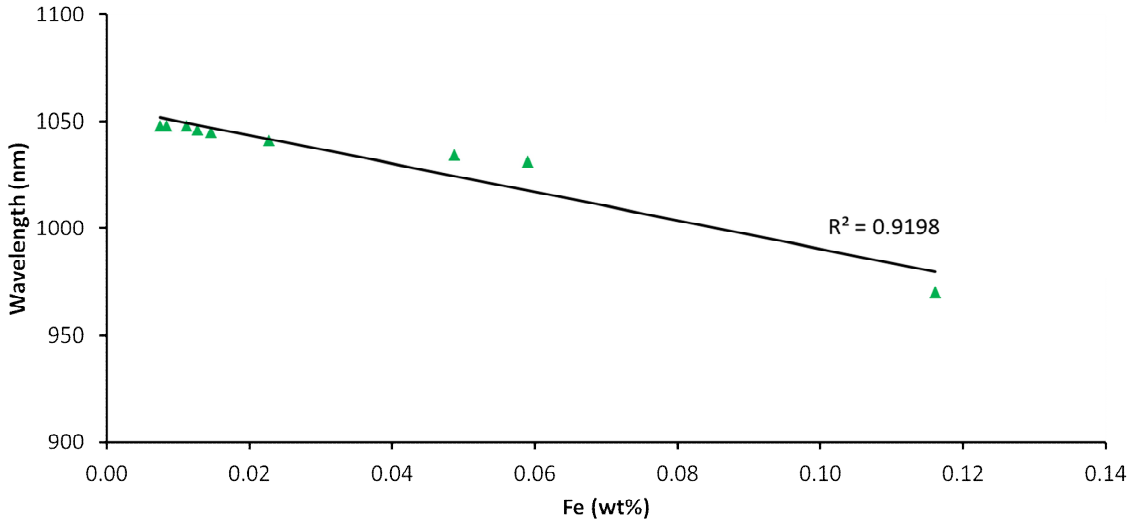

Fig. 8. The logarithmic trend (black lines) between the $npFe^0$ amount and the 1 µm band depth and the reflectance at 550 nm. R^2 is the root mean square deviation of the fit.

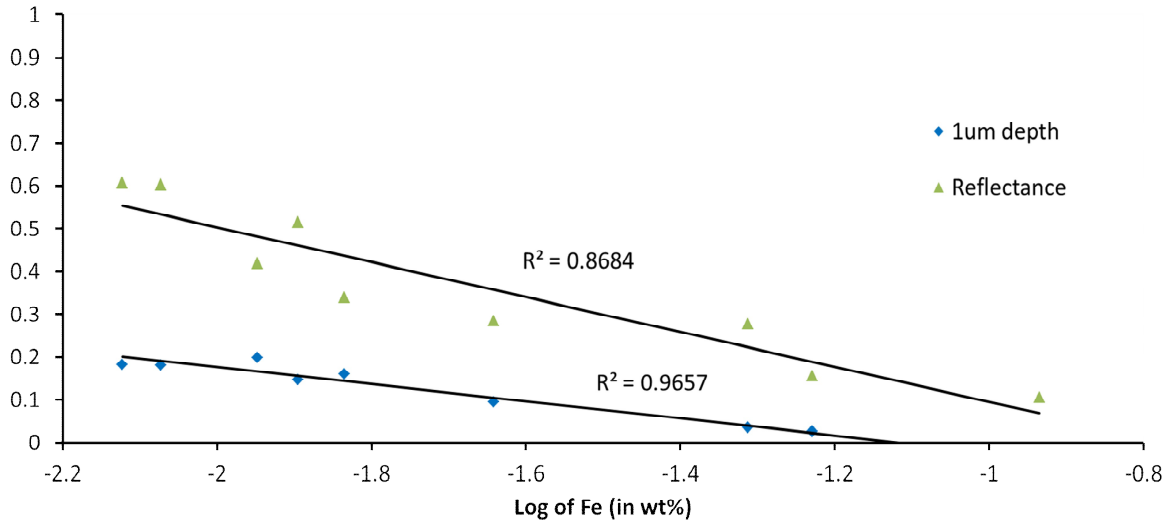

Fig. 9. The logarithmic trend (black line) between the $npFe^0$ amount and the spectral slope. The 850s30 sample (highlighted by a yellow circle) with additional population of larger $npFe^0$ particles does not fully follow the reddening trend. R^2 is the root mean square deviation of the fit.

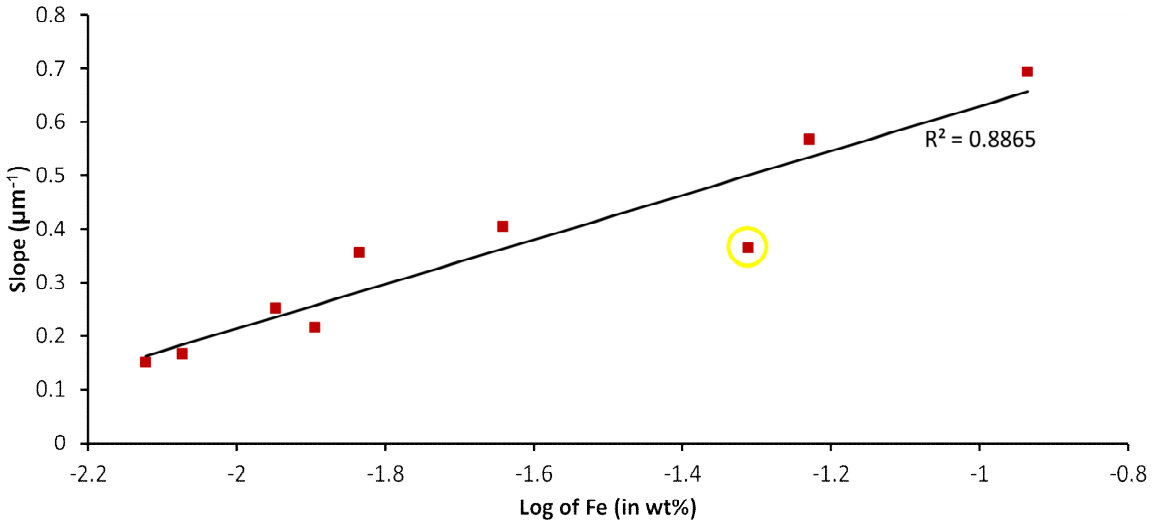

Fig. 10. The logarithmic trend (black line) between the npFe0 amount and the 1 µm band width at half depth. R2 is the root mean square deviation of the fit.

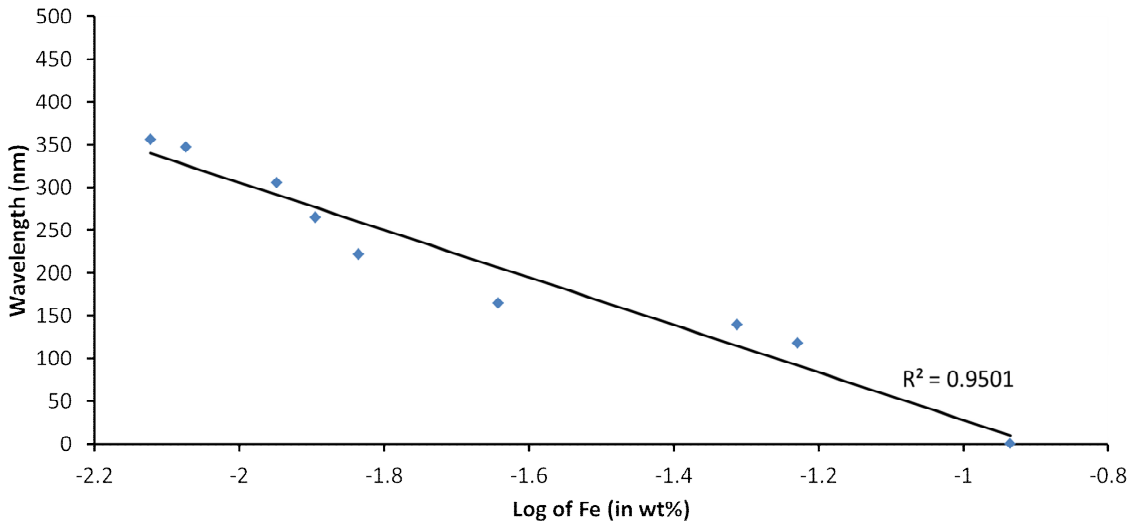

Fig. 11. Positions of the Gaussian band centres (C1-3) as a function of increasing $npFe^0$ content.

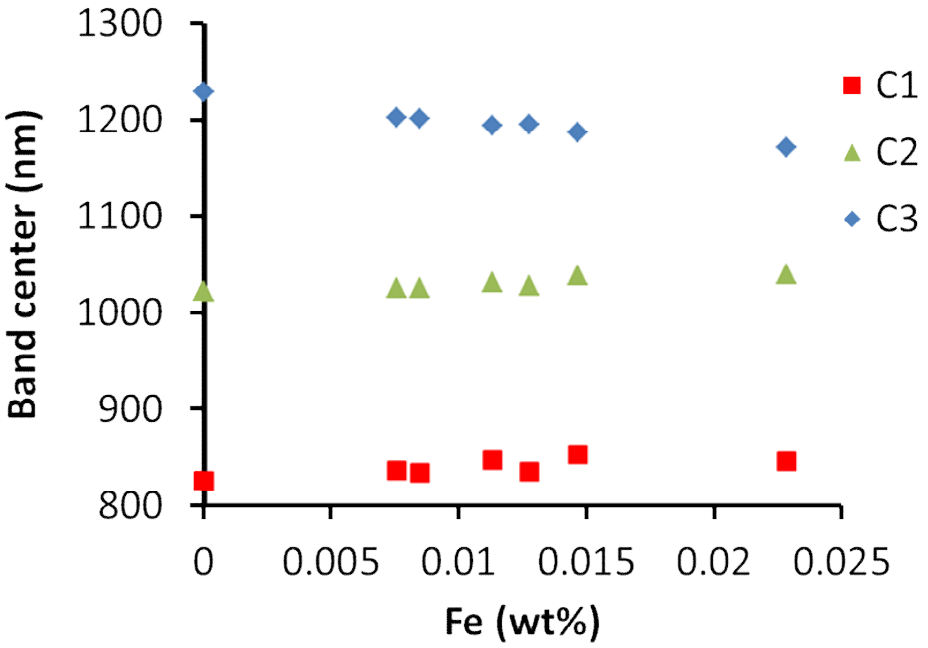

Supplementary material

Modified Gaussian model figures for samples listed in Table 4. Orange – measured spectrum, black – modeled spectrum, blue – gaussian bands, red – continuum, pink – residual error spectrum.

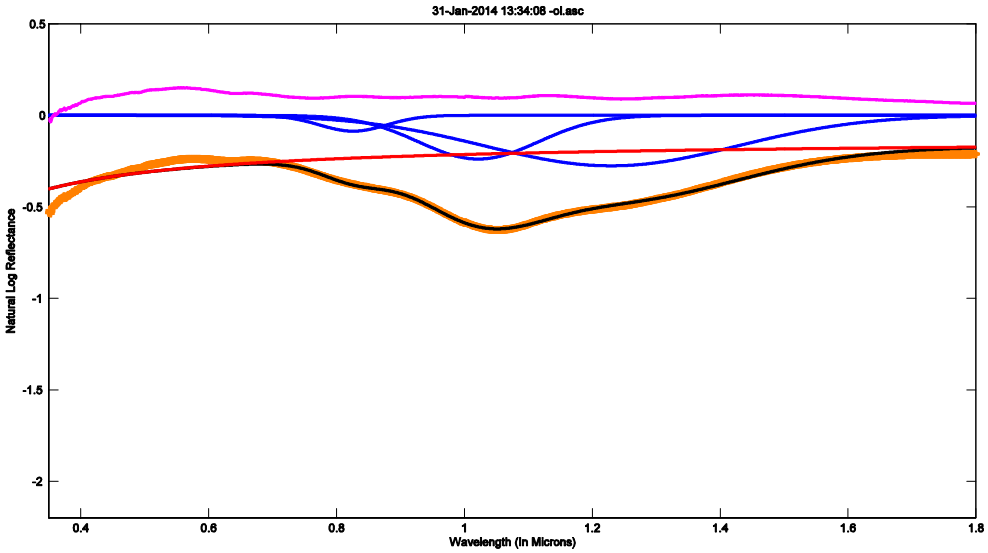

Fig. S1. Fresh olivine.

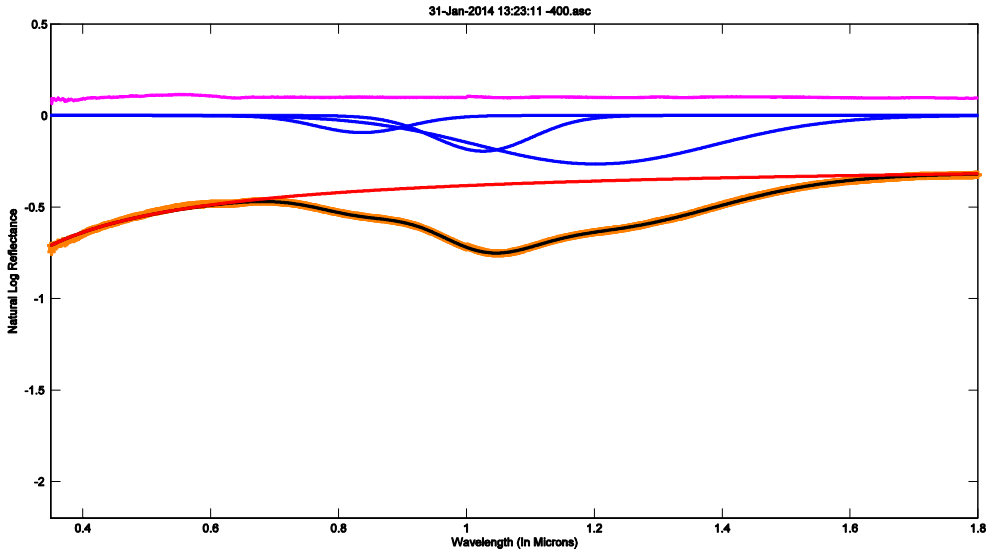

Fig. S2. Sample 400h1.

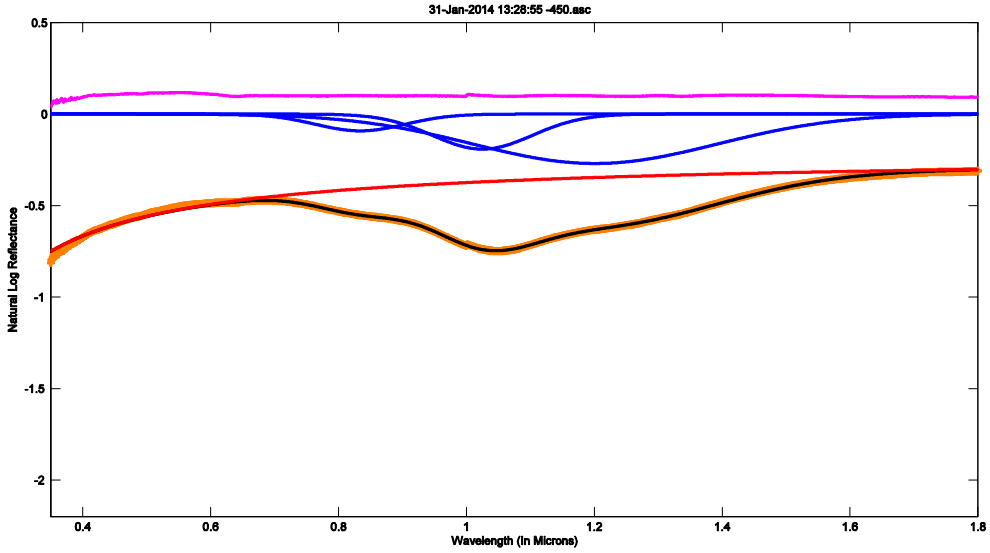

Fig. S3. Sample 450h1.

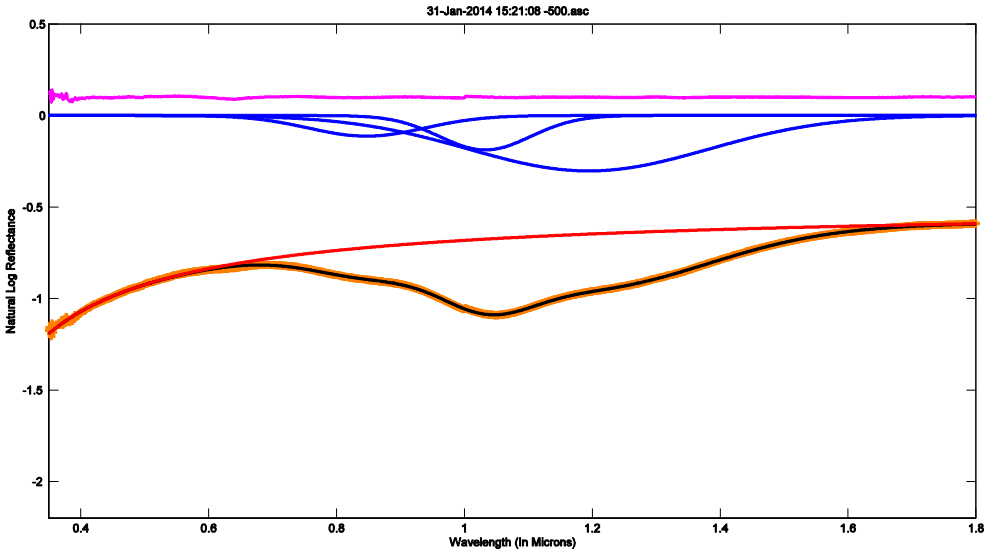

Fig. S4. Sample 500h1.

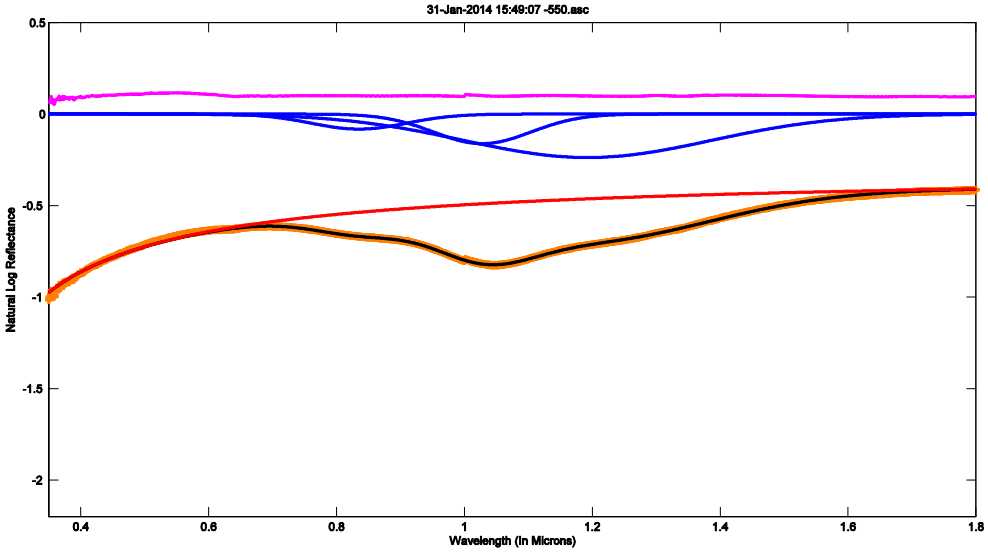

Fig. S5. Sample 550h1.

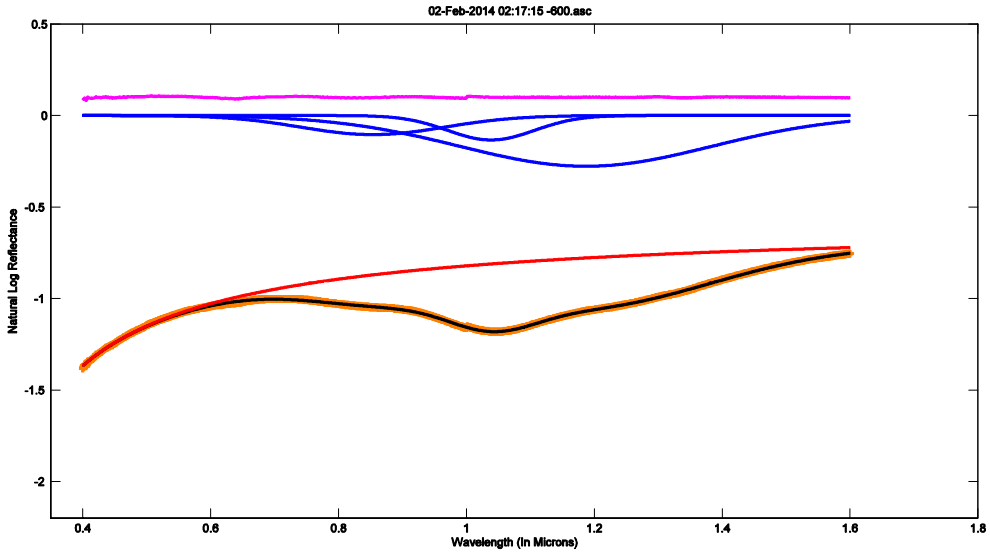

Fig. S6. Sample 600h1.

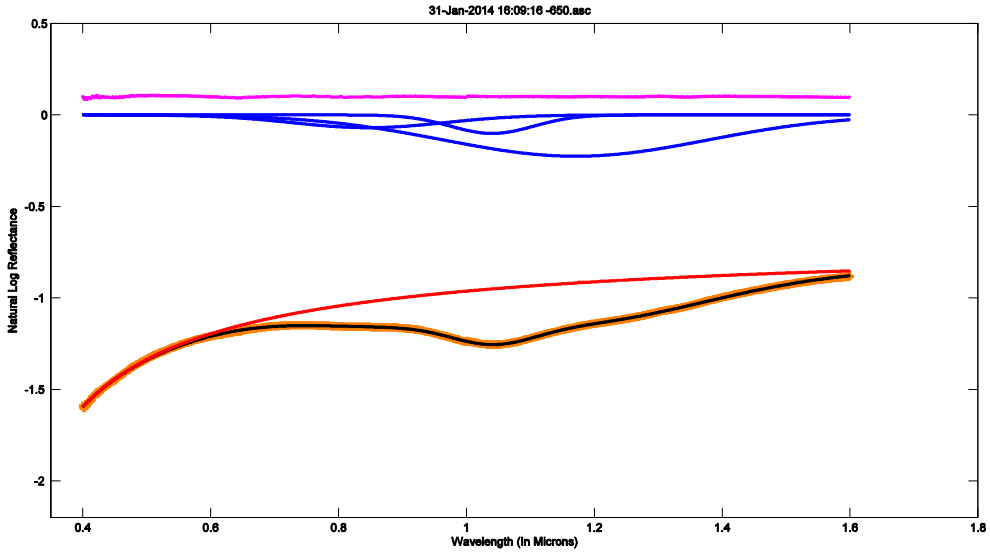

Fig. S7. Sample 650h1.